

# Cryogenic infrared spectroscopy as a probe of structure and dynamics of biomolecules

THÈSE N° 9164 (2018)

PRÉSENTÉE LE 7 DÉCEMBRE 2018

À LA FACULTÉ DES SCIENCES DE BASE

LABORATOIRE DE CHIMIE PHYSIQUE MOLÉCULAIRE

PROGRAMME DOCTORAL EN CHIMIE ET GÉNIE CHIMIQUE

ÉCOLE POLYTECHNIQUE FÉDÉRALE DE LAUSANNE

POUR L'OBTENTION DU GRADE DE DOCTEUR ÈS SCIENCES

PAR

Valeriu SCUTELNIC

acceptée sur proposition du jury:

Dr A.-S. Chauvin, présidente du jury

Prof. T. Rizzo, directeur de thèse

Prof. E. Garand, rapporteur

Prof. J. Oomens, rapporteur

Prof. U. Lorenz, rapporteur



ÉCOLE POLYTECHNIQUE  
FÉDÉRALE DE LAUSANNE

Suisse  
2018



# Abstract

The pivotal theory of molecular biology states that the structure of biomolecules is directly related to their function in living systems. In this way, the structural investigation of biological molecules allows understanding and intervening in the fundamental biological processes. Furthermore, the structural characterization of isolated biomolecules in the gas phase offers the advantage of determining their intrinsic structural properties free from environment perturbations. A particularly sensitive gas-phase technique to the finest structural details of biomolecules is cryogenic infrared spectroscopy. The scope of this thesis is to determine the gas-phase structure of a range of biologically relevant molecules in the gas phase.

In the first part of this thesis we study the clustering of the amino acid serine into a protonated octamer. As a “magic number” cluster it exhibits an unusually high abundance in the gas phase and an outstanding homochiral preference. We report the structure of the protonated serine octamer determined by a combination of experimental and computational techniques: gas-phase infrared spectroscopy of the helium-tagged  $\text{Ser}_8\text{H}^+$  cluster and *ab initio* molecular dynamics simulations. The found structure is surprisingly asymmetric and explains the homochiral preference of the cluster.

In the second part, we introduce an isotopic labeling method for analyzing the conformational heterogeneity of glycans. Infrared-infrared double resonance spectroscopy performed on a helium-tagged protonated

monosaccharide provides vibrational fingerprints of individual conformers and, together with quantum mechanical computations, is used to interpret the results from isotopic labeling.

In the last part, cryogenic infrared spectroscopy gives insight into the migration of the electronic excitation between two aromatic chromophores of a model peptide. This is possible because the absorption bands in the highly-resolved infrared spectra of the excited states are sensitive to the localization of the electronic energy in each chromophore.

**Keywords:** cryogenic spectroscopy, cold ion, biomolecules, infrared, ultraviolet, conformer selective, hydrogen bonds, structure, serine, magic-number cluster, glycans, peptides.

# Kurzfassung

Der Grundstein der Molekularbiologie wird durch die enge Verknüpfung zwischen Struktur und Funktion von Biomolekülen in lebenden Systemen gebildet. Die Aufklärung dieser Strukturen ist daher essentiell um biochemische Prozesse auf molekularer Ebene verstehen oder manipulieren zu können. Für diese Aufgabe sind Gasphasenmethoden besonders gut geeignet, da hierbei Umgebungseinflüsse ausgeschlossen werden können was die Erforschung intrinsischer struktureller Eigenschaften ermöglicht. Eine besonders empfindliche Methode um isolierte Moleküle in der Gasphase zu untersuchen ist die (kryogenische) Infrarotspektroskopie. Basierend auf dieser und verwandten experimentellen Techniken werden in der vorliegenden Dissertation die Gasphasenstrukturen einer Reihe biologisch relevanter Moleküle bestimmt.

Im ersten Teil der Arbeit wird der Octamercluster der Aminosäure Serin untersucht. Das Octamer dieser Aminosäure ist mit seiner magischen Clusterzahl besonders stabil in der Gasphase und zeichnet sich zudem durch seine Homochiralität aus. Hier wird die dreidimensionale Struktur dieses interessanten protonierten Clusters durch die Kombination von Experiment und Theorie bestimmt: Gasphasen-Infrarotspektroskopie am Helium-gebundenen  $\text{Ser}_8\text{H}^+$  Cluster und *ab initio* Molecular Dynamics Simulations. Die resultierende Struktur überrascht durch seine Asymmetrie und erklärt zudem die homochirale Präferenz des Clusters.

Im zweiten Teil wird die Methode der Isotopenmarkierung eingeführt um die Heterogenität von Glycanstrukturen zu untersuchen. Konformerselektive infrarot-infrarot Doppelresonanzspektroskopie an Helium-gebundenen protonierten Monosacchariden wird in Verbindung mit Quantenchemischen Berechnungen verwendet um die Ergebnisse von Isotopenmarkierungs-Experimenten zu interpretieren.

Im letzten Teil dieser Arbeit werden mittels kryogener Infrarotspektroskopie Details über die Migration elektronisch angeregter Zustände zwischen zwei Chromophoren eines Modellpeptids erforscht. Dies ist möglich, da die Absorptionsbanden in den hochaufgelösten Infrarotspektren empfindlich auf die Verteilung elektronischer Energie in den jeweiligen Chromophoren sind.

**Stichwörter:** Kryogenische Spektroskopie, kalte Ionen, Biomoleküle, Infrarot, Ultraviolett, konformerselektiv, Wasserstoffbrückenbindung, Struktur, Serin, Magische Clusterzahl, Glycan, Peptide.

# Résumé

La théorie cruciale de biologie moléculaire affirme que la structure de biomolécules est directement liée à leurs fonctions dans les systèmes vivants. De cette façon, une investigation structurale des molécules biologiques permet une compréhension et une intervention dans les processus biologiques fondamentales. Par ailleurs, la caractérisation structurale des biomolécules isolées en phase gazeuse offre l'avantage de déterminer leurs propriétés structurales intrinsèques, sans des perturbations de l'environnement. Une technique en phase gazeuse particulièrement sensible aux détails structuraux des biomolécules est la spectroscopie infrarouge cryogénique. Le but de cette thèse est de déterminer la structure en phase gazeuse d'un ensemble de molécules biologiquement pertinent dans la phase gazeuse.

Dans la première partie de cette thèse, nous étudions le regroupement de l'acide aminé sérine pour former un octamère protoné. Ce regroupement à « nombre magique » existe en abondance inhabituellement élevé en phase gazeuse et démontre une préférence remarquable pour l'homochiralité. Nous rapportons la structure de l'octamère protoné de sérine, déterminé par une combinaison de techniques expérimentales et computationnels ; notamment la spectroscopie infrarouge en phase gazeuse du regroupement  $\text{Ser}_8\text{H}^+$  marqué à l'hélium et des simulations *ab initio* des dynamiques moléculaires. La structure trouvée est remarquablement asymétrique et explique la préférence homochirale du regroupement.

Dans la deuxième partie, nous introduisons une méthode de marquage isotopique pour analyser l'hétérogénéité conformationnel des glycanes. La spectroscopie infrarouge-infrarouge double résonance a été réalisé sur un monosaccharide protoné marqué à l'hélium pour fournir l'empreinte vibrationnel des conformères individuels et, en relation avec des computations de mécanique quantique, est utilisé pour interpréter les résultats du marquage isotopique.

Dans la dernière partie, la spectroscopie cryogénique infrarouge donne un aperçu de la migration d'une excitation électronique entre deux chromophores aromatiques d'un peptide model. Ceci est possible parce que les changements dans le spectre infrarouge très résolu de l'état excité est très sensible à la localisation de l'énergie électronique dans chaque chromophore.

**Mots clés** : spectroscopie cryogénique, ion froid, biomolécules, infrarouge, ultraviolet, conformer sélective, liaison hydrogène, structure, sérine, regroupement à nombre magique, glycanes, peptides.



# List of abbreviations

DNA – deoxyribonucleic acid

IRMPD – infrared multiple photon dissociation

IMS – ion mobility spectrometry

MS – mass spectrometry

IR – infrared

UV – ultraviolet

SA-AIMD – simulated-annealing *ab initio* molecular dynamics

CCS – collision cross section

EET – electronic energy transfer

RF – radiofrequency

CFD – continuous fluid dynamics

OPO – optical parametric oscillator

OPA – optical parametric amplifier

RRKM – Rice-Ramsperger-Kassel-Marcus

CID – collision-induced dissociation

TDM – transition dipole moment

ADC(2) – algebraic diagrammatic construction up to second order

TDDFT – time-dependent density functional theory

EOM-CCSD – equation-of-motion coupled-cluster method



# Table of contents

ABSTRACT.....	I
KURZFASSUNG .....	III
RÉSUMÉ .....	V
LIST OF ABBREVIATIONS .....	VII
TABLE OF CONTENTS.....	IX
<b>CHAPTER 1. INTRODUCTION .....</b>	<b>1</b>
1.1. SELF-ASSEMBLING OF THE PROTONATED SERINE OCTAMER.....	2
1.2. GLYCANS.....	4
1.3. ELECTRONIC ENERGY TRANSFER IN BIOLOGICAL SYSTEMS .....	6
<b>CHAPTER 2. EXPERIMENTAL APPROACH.....</b>	<b>17</b>
2.1. INSTRUMENT OVERVIEW .....	17
2.2. ELECTROSPRAY IONIZATION .....	18
2.3. ION FUNNEL.....	19
2.4. GUIDING AND TRAPPING IONS.....	22
2.4.1. <i>Multipoles</i> .....	23
2.4.2. <i>Effective potential approximation</i> .....	23
2.4.3. <i>Quadrupole mass filter</i> .....	27
2.4.4. <i>Ring electrode guide</i> .....	31
2.5. BUFFER GAS COOLING AND TAGGING .....	33
2.6. LASER SPECTROSCOPY.....	37
2.7. ION DETECTION AND SATURATION OF DETECTOR .....	41
<b>CHAPTER 3. PROTONATED SERINE OCTAMER AND ITS HOMOCHIRAL PREFERENCE</b>	<b>51</b>
3.1. MAGIC NUMBER AND HOMOCHIRAL PREFERENCE.....	53
3.2. HYDROGEN-DEUTERIUM EXCHANGE IN THE ION SOURCE .....	54

3.3.	INFRARED SPECTROSCOPY .....	55
3.4.	CYSTEINE SUBSTITUTION .....	57
3.5.	QUANTUM MECHANICAL CONFORMATIONAL SEARCH .....	59
3.6.	THEORETICAL PREDICTIONS VS. EXPERIMENT.....	65
3.7.	CRYOGENIC ION SPECTROSCOPY IN THE FINGERPRINT REGION .....	68
3.8.	CHIRAL SUBSTITUTION .....	70
3.9.	ADDITIONAL AMINO ACID SUBSTITUTIONS .....	72
3.10.	INFLUENCE OF HE TAGS ON THE SPECTRUM OF SER <sub>8</sub> H <sup>+</sup> .....	77
3.11.	IR SPECTROSCOPY OF PROTONATED SERINE OLIGOMERS.....	79
3.12.	SUMMARY.....	82
<b>CHAPTER 4. SPECTROSCOPY OF GLYCANS.....</b>		<b>93</b>
4.1.	GLUCOSAMINE AS A BENCHMARK .....	94
4.1.1.	<i>Infrared laser setup for conformer-selective spectroscopy.....</i>	<i>95</i>
4.1.2.	<i>Sample preparation.....</i>	<i>96</i>
4.1.3.	<i><sup>18</sup>O labeling at the reducing end.....</i>	<i>97</i>
4.1.4.	<i>Conformer-selective spectroscopy of He-tagged protonated glucosamine .....</i>	<i>98</i>
4.1.5.	<i>Synergistic effect and saturation of the detector.....</i>	<i>101</i>
4.1.6.	<i>Conformational space sampling .....</i>	<i>103</i>
4.1.7.	<i>Predicted structures of protonated glucosamine.....</i>	<i>104</i>
4.1.8.	<i>Power dependence and abundance of conformers .....</i>	<i>106</i>
4.2.	PROTONATED GALACTOSAMINE.....	108
4.3.	IR SPECTROSCOPY OF A DEPROTONATED PENTASACCHARIDE.....	110
4.4.	COLLISION-INDUCED DISSOCIATION .....	112
4.5.	SUMMARY.....	115
<b>CHAPTER 5. ELECTRONIC ENERGY TRANSFER .....</b>		<b>121</b>
5.1.	MODEL PEPTIDE FOR ENERGY TRANSFER STUDIES.....	122
5.2.	EXPERIMENTAL AND THEORETICAL METHODS .....	122
5.3.	ULTRAVIOLET PHOTOFRAGMENT SPECTROSCOPY.....	124
5.4.	STRUCTURAL IDENTIFICATION OF GROUND STATE CONFORMATIONS .....	126
5.5.	IR SPECTROSCOPY OF EXCITED STATES .....	129
5.6.	TRANSIENT SPECTROSCOPY.....	134
5.7.	MODELS FOR ELECTRONIC ENERGY TRANSFER .....	138

5.8.	COMPUTATIONAL RESULTS .....	140
5.9.	FRAGMENTATION FROM THE UV LASER.....	146
5.10.	SUMMARY.....	147
<b>CHAPTER 6. CONCLUSIONS .....</b>		<b>157</b>
<b>APPENDIX: CRYOGENIC INFRARED SPECTROSCOPY OF MOBILITY- SELECTED IONS .....</b>		<b>161</b>
<b>ACKNOWLEDGEMENTS.....</b>		<b>165</b>
<b>CURRICULUM VITAE .....</b>		<b>167</b>



# Chapter 1. Introduction

All living organisms thrive on earth due to their ability to transfer genetic information to the descendant generations. The genetic code – contained in the cellular nucleus, in deoxyribonucleic acid (DNA) – is deciphered and transformed into an amino acid sequence in proteins that fold into well-defined structures. A protein's structure is intimately related to the functions it fulfils in the intricate machinery of the living body, such as: (1) enzymatic catalysis, (2) receptors of metabolic signals from outside the cell, (3) defense against foreign particles, and (4) cellular structural support, etc. [1]. Extensive research showed that hydrogen bonds direct the protein folding and are largely responsible for molecular recognition (binding of substrates, effectors and inhibitors) [2]. A similar tendency was established for lectin-carbohydrate interactions, where the sugar hydroxyl groups form strong and directional hydrogen bonds with protein polar groups [3]. A common hydrogen-bond chain in lectin-sugar complex contains the sugar hydroxyl group bound to a N-H group at the oxygen moiety and a O=C group at the hydrogen moiety [4]. In this way, a change of the configuration at a single chiral center leads to a change in the hydroxyl group orientation that has a strong impact on the stability of the glycan-lectin complex.

The major goal of this thesis is to determine the structure and its correspondence with the hydrogen bonding network of amino acid clusters, peptides (short amino acid sequences) and glycans in the gas phase. For this

we employ cryogenic vibrational spectroscopy that is a sensitive probe of the hydrogen-bond strength. Gas-phase experimental results are combined with quantum mechanical computations to determine the precise 3D structure of the studied systems. The following subsections of this chapter introduce three case studies, which brightly illustrate the relation between the hydrogen bonding and the gas-phase structure of biomolecules.

### 1.1. Self-assembling of the protonated serine octamer

The protein building blocks have an astounding property: all the common amino acids share the same L chirality. This fact led scientists to hypothesize the existence of a common ancestor compound or aggregate for all the homochiral building blocks of biomolecules [5, 6]. Also, a variety of models relying on phase transitions of amino acids have emerged [7-10]. In one or another way, a progenitor chiral aggregate is the central assumption in the mentioned hypotheses. In their pioneering work, Cooks *et al.* discovered that serine – a highly abundant amino acid [11-13] – forms a stable “magic-number” cluster in the gas phase in its protonated form ( $\text{Ser}_8\text{H}^+$ ) [6] and as a dihalide complex ( $\text{Ser}_8\text{X}_2^{2-}$ , X = Cl or Br) [14]. In addition to the high stability of serine octamer clusters, they have a strong homochiral preference, which is the ground for considering the serine octamer as a potential pathway to homochirality [15]. Clemmer *et al.* applied ion mobility spectrometry (IMS) to  $\text{Ser}_8\text{H}^+$  and found a relatively small collision cross section (CCS) of  $\sim 191 \text{ \AA}^2$ , suggesting a compact structure [16]. Another remarkable observation was that up to two serine



units in the homochiral  $\text{Ser}_8\text{H}^+$  could be easily substituted with either other amino acids or serine of opposite chirality [15]. With these observations in hand, theoretical studies suggested several stable, compact structures with eight zwitterionic serines [6, 17, 18]. The majority of the proposed structures are symmetrical [6, 19, 20] and show good agreement with the observed CCS value, but they do not provide a clear reason for either the homochiral preference or the tolerated substitution of two serine units.

Spectroscopic techniques have been applied in an effort to make a more definitive structural assignment of the protonated serine octamer. Infrared (IR) spectroscopy is a particularly powerful tool for structural identification because vibrational frequencies provide critical insights into the nature of hydrogen-bonding interactions. Nevertheless, previous room-temperature IR spectroscopic studies on  $\text{Ser}_8\text{H}^+$  in the N–H and O–H stretch region ( $3000\text{--}4000\text{ cm}^{-1}$ ) [21-24] have not led to a clear structural assignment.

Apart from the experimental complications, the protonated serine octamer is a challenging case for computational methods due to an enormous pool of possible conformations of the noncovalent complex: each serine amino acid can be in its neutral or zwitterionic form. Thus, a computational method that allows migration of protons from one site to another during the conformational search is required. Moreover, the serine subunits can interact differently in the cluster through their polar groups. In this work, we use a combination of cryogenic IR messenger-tagging

spectroscopy and high-level computations to determine the structure of  $\text{Ser}_8\text{H}^+$ .

## 1.2. Glycans

Following their biological path after synthesis on ribosomes, proteins undergo post-translational modifications in the endoplasmic reticulum and Golgi apparatus [25]. A common post-translational modification in eukaryotic cells is glycosylation that is of paramount importance in protein regulation and folding; furthermore, glycans are exposed on the surface of cells for mediating cell-to-cell recognition processes [26] and are involved in triggering cellular immune response [27]. Because glycans are involved in a multitude of signaling pathways, the glycosylation pattern of pharmaceutical products can be tuned to reduce the cytotoxicity of biosynthesized drugs [28, 29]. Hence, a profound study of glycans can guide the development of a novel class of highly effective glycan-based drugs.

In contrast to DNA or proteins, glycan sequencing presents a particularly challenging task for analytical chemistry owing to the intrinsic isomeric complexity of glycans: (1) numerous monosaccharides are isomers of each other, (2) the glycosidic bond linking varies in its stereochemistry or regiochemistry, and (3) glycans can grow into branched structures. Consequently, mass spectrometry on its own is limited in determining the primary structure of glycans [30-32].

Vibrational spectroscopy shows great promise for distinguishing isomers of carbohydrates due to different hydrogen bonding patterns of

hydroxyl groups [33, 34]. For instance, conformers of monosaccharides were successfully identified by means of infrared multiple photon dissociation (IRMPD) spectroscopy [35, 36]. Likewise, Schindler *et al.* used IRMPD spectroscopy to determine the anomeric content of carbohydrates [37, 38]. However, the broad vibrational features of room-temperature ions can render the structural identification ambiguous.

Rizzo and coworkers have developed a method of glycan identification that combines cryogenic, messenger-tagging spectroscopy with ion mobility spectrometry (IMS) and mass spectrometry (MS) [33]. Cryogenic ion spectroscopy distinguishes even the slightest structural difference between glycan isomers [33, 39, 40]. However, the conformational heterogeneity of a glycan can cause the IR spectra to be less informative. A recent study by IR-IR double resonance spectroscopy highlights that carbohydrates are prone to be trapped in solution-like structures giving rise to multiple conformers in the gas phase [41].

We combine conformer-selective cryogenic IR spectroscopy, quantum mechanical computations and  $^{18}\text{O}$  isotopic substitution to determine the anomericity of a benchmark system – protonated glucosamine. IR-IR double resonance spectroscopy of helium-tagged protonated glucosamine provides vibrational fingerprints of individual conformers and the obtained experimental spectra are matched with computed structures. The facile isotopic substitution with  $^{18}\text{O}$  allows us to label glucosamine only at its reducing end.

### 1.3. Electronic energy transfer in biological systems

Autotrophic organisms convert sunlight into energy of chemical bonds in carbohydrates that serve as nutrition to heterotrophs. Efficient electronic energy transfer (EET) after sunlight capture plays a central role in photosynthesis [42]. Moreover, DNA is protected from photodamage by means of photolyase, EET being key to its functioning [43]. Accurate modeling of EET could assist in the engineering of more efficient solar cells [44, 45]. While the majority of electronic energy transfer studies are performed in solution at room temperature, the theoretical modeling of EET would significantly benefit from experiments carried out on isolated molecules at low temperature, which would allow for conformer-specific measurements. This is essential, since both the distance and orientation of the chromophores play key roles in the energy transfer efficiency. The objective of our work is to measure electronic energy transfer rates of a gas-phase peptide of well-defined geometry in a cryogenic ion trap.

Conformation-dependent electronic energy transfer in the gas phase was first demonstrated in molecular beam experiments by Chatteraj *et al.* [46]. More recently, other research groups have extended EET studies to gas-phase ions inside a mass spectrometer [47-49]. However, fluorescence detection from ions stored in an ion trap is challenging, owing to the low chromophore density and restricted angle for photon collection. Dugourd and coworkers introduced an “action-FRET” technique [50] that circumvents these obstacles by measuring the electronic energy transfer

efficiency by means of specific photofragmentation rather than by fluorescence. However, a detailed picture of the energy dissipation processes that leads to fragmentation is still lacking. We have applied a combination of cryogenic electronic and vibrational spectroscopy to get a deeper insight into the energy transfer process in a model peptide of a well-defined structure. Infrared spectroscopy turns out to be particularly sensitive to the localization of the electronic excitation of each chromophore and probes the migration of electronic energy in our experiments.

References:

1. Philip, K., E.-S. Simon, G. Vanessa, J.M. Guss, P.H. Dale, M.J. Jill, J. Alan and M.M. Jacqui, *Schaum's Outline of Biochemistry, Third Edition*. Schaum's Outline. 2011: McGraw-Hill. -1.
2. Hubbard, R.E. and M. Kamran Haider, *Hydrogen Bonds in Proteins: Role and Strength*. eLS, 2010.
3. Cocinero, E.J. and P. Çarçabal, *Carbohydrates*, in *Gas-Phase IR Spectroscopy and Structure of Biological Molecules*, A.M. Rijs and J. Oomens, Editors. 2015, Springer International Publishing: Cham. p. 299-333.
4. Weis, W.I. and K. Drickamer, *Structural Basis of Lectin-Carbohydrate Recognition*. *Annu. Rev. Biochem.*, 1996. **65**(1): p. 441-473.
5. Popa, R., *A Sequential Scenario for the Origin of Biological Chirality*. *Journal of Molecular Evolution*, 1997. **44**(2): p. 121-127.
6. Cooks, R.G., D. Zhang, K.J. Koch, F.C. Gozzo and M.N. Eberlin, *Chiroselective Self-Directed Octamerization of Serine: Implications for Homochirogenesis*. *Anal. Chem.*, 2001. **73**(15): p. 3646-3655.
7. Klussmann, M., H. Iwamura, S.P. Mathew, D.H. Wells Jr, U. Pandya, A. Armstrong and D.G. Blackmond, *Thermodynamic control of asymmetric amplification in amino acid catalysis*. *Nature*, 2006. **441**: p. 621.

8. Perry, R.H., C. Wu, M. Neftliu and R.G. Cooks, *Serine sublimates with spontaneous chiral amplification*. Chem. Commun., 2007(10): p. 1071-1073.
9. G., B.D., “*Chiral Amnesia*” as a Driving Force for Solid-Phase Homochirality. Chemistry – A European Journal, 2007. **13**(12): p. 3290-3295.
10. Blackmond, D.G. and M. Klussmann, *Spoilt for choice: assessing phase behavior models for the evolution of homochirality*. Chem. Commun., 2007(39): p. 3990-3996.
11. King, J.L. and T.H. Jukes, *Non-Darwinian Evolution*. Science, 1969. **164**(3881): p. 788-798.
12. Dyer, K.F., *The Quiet Revolution: A New Synthesis of Biological Knowledge*. Journal of Biological Education, 1971. **5**(1): p. 15-24.
13. Andre, S., R. Michael, S. Astrid, H. Matthias, S. Eileen and K. Erika, *GC content-independent amino acid patterns in Bacteria and Archaea*. Journal of Basic Microbiology, 2012. **52**(2): p. 195-205.
14. Nanita, S.C. and R.G. Cooks, *Negatively-Charged Halide Adducts of Homochiral Serine Octamers*. J. Phys. Chem. B, 2005. **109**(10): p. 4748-4753.
15. Nanita, S.C. and R.G. Cooks, *Serine Octamers: Cluster Formation, Reactions, and Implications for Biomolecule Homochirality*. Angew. Chem. Int. Ed., 2006. **45**(4): p. 554-569.

16. Counterman, A.E. and D.E. Clemmer, *Magic Number Clusters of Serine in the Gas Phase*. J. Phys. Chem. B, 2001. **105**(34): p. 8092-8096.
17. Schalley, C.A. and P. Weis, *Unusually stable magic number clusters of serine with a surprising preference for homochirality*. Int. J. Mass spectrom., 2002. **221**(1): p. 9-19.
18. Julian, R.R., R. Hodyss, B. Kinnear, M.F. Jarrold and J.L. Beauchamp, *Nanocrystalline Aggregation of Serine Detected by Electrospray Ionization Mass Spectrometry: Origin of the Stable Homochiral Gas-Phase Serine Octamer*. J. Phys. Chem. B, 2002. **106**(6): p. 1219-1228.
19. Counterman, A.E. and D.E. Clemmer, *Magic Number Clusters of Serine in the Gas Phase*. Journal of Physical Chemistry B, 2001. **105**(34): p. 8092-8096.
20. Spencer, E.A.C., T. Ly and R.R. Julian, *Formation of the serine octamer: Ion evaporation or charge residue?* Int. J. Mass spectrom., 2008. **270**(3): p. 166-172.
21. Kong, X., I.A. Tsai, S. Sabu, C.-C. Han, Y.T. Lee, H.-C. Chang, S.-Y. Tu, A.H. Kung and C.-C. Wu, *Progressive Stabilization of Zwitterionic Structures in  $[H(\text{Ser})_{2-8}]^+$  Studied by Infrared Photodissociation Spectroscopy*. Angew. Chem. Int. Ed., 2006. **45**(25): p. 4130-4134.



22. Kong, X., C. Lin, G. Infusini, H.-B. Oh, H. Jiang, K. Breuker, C.-C. Wu, O.P. Charkin, H.-C. Chang and F.W. McLafferty, *Numerous Isomers of Serine Octamer Ions Characterized by Infrared Photodissociation Spectroscopy*. ChemPhysChem, 2009. **10**(15): p. 2603-2606.
23. Sunahori, F.X., G. Yang, E.N. Kitova, J.S. Klassen and Y. Xu, *Chirality recognition of the protonated serine dimer and octamer by infrared multiphoton dissociation spectroscopy*. Phys. Chem. Chem. Phys., 2013. **15**(6): p. 1873-1886.
24. Liao, G.H., Y.J. Yang and X.L. Kong, *Chirality effects on proline-substituted serine octamers revealed by infrared photodissociation spectroscopy*. Phys. Chem. Chem. Phys., 2014. **16**(4): p. 1554-1558.
25. Varki, A., R.D. Cummings and J.D. Esko, *Essentials of Glycobiology*. 2015-2017, Cold Spring Harbor Laboratory Press: Cold Spring Harbor (NY).
26. Varki, A., *Biological roles of glycans*. Glycobiology, 2017. **27**(1): p. 3-49.
27. Rudd, P.M., T. Elliott, P. Cresswell, I.A. Wilson and R.A. Dwek, *Glycosylation and the Immune System*. Science, 2001. **291**(5512): p. 2370-2376.
28. Jefferis, R., *Glycosylation as a strategy to improve antibody-based therapeutics*. Nature Reviews Drug Discovery, 2009. **8**: p. 226.

29. Karav, S., J. German, C. Rouquié, A. Le Parc and D. Barile, *Studying Lactoferrin N-Glycosylation*. *Int. J. Mol. Sci.*, 2017. **18**(4): p. 870.
30. Hofmann, J., H.S. Hahm, P.H. Seeberger and K. Pagel, *Identification of carbohydrate anomers using ion mobility–mass spectrometry*. *Nature*, 2015. **526**: p. 241.
31. Kailemia, M.J., L.R. Ruhaak, C.B. Lebrilla and I.J. Amster, *Oligosaccharide Analysis by Mass Spectrometry: A Review of Recent Developments*. *Anal. Chem.*, 2014. **86**(1): p. 196-212.
32. Pagel, K. and D.J. Harvey, *Ion Mobility–Mass Spectrometry of Complex Carbohydrates: Collision Cross Sections of Sodiated N-linked Glycans*. *Anal. Chem.*, 2013. **85**(10): p. 5138-5145.
33. Masellis, C., N. Khanal, M.Z. Kamrath, D.E. Clemmer and T.R. Rizzo, *Cryogenic Vibrational Spectroscopy Provides Unique Fingerprints for Glycan Identification*. *J. Am. Soc. Mass. Spectrom.*, 2017. **28**(10): p. 2217-2222.
34. Mucha, E., A.I. González Flórez, M. Marianski, D.A. Thomas, W. Hoffmann, W.B. Struwe, H.S. Hahm, S. Gewinner, W. Schöllkopf, P.H. Seeberger, G. von Helden and K. Pagel, *Glycan Fingerprinting via Cold-Ion Infrared Spectroscopy*. *Angew. Chem. Int. Ed.*, 2017. **56**(37): p. 11248-11251.
35. Contreras, C.S., N.C. Polfer, J. Oomens, J.D. Steill, B. Bendiak and J.R. Eyler, *On the path to glycan conformer identification: Gas-phase study of the anomers of methyl glycosides of N-acetyl-D-glucosamine*

- and N-acetyl-D-galactosamine*. Int. J. Mass spectrom., 2012. **330-332**: p. 285-294.
36. Tan, Y., N. Zhao, J. Liu, P. Li, C.N. Stedwell, L. Yu and N.C. Polfer, *Vibrational Signatures of Isomeric Lithiated N-acetyl-D-hexosamines by Gas-Phase Infrared Multiple-Photon Dissociation (IRMPD) Spectroscopy*. J. Am. Soc. Mass. Spectrom., 2017. **28**(3): p. 539-550.
37. Schindler, B., L. Barnes, G. Renois, C. Gray, S. Chambert, S. Fort, S. Flitsch, C. Loison, A.-R. Allouche and I. Compagnon, *Anomeric memory of the glycosidic bond upon fragmentation and its consequences for carbohydrate sequencing*. Nature Communications, 2017. **8**(1): p. 973.
38. Gray, C.J., B. Schindler, L.G. Migas, M. Pičmanová, A.R. Allouche, A.P. Green, S. Mandal, M.S. Motawia, R. Sánchez-Pérez, N. Bjarnholt, B.L. Møller, A.M. Rijs, P.E. Barran, I. Compagnon, C.E. Eyers and S.L. Flitsch, *Bottom-Up Elucidation of Glycosidic Bond Stereochemistry*. Anal. Chem., 2017. **89**(8): p. 4540-4549.
39. Khanal, N., C. Masellis, M.Z. Kamrath, D.E. Clemmer and T.R. Rizzo, *Glycosaminoglycan Analysis by Cryogenic Messenger-Tagging IR Spectroscopy Combined with IMS-MS*. Anal. Chem., 2017. **89**(14): p. 7601-7606.
40. Khanal, N., C. Masellis, M.Z. Kamrath, D.E. Clemmer and T.R. Rizzo, *Cryogenic IR spectroscopy combined with ion mobility*

- spectrometry for the analysis of human milk oligosaccharides.* Analyst, 2018. **143**(8): p. 1846-1852.
41. Voss, J.M., S.J. Kregel, K.C. Fischer and E. Garand, *IR-IR Conformation Specific Spectroscopy of Na+(Glucose) Adducts.* J. Am. Soc. Mass. Spectrom., 2017.
42. Scholes, G.D., G.R. Fleming, A. Olaya-Castro and R. van Grondelle, *Lessons from Nature about Solar Light Harvesting.* Nat. Chem., 2011. **3**(10): p. 763-774.
43. Tan, C., L. Guo, Y. Ai, J. Li, L. Wang, A. Sancar, Y. Luo and D. Zhong, *Direct Determination of Resonance Energy Transfer in Photolyase: Structural Alignment for the Functional State.* J. Phys. Chem. A, 2014. **118**(45): p. 10522-10530.
44. Feron, K., W.J. Belcher, C.J. Fell and P.C. Dastoor, *Organic Solar Cells: Understanding the Role of Förster Resonance Energy Transfer.* Int. J. Mol. Sci., 2012. **13**(12): p. 17019-17047.
45. Huang, J.-S., T. Goh, X. Li, M.Y. Sfeir, E.A. Bielski, S. Tomasulo, M.L. Lee, N. Hazari and A.D. Taylor, *Polymer Bulk Heterojunction Solar Cells Employing Förster Resonance Energy Transfer.* Nat. Photonics, 2013. **7**(6): p. 479-485.
46. Chatteraj, M., B. Bal, G.L. Closs and D.H. Levy, *Conformation-Dependent Intramolecular Electronic Energy Transfer in a Molecular Beam.* J. Phys. Chem., 1991. **95**(24): p. 9666-9672.

47. Danell, A.S. and J.H. Parks, *FRET Measurements of Trapped Oligonucleotide Duplexes*. Int. J. Mass spectrom., 2003. **229**(1–2): p. 35-45.
48. Dashtiev, M., V. Azov, V. Frankevich, L. Scharfenberg and R. Zenobi, *Clear Evidence of Fluorescence Resonance Energy Transfer in Gas-Phase Ions*. J. Am. Soc. Mass. Spectrom., 2005. **16**(9): p. 1481-1487.
49. Talbot, F.O., A. Rullo, H. Yao and R.A. Jockusch, *Fluorescence Resonance Energy Transfer in Gaseous, Mass-Selected Polyproline Peptides*. J. Am. Chem. Soc., 2010. **132**(45): p. 16156-16164.
50. Daly, S., F. Poussigue, A.-L. Simon, L. MacAleese, F. Bertorelle, F. Chirot, R. Antoine and P. Dugourd, *Action-FRET: Probing the Molecular Conformation of Mass-Selected Gas-Phase Peptides with Förster Resonance Energy Transfer Detected by Acceptor-Specific Fragmentation*. Anal. Chem., 2014. **86**(17): p. 8798-8804.



## Chapter 2. Experimental approach

This section first describes the general working principle of the tandem mass spectrometer for cryogenic ion spectroscopy, on which all the experiments were performed. In the subsequent sections, the functioning of each functional component of the instrument is discussed in detail.

### 2.1. Instrument overview

Experiments are carried out in a home-built tandem mass spectrometer equipped with a cryogenic octupole ion trap [1]. Figure 2.1 shows the key components of the instrument.

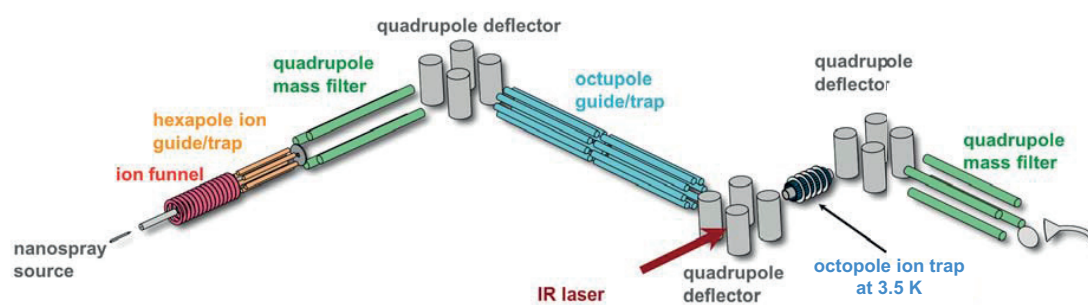


*Figure 2.1. Layout of the tandem mass spectrometer equipped with a cold octupole ion trap.*

We produce protonated gas-phase ions by electrospraying the compound of interest dissolved in a mixture of water and methanol. The ions are focused in an electrodynamic ion funnel. In order to match the continuous ion source (electrospray) with the pulsed trapping in the cryogenic ion trap, we accumulate and thermalize the electrosprayed ions

in a hexapole ion trap. Short ion packets leave the hexapole and are mass selected in a quadrupole mass filter and guided to a cryogenic octupole ion trap (cooled to 3.5 K) where they are trapped and cooled in collisions with helium buffer gas. Then, UV and/or IR laser radiation excites the trapped ions in order to perform action spectroscopy. The infrared spectra carry structural information about the investigated ion, which can be elucidated by comparing the measured spectra with those from quantum mechanical computations.

### 2.2. Electrospray ionization

The invention of electrospray ionization by John Fenn and coworkers [2] has had a great impact on the field of mass spectrometry by facilitating the volatilization of intact macromolecules. The electrospray process works as follows: by applying a high voltage to a metal coated needle filled with a solution of electrolyte a Taylor cone is formed [3], and the high electric field gradient disperses the liquid into charged drops and drives them to the entrance of the mass spectrometer (Figure 2.2). During their flight through air, solvent evaporates from the drop, and the charge density at the surface increases until the Coulomb force leads to fission of the drop into smaller droplets [4]. This process repeats until nanoscale droplets are produced. The mechanism of dry ionized molecule formation in the last phase of the electrospray process is a subject of debate [5] and is described by two main models:



- (1) *Ion evaporation model.* Small ions can be ejected from the droplet when the charge repulsion is stronger than the ion solvation. The activation barrier for ion evaporation occurs when the ion is at  $\sim 0.5$  nm distance from the droplet [4].
- (2) *Charge residue model.* Large analyte ions cannot overcome the energetic penalty for desolvation, and thus are not able to leave the charged droplet – the solvent evaporates until the dry ion is left [6]. This mechanism is common for globular proteins.

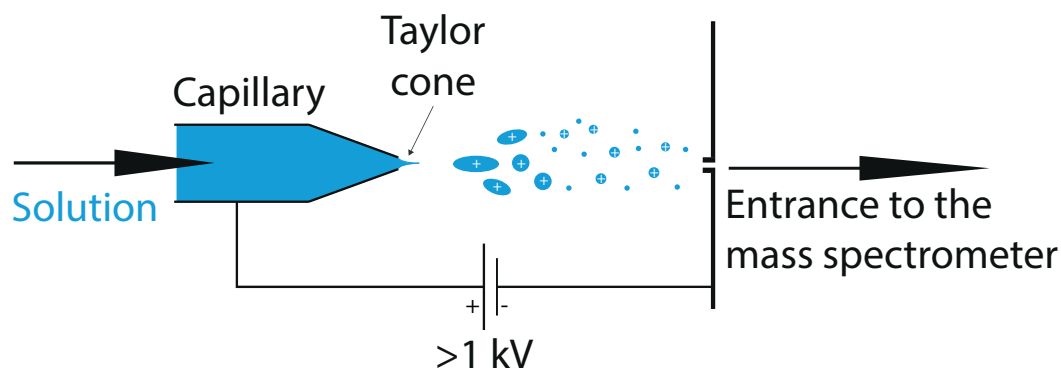
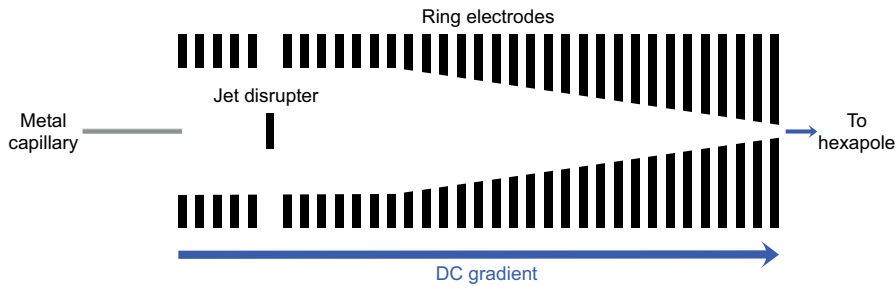


Figure 2.2. Soft ionization of large biomolecules is made possible with electro spray ionization.

### 2.3. Ion funnel

Ions produced in electro spray pass through a metal capillary into a chamber maintained at 2 mbar pressure with a scroll pump. Here the ions are focused with an electrodynamic ion funnel, which increases the throughput of ions to the next pumping stage (see Figure 2.1). The design of our ion funnel is adopted from the work of Richard Smith and coworkers

[7]. An ion funnel consists in a stack of circular electrodes that form a tapered tunnel [8]. The electrodes are operated with a radiofrequency (RF) oscillating voltage that produces a confining radial effective potential; more detailed information about RF devices follows in the next section. The driving longitudinal force is achieved with a constant voltage drop superimposed on the RF field (Figure 2.3). An additional DC electrode – referred to as a jet disrupter – is placed downstream from the capillary to reduce the load of neutrals on the next pumping stage [9]. The jet disrupter is biased such that ions flow around it, while the directed jet of neutrals and large droplets hits it and is pumped out of the funnel.



*Figure 2.3. Cartoon of an electrodynamic ion funnel with a jet disrupter.*

A continuous fluid dynamics (CFD) simulation brings insight into the carrier gas temperature after injection into the funnel chamber. The model system depicted in Figure 2.4 represents a sonic/supersonic air flow from atmosphere through a capillary into a cylindrical reservoir held at 2 mbar pressure.

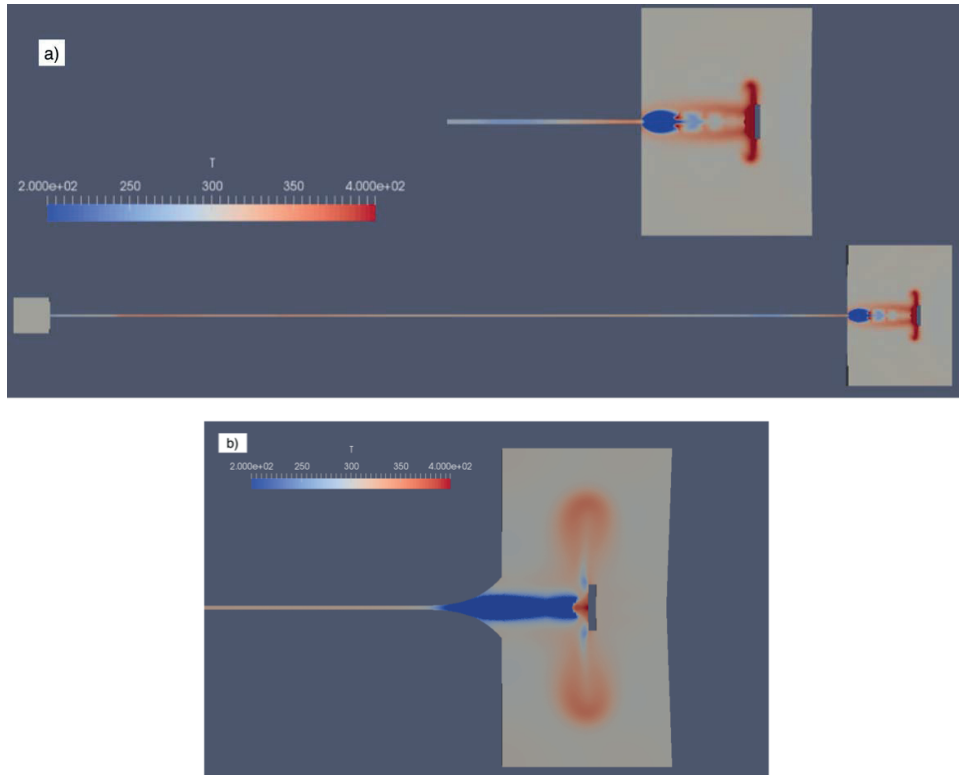


Figure 2.4. a) Temperature profile after air travels from 1 bar pressure through the straight capillary and expands into a vacuum chamber held at 2 mbar. The inset is a zoom of the vacuum chamber. b) Air expansion from a flared capillary (same temperature scale). The gas dynamics simulation is computed with OpenFOAM software: after a stable run is established in the laminar regime, the simulation is finalized in the turbulent regime.

The air jet presents shock waves and a pronounced Mach disk, consistent with similar computations [10] and experiments [11, 12]. The temperature profile strongly depends upon the geometry of the capillary outlet. In Figure 2.4a, the gas temperature after expansion from a normal capillary outlet is 20-50K higher than the background temperature. In contrast, a flared outlet of the capillary (Figure 2.4b) leads to a negligible

temperature increase in the shock waves. In the transitional pressure regime of the funnel and at a large distance from the RF electrodes, the ions undergo multiple collisions and thermalize to the temperature of the bath gas, their temperature and trajectory being strongly influenced by the carrier gas flow and compression [13]. In this way, the ions exiting a straight capillary outlet are more activated in the hot, compressed gas of the shock waves before reaching the jet disrupter, which can lead to isomerization of kinetically trapped conformers [14].

To summarize, a flared outlet of the capillary can moderately reduce the temperature of the bath gas that the ions experience at the funnel entrance and can promote a gentler transmission of ions to the next pumping stage.

### 2.4. Guiding and trapping ions

After the ions pass through the funnel, they accumulate in a hexapole device. The background pressure decreases stepwise in the hexapole from  $\sim 10^{-2}$  to  $\sim 10^{-5}$  mbar. In the higher-pressure section of the hexapole, the ions are thermalized upon collisions with the room-temperature background gas. We switch the voltage applied to the exit electrode in order to release short packets of ions. The hexapole exit electrode voltage is higher than the pole bias during 96 ms for ion accumulation; for the remaining 4 ms of a cycle, the exit electrode is lower than the hexapole pole bias to release the ions. Pretrapping in the hexapole has the advantage of reducing the ion current instability caused by the variable electrospray ionization efficiency.

In higher vacuum conditions – where the ions do not undergo frequent collisions – their motion is well-controlled by electric fields. In 1951 Wolfgang Paul proposed to manipulate ions with RF multipoles [15]. We describe below the principle of operation of RF devices with an introduction to effective potential approximation.

#### 2.4.1. Multipoles

The two-dimensional multipolar electric potential is time-dependent and is expressed in cylindrical coordinates as follows [16, 17]:

$$V(r, \phi, t) = V_0 \cos(n\phi) \left(\frac{r}{R_0}\right)^n \sin(\omega t) \quad (2.1)$$

where  $V_0$  represents the radiofrequency amplitude,  $R_0$  is the distance from each RF electrode to the origin axis,  $2n$  is the total number of electrodes, and  $\omega$  is the angular frequency. From a practical point of view, the trap is built from cylindrical rods that approximate the ideal multipole potential of Equation 2.1. To approximate the multipole potential to the first and second orders, the diameter of the rods has to fulfil the relation [17]

$$\rho = \frac{R_0}{n-1}. \quad (2.2)$$

#### 2.4.2. Effective potential approximation

The trajectory of an ion can be determined analytically only for a quadrupole ( $n=2$ ). When  $n>2$ , the system of equations of motion are coupled and nonlinear in position coordinates. For this case the effective

potential approximation largely simplifies the description of ion dynamics. Dehmelt pioneered the analysis of ion motion in RF traps in the frame of adiabatic approximation [18]. The adiabatic approximation assumes that the ion motion can be decomposed into a fast oscillation – also referred to as micromotion – and the slow change of the coordinate  $\vec{R}(t)$ , called the secular motion

$$\vec{r}(t) = \vec{R}(t) + \vec{\xi}(t). \quad (2.3)$$

Expanding the electric field at the position of the ion in a Taylor series and considering only the quickly varying terms, one finds the expression for the micromotion

$$\vec{\xi}(t) = -\frac{q\vec{E}(\vec{R})}{m\omega^2} \sin(\omega t). \quad (2.4)$$

Equation 2.4 implies that the micromotion of the charge  $\vec{\xi}(t)$  follows the RF oscillation of the electric potential. Using Equation 2.4, the expression for the secular motion becomes

$$m \frac{d^2}{dt^2} \vec{R} = -\vec{\nabla} \left( \frac{q^2}{2m\omega^2} \langle \vec{E}(\vec{R}, t)^2 \rangle \right). \quad (2.5)$$

The angled brackets indicate the time average over one oscillation period of the electric potential. It is easy to see that the slow drift motion is governed by the force of an effective potential  $V_{\text{eff}}$

$$V_{\text{eff}}(\vec{R}) = \frac{q^2}{2m\omega^2} \langle \vec{E}(\vec{R}, t)^2 \rangle = \frac{q^2}{4m\omega^2} \vec{E}(\vec{R})^2. \quad (2.6)$$

In the last relation, we averaged over one period of oscillation of the electric field. The effective potential for an infinitely long multipole (Equation 2.1) is cylindrically symmetric and is given by

$$V_{eff}(\vec{R}) = \frac{q^2 n^2 V_0^2}{4m\omega^2 R_0^2} \left(\frac{R}{R_0}\right)^{2n-2}. \quad (2.7)$$

Hence, the effective potential of a high order multipole increases more steeply with the radius  $R$ , allowing a larger nearly field-free central region (Figure 2.5). From the solution for  $\vec{\xi}(t)$ , it follows that the time-averaged kinetic energy of the micromotion equals exactly the effective potential. This demonstrates that the effective potential energy is stored in the kinetic energy of ion micromotion. In other words, the ion confinement in the multipole occurs because the kinetic energy of the drift motion is reversibly converted into the kinetic energy of the micromotion near the RF electrodes. As a consequence, ions moving in a buffer gas undergo collisional heating in regions with high effective potential because of a large amplitude micromotion. On the one hand, from Figure 2.5 it follows that the higher order multipoles are more suitable for efficient buffer gas cooling due to their larger field-free space. On the other hand, the lower order multipoles are more advantageous for confining the ions in the central part of the trap for a better overlap with the laser beam. A good compromise is the octupole ion trap, which provides both efficient cooling and radial confinement [19].

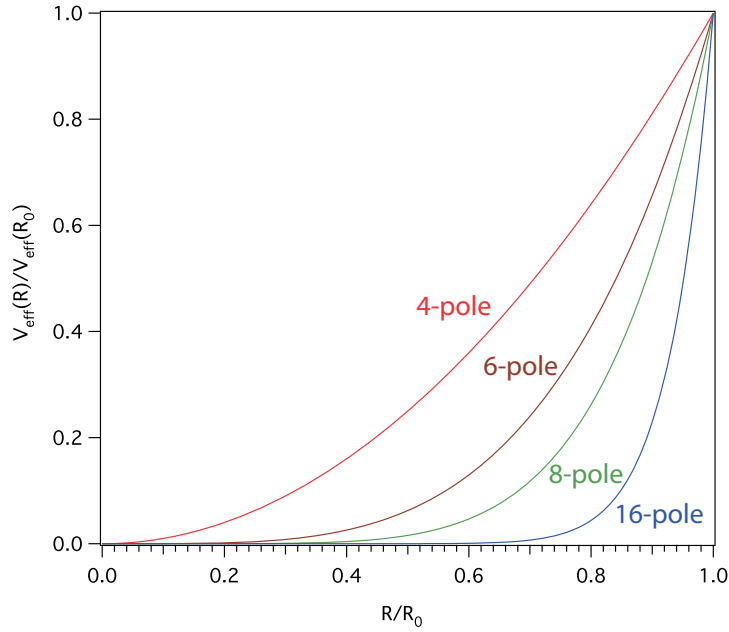


Figure 2.5. The shape of effective potentials in multipoles with  $2n=4$  (red), 6 (brown), 8 (green), and 16 (blue).

Under what conditions is the effective potential approximation valid, and the total energy – an adiabatic constant of the ion motion? Generally speaking, the total energy of an ion in RF field is not conserved. Undoubtedly, if the amplitude of the micromotion is too large, the secular motion can increase in amplitude until the ion is lost in collisions with electrodes. Such a situation is more likely to happen when the electric field amplitude changes significantly over the distance travelled by an ion during one cycle of the micromotion. The adiabaticity parameter  $\eta$  is defined as:

$$\eta = \left| \frac{2(\vec{\xi}_0 \vec{\nabla}) \vec{E}(\vec{R})}{\vec{E}(\vec{R})} \right| = \frac{2|q|}{m\omega^2} |\nabla E_0(\vec{R})|. \quad (2.8)$$



Based on an ample body of numerical simulations and experimental observations, Gerlich [17] reports that  $\eta < 0.3$  guarantees a safe operation of the ion trap, *i.e.* stability of the ion trajectory.

In the case of an ideal multipole, the adiabaticity parameter transforms into:

$$\eta = 2n(n-1) \frac{|q|V_0}{m\omega^2 R_0^2} \left(\frac{R}{R_0}\right)^{n-2}. \quad (2.9)$$

As a result,  $\eta$  does not depend on the radius of secular motion in the case of the quadrupolar field.

### 2.4.3. Quadrupole mass filter

Wolfgang Paul and Helmut Steinwedel were first to propose the quadrupole ion guide to be used as a mass filter [20]. The quadrupolar mass filters found a large demand in the field of mass spectrometry due to their relatively compact construction and absence of magnetic fields [21]. A quadrupole consists of four longitudinally aligned metallic hyperbolic electrodes (Figure 2.6a). Hyperbolic rods are usually replaced with cylindrical rods, which are easier to machine. The cylindrical rods are tangential to an imaginary circle (Figure 2.6b) and the rod radius is optimized to correctly approximate the field of an ideal multipole [22, 23]. Each pair of opposite electrodes receives a voltage  $\Phi_0$  with a constant component ( $U$ ) and a radiofrequency component ( $V$ ):

$$\Phi_0 = U + V\cos(\omega t). \quad (2.10)$$

where  $\omega$  represents the angular frequency. Voltages  $+\Phi_0$  and  $-\Phi_0$  are supplied to the two pairs of opposite electrodes; as a result, this configuration produces the electric potential described as:

$$\Phi = \Phi_0 \frac{x^2 - y^2}{r_0^2}. \quad (2.11)$$

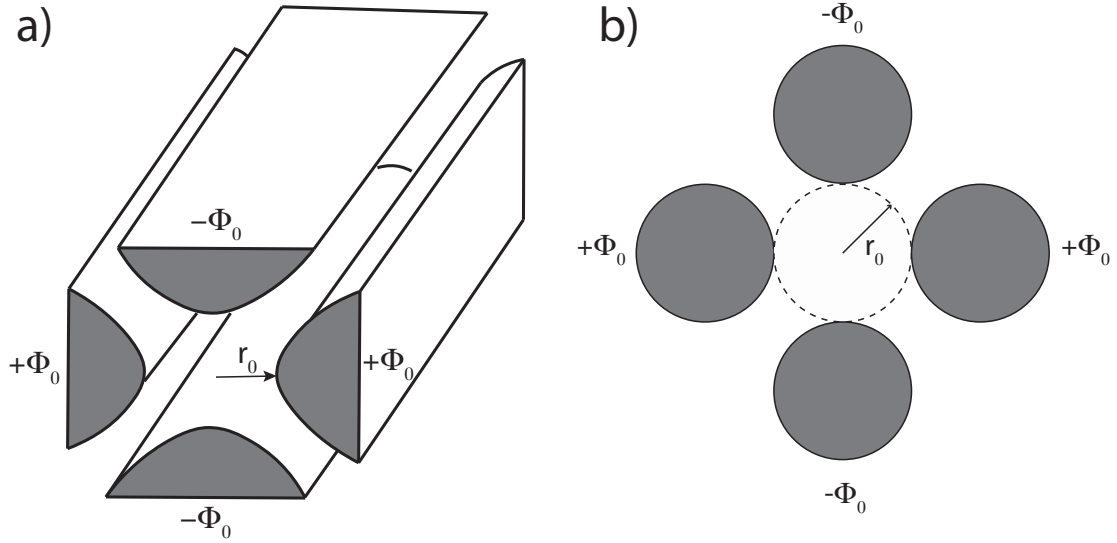


Figure 2.6. Cross section through a radiofrequency quadrupole. The hyperbolic electrodes (a) is approximated with cylindrical rods (b) [16, 24].

In an ideal quadrupolar potential, the equations of motion in each cartesian coordinate can be considered independent [24, 25]

$$\frac{d^2x}{dt^2} + \frac{2e}{mr_0^2} (U + V \cos \omega t) x = 0, \quad (2.12)$$

$$\frac{d^2y}{dt^2} - \frac{2e}{mr_0^2} (U + V \cos \omega t) y = 0, \quad (2.13)$$

$$\frac{d^2z}{dt^2} = 0, \quad (2.14)$$

where  $m$  is the mass of the ion, and  $e$  represents here the charge of the ion.

To simplify the treatment of the differential equations 2.12 and 2.13, the physical variables are substituted for their unitless analogues

$$\xi = \frac{\omega t}{2}, \quad (2.15)$$

$$a = \frac{8eU}{mr_0^2 \omega^2}, \quad (2.16)$$

$$q = \frac{4eV}{mr_0^2 \omega^2}, \quad (2.17)$$

which leads to the two equations:

$$\frac{d^2x}{d\xi^2} + (a + q \cos 2\xi) x = 0 \quad (2.18)$$

$$\frac{d^2y}{d\xi^2} - (a + q \cos 2\xi) y = 0. \quad (2.19)$$

Equations 2.18 and 2.19 represent a special type of second-order differential equations that are known as Mathieu's equations. A single ion passing through the device undergoes a motion that is a solution of these equations. The solutions of Mathieu's equations for motion in the x-y plane contain either a strictly growing exponential factor or an oscillatory term of finite radial extent, depending on the ion charge-to-mass ratio  $m/e$ . Stable solutions for the named equations can be represented on a diagram, referred to as Mathieu stability diagram (Figure 2.7). To achieve high mass resolution, the parameters  $a$  and  $q$  are chosen in the vicinity of the apex of the stability region. As a result, a choice of  $U$  and  $V$ , which fulfills the

condition  $\frac{U}{V} = \frac{a}{2q}$ , selects the ions with an *a priori* known mass-to-charge ratio.

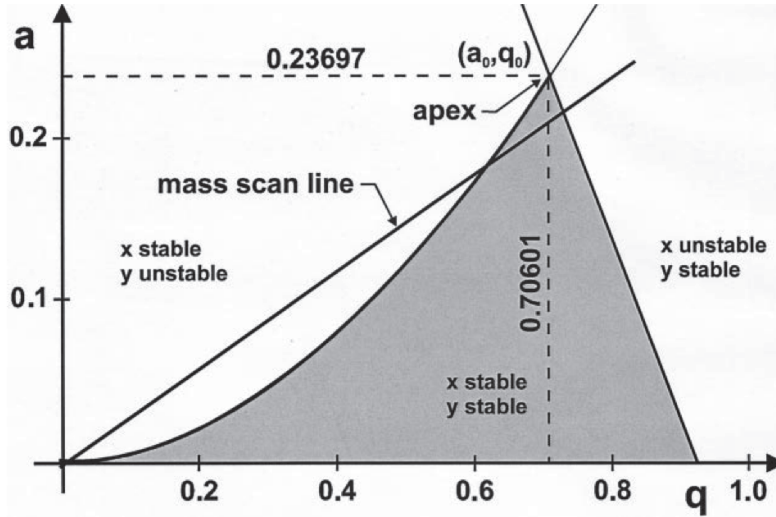


Figure 2.7. Mathieu stability diagram (gray) shown in  $a, q$ -coordinates (reproduced from [26]).

Operating the quadrupole in a highly resolving mode, *i.e.* when  $a$  and  $q$  approach  $(0.236, 0.706)$ , the stable trajectory of the corresponding ion exhibits large amplitude oscillations (Figure 2.8). Ions of higher or lower masses have unstable trajectories in the  $x$  or  $y$  direction, which leads to the loss of such ions on the quadrupole electrodes.

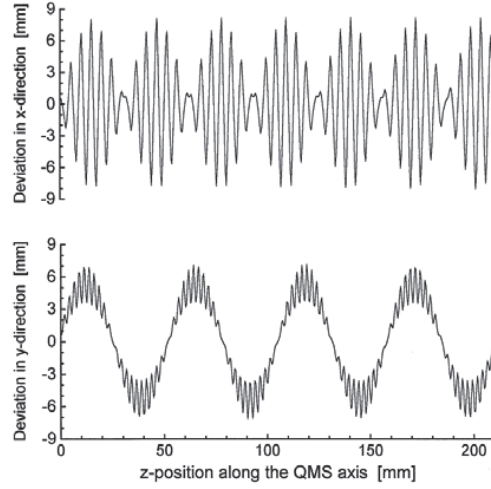


Figure 2.8. Displacement in  $x$  and  $y$  directions of a simulated stable trajectory; the distance between the center and the electrodes is 9.39 mm (reproduced from [26]).

#### 2.4.4. Ring electrode guide

The ring electrode structure is another representative case of RF devices. D. Gerlich [17, 27] and K. Asmis [28] have largely applied the ring electrode trap to kinetic and spectroscopic studies of cold ions. Moreover, the ring electrode trap has led to the development of the electrodynamic ion funnels, mainly in the group of Richard Smith [7].

The radius of an electrode is  $r_0$ , and the distance between two adjacent electrodes in the stack is  $\pi z_0$  (Figure 2.9). Alternating voltage with an amplitude of  $\Phi_0$ , applied to the ring electrodes, generates a cylindrically symmetric potential of the form:

$$\Phi(r, z, t) = \Phi_0 \sin(\omega t) \frac{I_0\left(\frac{r}{z_0}\right)}{I_0\left(\frac{r_0}{z_0}\right)} \cos \frac{z}{z_0} \quad (2.20)$$

where  $I_n(x)$  stands for the modified Bessel function of the first type, which can be expressed in its integral representation [29]:

$$I_n(z) = \frac{1}{\pi} \int_0^\pi e^{(z \cos \theta)} \cos(n\theta) d\theta \quad (2.21)$$

if  $n$  is an integer number. The effective potential for a ring electrode stack can be derived from Equations 2.6 and 2.20. The potential evaluates to:

$$V_{eff}(r, z) = \frac{q^2 V_0^2}{4m\omega^2 z_0^2} \frac{I_1^2\left(\frac{r}{z_0}\right) \cos^2\frac{z}{z_0} + I_0^2\left(\frac{r}{z_0}\right) \sin^2\frac{z}{z_0}}{I_0^2\left(\frac{r_0}{z_0}\right)}. \quad (2.22)$$

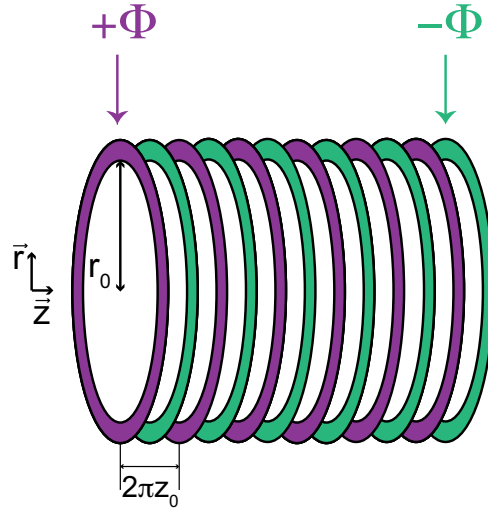


Figure 2.9. Ring electrode trap. Green and purple denote the two opposite phases of RF voltage.

A useful estimate of the effective potential can be done, if the inner radius of the ring electrodes,  $r$ , is large compared to the spacing between electrodes, i.e.  $z < r < r_0$  [30]:

$$V_{eff} \approx V_{max} \frac{r_0}{r} \exp\left(\frac{r-r_0}{z/2}\right). \quad (2.23)$$

This expression emphasizes that the effective potential of a ring electrode guide increases exponentially approaching the electrode radius  $r_0$  and leaves a large field free region inside the ring electrode trap [17, 31].

In fact, the design of an ion funnel represents a ring electrode guide, in which the internal diameter gradually decreases (Figure 2.3). The effective potential of an ion funnel switches on only in close proximity to the electrodes. Furthermore, analyzing the behavior of the effective potential on the central axis of the ion funnel, one finds that it is modulated by the period of the spacing between the electrodes [30]. This effect leads to trapping of ions in effective potential wells created along the ion funnel axis at  $z$ -positions corresponding to each exit ring electrode. The axial wells trap stronger lighter ions, producing a spurious  $m/z$ -dependent transmission of ions. This effect can be reduced by increasing the opening of the last RF electrode of the ion funnel and decrease of the interelectrode distance [8].

### 2.5. Buffer gas cooling and tagging

The hexapole releases ions in short and dense bunches that are guided into the cryogenic octupole ion trap for trapping and cooling (see machine layout in Figure 2.1). The short pulse of ions released from the hexapole improves the efficiency of trapping and cooling in the cryogenic octupole trap because a large number of ions arrive at the moment when the instantaneous pressure of helium buffer gas is the highest,  $\sim 0.5$  ms after the He pulse. After trapping and cooling, the ions can form weakly bound complexes with helium [32, 33] that we subsequently use for IR

predissociation spectroscopy (or “messenger-tagging” spectroscopy, discussed below). The timescales of trapping, cooling and helium tagging are discussed further in this section.

Anticipating the arrival of ions in the octupole ion trap, a solenoid valve opens for  $\sim 350\text{-}400\ \mu\text{s}$  and gives a burst of helium that thermalizes with the copper housing maintained at 3.5 K. Opening the pulsed valve at a repetition rate of 10 Hz, we measure  $\sim 1 \times 10^{-5}$  mbar average pressure in the vacuum chamber. Zabuga estimated the instantaneous pressure after the pulse as  $\sim 10^{-2}$  mbar ( $\sim 10^{16}\ \text{cm}^{-3}$  number density) calculating the conductance of the octupole housing and the pumping speed of the turbomolecular pump that evacuates the chamber [34]. This calculation does not take into account the adsorption/desorption of He on the trap walls, which is possible at 3.5K [35].

Wester determined that the trapped ions equilibrate their translational degrees of freedom already after 3-10 collisions with the buffer gas [16]. Given that the hard-sphere collision rate is on the order of  $10^{-6}\ \text{s}^{-1}$  at  $\sim 10^{16}\ \text{cm}^{-3}$  number density [16], the ions are trapped within a few microseconds. Significantly more – up to  $10^4$  collisions – are required to thermalize the vibrational degrees of freedom due to the lower cross section for inelastic collisions. For example, Zwier and coworkers determined by means of UV spectroscopy that a pentapeptide cools within 1 ms from room temperature to  $T_{\text{vib}} = 10\text{K}$  [36]. Energetic collisions with the buffer gas in the course of ion micromotion hinders an efficient thermalization of the



translational degrees of freedom to the bath temperature. Because the effective potential corresponds to the ion micromotion (see section “Effective potential approximation”), we can conclude that the large field-free region inside the higher order multipoles (see Figure 2.5) avoids the RF heating. Measuring the vibronic hot band intensity of TyrH<sup>+</sup>, Aseev determined that the vibrational temperature of ions in our cryogenic octupole ion trap can reach down to ~10K [37]; Lorenz measured a similar ion temperature in the 22-pole ion trap [38].

A stable He-ion cluster can be formed if the result of a two-body collision is a short-lived excited complex that releases the excess energy in a collision with the second He atom. Such a delayed three-body reaction is known as Lindemann mechanism [39]. The high instantaneous number density (about 10<sup>16</sup> cm<sup>-3</sup>) of buffer gas in our octupole leads to a substantial number of three-body collisions, which can bring about condensation of a He atom on the ion [40]. Under optimal conditions, we observe on average 10-20 % of parent ions He-tagged in our cryogenic octupole ion trap. Such a species presents an excellent candidate for “messenger-tagging” spectroscopy. Y.T. Lee pioneered this approach [41]: in which one attaches a rare gas atom [42] or H<sub>2</sub> [43] to the ion of interest and performs infrared spectroscopy on the tagged ion. The low binding energy of the tag, which is much less than the energy of the IR photon, permits recording a single photon predissociation spectrum for a variety of ions through the loss of the messenger molecule. Furthermore, the weakly bound He tag produces

minimal deviations from the vibrational spectrum of the host ion [40, 44, 45]. Another more exotic example is electronic spectroscopy of fullerene: the binding energy of one helium atom to  $C_{60}^+$  is 10 meV, which minimally perturbs the electronic spectrum of the fullerene cation [46, 47]. The dissociation energy of the cluster  $N_2^+-He$  is similar:  $\sim 12$  meV [48]. In contrast to helium, hydrogen is more polarizable, which leads to stronger interaction with the host ion and may cause noticeable shifts in the spectrum for small ions (e.g., the case of protonated glycine [49]).

The advantage of having minimal perturbation of the spectrum comes with a limitation: the low binding energy of helium demands a lower temperature of the trap for efficient tagging. Consequently, ions that have a localized charge exposed to the surface attracts He more strongly and thus tag more efficiently. The optimal operation of the instrument for efficient He tagging requires an injection of the ions into the cryogenic octupole with minimal kinetic energy: we meet this requirement by keeping a small (2-3 V) difference between the pole bias of the cold octupole and the hexapole pole bias. A low efficiency of He-tagging is observed if the octupole trap is loaded with a large number of light ions. Our interpretation of this rather counterintuitive effect is that the ions reside closer to the trap electrodes due to charge repulsion and experience excessive RF heating. The helium pulse duration needs to be long enough to provide a high gas density and to allow for numerous three-body collisions. However, at very high densities of buffer gas, the pumping system fails to sufficiently reduce the pressure

by the time the ions are extracted from the trap, and the helium tags have the potential to be lost in collisions with the buffer gas molecules during the extraction process. Aseev experimentally estimated the time constant for He pressure decay in the octupole housing as being 72 ms monitoring the reduction of the ion flux in collisions with injected He [37], such a long pump-out time gives reason for injecting the buffer gas as early as possible in the cycle. Consistent with this reasoning, the He-tagging efficiency monotonously increases as a function of the ion storage time in the octupole trap (Figure 2.10). A minimal voltage drop in the octupole trap region also allows us to extract more efficiently the tagged ions.

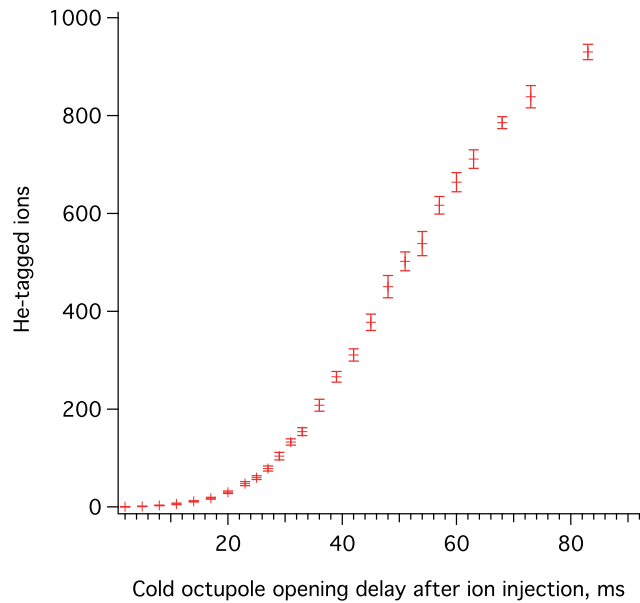


*Figure 2.10. Number of He-tagged ions are plotted as a function of the storage time in our octupole trap.*

## 2.6. Laser spectroscopy

The goal of the employed technique is to acquire infrared spectra of the cold ions that are confined in an ion trap. In conventional direct absorption IR spectroscopy, light passes through a cell containing a rather large concentration of absorbing molecules, and as a result, the light beam transmitted through the sample is attenuated. Let's consider a light beam that passes through a sample of infinitely small thickness  $dz$ . The decrease of light flux  $d\Phi$  is directly proportional to the absorption cross section  $\sigma$ , the number density of absorbing centers  $n$ , and the incoming flux  $\Phi$ :

$$\frac{d\Phi}{dz} = -n\sigma\Phi. \quad (2.24)$$

The Lambert–Beer law is the integrated form of the Equation 2.24:

$$\frac{\Phi}{\Phi_0} = e^{-\sigma nL}. \quad (2.25)$$

where  $L$  is the total thickness of the sample,  $\Phi_0$  is the incident light flux and  $\Phi$  is the flux after the cell.

The density of ions in a trap is limited by the space-charge effect ( $\sim 10^7 \text{ cm}^{-3}$  [50]), which does not produce any measurable depletion of light flux. Instead of relying on conventional absorption spectroscopy, we observe the changes in ions after they absorbed light, which is referred to as “action” spectroscopy. Because the light flux is not significantly attenuated, inverting Equation 2.24 we obtain:

$$\frac{dN_{ion}}{dz} = -\rho_{ph}\sigma N_{ion}, \quad (2.26)$$

where  $N_{ion}$  represents the number of ions in the trap,  $\rho_{ph}$  is the density of photons in the laser beam, and  $\sigma$  is the same absorption cross section as in Equation 2.24. Now the integration by  $dz$  is done over the length of the laser pulse that renders the expression:

$$\frac{N_{ion}}{N_{ion,0}} = e^{-\sigma F}, \quad (2.27)$$

where  $F$  is the laser fluence (i.e. the number of incident photons per unit area). If the product  $\sigma F \ll 1$ , Equation 2.27 can be approximated with:

$$\frac{N_{ion}}{N_{ion,0}} = \sigma F. \quad (2.28)$$

Thus, if the fluence is kept at a low level, the measured intensity of the bands reflects their relative absorption cross sections  $\sigma$ . Such spectra are referred to as linear spectra.

We implement a variety of spectroscopic schemes that rely on the “action” of the excited ions. In one set of experiments, we use messenger-tagging spectroscopy. The He-tagged ions are irradiated with an infrared (IR) pulse from a tunable optical parametric oscillator/amplifier system (OPO/OPA), in future denoted as OPO for simplicity. When the OPO light is in resonance with a vibrational transition, IR radiation is absorbed and then redistributed. Once the vibrational energy concentrates on the dissociation coordinate, He detachment occurs. According to Rice-Ramsperger-Kassel-Marcus (RRKM) theory [51, 52], the population of the critical mode happens very frequently and is only weakly dependent on the

total number of degrees of freedom due to its particularly small depth of  $\sim 100 \text{ cm}^{-1}$ . Monitoring the depletion of the tagged ions as a function of the OPO wavenumber allows one to acquire an infrared action spectrum, which is equivalent to the absorption spectrum in a wide range of molecular sizes.

In order to obtain infrared spectra of individual conformers, a second IR pulse is added after  $1 \mu\text{s}$  delay. The pump IR OPO (firing at 5 Hz) is fixed at a frequency specific for one conformer and the probe IR OPO (firing at 10 Hz) is scanned [53]. Because the probe IR induces depletion only when in resonance with any other conformer [40], the difference of the cycle with and without probe laser leads to a dip spectrum of the pumped conformer. The fluence of the pump IR pulse is increased to fully saturate the transition of a given conformer.

In the second spectroscopic scheme we excite chromophore-containing peptide ions with ultraviolet (UV) light and perform photofragment spectroscopy. If the UV radiation is in resonance with a vibronic transition in the ion, the absorbed energy is enough to cleave a covalent bond in the molecule and produce fragment ions. The fragments are mass analyzed in the second quadrupole and are detected with a channeltron.

The IR-UV double resonance technique allows us to assign infrared spectra to each peak in the electronic spectrum. This technique consists in exciting the cold ions with a tunable IR laser 100 ns before the UV laser, thus producing depletion in the UV-induced fragmentation yield. For further details the reader is referred to article [54].

We perform excited state spectroscopy promoting a conformer to a vibronic state with UV radiation and probing it after a certain delay with an IR laser. Resonant IR absorption leads to enhancement in photofragment signal that corresponds to the tyrosine side chain loss channel. This scheme has been characterized in a previous study done in our laboratory [55].

### 2.7. Ion detection and saturation of detector

Ions from the cryogenic trap are detected in counting mode with a channel electron multiplier (channeltron) equipped with a conversion dynode (DeTech, 402-A-H). For positive ion detection, the conversion dynode is biased to -5 kV, the entrance of the channel electron multiplier (a continuous dynode) is at -1.9 kV, and the exit is at ground potential. When an ion reaches the detector, it strikes the conversion dynode with high energy and emits secondary electrons. These electrons collide with the continuous dynode, leading to an avalanche of secondary emission, which is collected at the rear end of the channeltron. A preamplifier (MTS-100) is used to transform the weak current produced by the secondary electrons into a 5 V pulse with a duration of  $\sim 20$  ns.

In the usual operating conditions of the instrument, the ions arrive at the channeltron in time window of a few  $\mu\text{s}$ . At high ion currents, two ions can reach the detector in less than 20 ns, giving one count signal. This nonlinear response of the channeltron is known as detector saturation. If this situation is reached, the output signal is no longer a linear function of the ion current.

When the channeltron is operated in negative-ion mode, the voltages are changed to +500 V on the collision dynode to steer negatively charged ions directly to the channeltron entrance, which is biased to +1.9 kV. The channeltron exit is floated at +3.8 kV together with the signal line.



## References

1. Svendsen, A., U.J. Lorenz, O.V. Boyarkin and T.R. Rizzo, *A new tandem mass spectrometer for photofragment spectroscopy of cold, gas-phase molecular ions*. Rev. Sci. Instrum., 2010. **81**(7): p. 073107.
2. Yamashita, M. and J.B. Fenn, *Electrospray ion source. Another variation on the free-jet theme*. J. Phys. Chem., 1984. **88**(20): p. 4451-4459.
3. *Disintegration of water drops in an electric field*. Proceedings of the Royal Society of London. Series A. Mathematical and Physical Sciences, 1964. **280**(1382): p. 383-397.
4. Kebarle, P., *A brief overview of the present status of the mechanisms involved in electrospray mass spectrometry*. J. Mass Spectrom., 2000. **35**(7): p. 804-817.
5. Kebarle, P. and M. Peschke, *On the mechanisms by which the charged droplets produced by electrospray lead to gas phase ions*. Anal. Chim. Acta, 2000. **406**(1): p. 11-35.
6. Fernandez de la Mora, J., *Electrospray ionization of large multiply charged species proceeds via Dole's charged residue mechanism*. Anal. Chim. Acta, 2000. **406**(1): p. 93-104.
7. Shaffer, S.A., K. Tang, G.A. Anderson, D.C. Prior, H.R. Udseth and R.D. Smith, *A novel ion funnel for focusing ions at elevated pressure using electrospray ionization mass spectrometry*. Rapid Commun. Mass Spectrom., 1997. **11**(16): p. 1813-1817.

8. Kim, T., A.V. Tolmachev, R. Harkewicz, D.C. Prior, G. Anderson, H.R. Udseth, R.D. Smith, T.H. Bailey, S. Rakov and J.H. Futrell, *Design and Implementation of a New Electrodynamic Ion Funnel*. Anal. Chem., 2000. **72**(10): p. 2247-2255.
9. Kim, T., K. Tang, H.R. Udseth and R.D. Smith, *A Multicapillary Inlet Jet Disruption Electrodynamic Ion Funnel Interface for Improved Sensitivity Using Atmospheric Pressure Ion Sources*. Anal. Chem., 2001. **73**(17): p. 4162-4170.
10. Eric, T., A.J. Mark, G. Rasim and S. Rudy, *Enhanced simulation of an RF ion funnel including gas turbulence*. J. Mass Spectrom., 2015. **50**(1): p. 206-211.
11. Campargue, R., *Progress in overexpanded supersonic jets and skimmed molecular beams in free-jet zones of silence*. J. Phys. Chem., 1984. **88**(20): p. 4466-4474.
12. Powell, A., *The sound-producing oscillations of round underexpanded jets impinging on normal plates*. The Journal of the Acoustical Society of America, 1988. **83**(2): p. 515-533.
13. Tolmachev, A.V., A.N. Vilkov, B. Bogdanov, L. PĀsa-Tolić, C.D. Masselon and R.D. Smith, *Collisional activation of ions in RF ion traps and ion guides: The effective ion temperature treatment*. J. Am. Soc. Mass. Spectrom., 2004. **15**(11): p. 1616-1628.
14. Voronina, L., A. Masson, M. Kamrath, F. Schubert, D. Clemmer, C. Baldauf and T. Rizzo, *Conformations of Prolyl–Peptide Bonds in the*

- Bradykinin 1–5 Fragment in Solution and in the Gas Phase*. J. Am. Chem. Soc., 2016. **138**(29): p. 9224-9233.
15. Friedburg, H. and W. Paul, *Optische Abbildung mit neutralen Atomen*. Naturwissenschaften, 1951. **38**(7): p. 159-160.
  16. Roland, W., *Radiofrequency multipole traps: tools for spectroscopy and dynamics of cold molecular ions*. Journal of Physics B: Atomic, Molecular and Optical Physics, 2009. **42**(15): p. 154001.
  17. Gerlich, D., *Inhomogeneous RF fields*, in *Adv. Chem. Phys.* 1992. p. 1-176.
  18. Dehmelt, H.G., *Radiofrequency Spectroscopy of Stored Ions I: Storage*, in *Advances in Atomic and Molecular Physics*, D.R. Bates and I. Estermann, Editors. 1968, Academic Press. p. 53-72.
  19. Boyarkin, O.V. and V. Kopysov, *Cryogenically cooled octupole ion trap for spectroscopy of biomolecular ions*. Rev. Sci. Instrum., 2014. **85**(3): p. 033105.
  20. Paul, W. and H. Steinwedel, *Notizen: Ein neues Massenspektrometer ohne Magnetfeld*, in *Zeitschrift für Naturforschung A*1953. p. 448.
  21. Paul, W., H.P. Reinhard and U. von Zahn, *Das elektrische Massenfilter als Massenspektrometer und Isotopentrenner*. Zeitschrift für Physik, 1958. **152**(2): p. 143-182.
  22. Dawson, P.H. and N.R. Whetten, *Quadrupole Mass Filter: Circular Rods and Peak Shapes*. Journal of Vacuum Science and Technology, 1970. **7**(3): p. 440-441.

23. Gibson, J.R. and S. Taylor, *Prediction of quadrupole mass filter performance for hyperbolic and circular cross section electrodes*. Rapid Commun. Mass Spectrom., 2000. **14**(18): p. 1669-1673.
24. Campana, J.E., *Elementary theory of the quadrupole mass filter*. International Journal of Mass Spectrometry and Ion Physics, 1980. **33**(2): p. 101-117.
25. Hiroki, S., T. Abe and Y. Murakami, *Development of a quadrupole mass spectrometer using the second stable zone in Mathieu's stability diagram*. Rev. Sci. Instrum., 1991. **62**(9): p. 2121-2124.
26. Blaum, K., C. Geppert, P. Müller, W. Nörtershäuser, E.W. Otten, A. Schmitt, N. Trautmann, K. Wendt and B.A. Bushaw, *Properties and performance of a quadrupole mass filter used for resonance ionization mass spectrometry*. Int. J. Mass spectrom., 1998. **181**(1): p. 67-87.
27. Luca, A., S. Schlemmer, I. Čermák and D. Gerlich, *On the combination of a linear field free trap with a time-of-flight mass spectrometer*. Rev. Sci. Instrum., 2001. **72**(7): p. 2900-2908.
28. Goebbert, D.J., G. Meijer and K.R. Asmis, *10 K Ring Electrode Trap—Tandem Mass Spectrometer for Infrared Spectroscopy of Mass Selected Ions*. AIP Conference Proceedings, 2009. **1104**(1): p. 22-29.
29. Abramowitz, M., *Handbook of Mathematical Functions, With Formulas, Graphs, and Mathematical Tables*. 1974: Dover Publications, Inc.

30. T., K.R., T.A. V., P.J. S., T. Keqi and S.R. D., *The ion funnel: Theory, implementations, and applications*. Mass Spectrom. Rev., 2010. **29**(2): p. 294-312.
31. Tolmachev, A.V., T. Kim, H.R. Udseth, R.D. Smith, T.H. Bailey and J.H. Futrell, *Simulation-based optimization of the electrodynamic ion funnel for high sensitivity electrospray ionization mass spectrometry*. Int. J. Mass spectrom., 2000. **203**(1): p. 31-47.
32. Brümmer, M., C. Kaposta, G. Santambrogio and K.R. Asmis, *Formation and photodepletion of cluster ion-messenger atom complexes in a cold ion trap: Infrared spectroscopy of VO<sup>+</sup>, VO<sub>2</sub><sup>+</sup>, and VO<sub>3</sub><sup>+</sup>*. J. Chem. Phys., 2003. **119**(24): p. 12700-12703.
33. Asvany, O., S. Brünken, L. Kluge and S. Schlemmer, *COLTRAP: a 22-pole ion trapping machine for spectroscopy at 4 K*. Appl. Phys. B, 2014. **114**(1): p. 203-211.
34. Zabuga, A., *Dynamics of UV-excited, protonated peptides in the gas phase*, 2014, EPFL.
35. Pereverzev, A., *Multilaser Conformer-Selective Spectroscopy of Cold Biomolecular Ions in the Gas Phase*, 2017, EPFL.
36. Harrilal, C.P., A.F. DeBlase, J.L. Fischer, J.T. Lawler, S.A. McLuckey and T.S. Zwier, *Infrared Population Transfer Spectroscopy of Cryo-Cooled Ions: Quantitative Tests of the Effects of Collisional Cooling on the Room Temperature Conformer Populations*. J. Phys. Chem. A, 2018. **122**(8): p. 2096-2107.

37. Asev, O., *Spectroscopic studies of peptide fragments produced by collision-induced dissociation*, 2014, EPFL.
38. Lorenz, U., *Spectroscopy of Cold, Biomolecular Ions: Instrumentation and Application*, 2011, EPFL.
39. Croft, J.F.E. and J.L. Bohn, *Non-sticking of helium buffer gas to hydrocarbons*. Physical Review A, 2015. **91**(3): p. 032706.
40. Jašík, J., D. Gerlich and J. Roithová, *Two-Color Infrared Predissociation Spectroscopy of C<sub>6</sub>H<sub>6</sub><sup>2+</sup> Isomers Using Helium Tagging*. J. Phys. Chem. A, 2015. **119**(11): p. 2532-2542.
41. Lisy, J.M., *Infrared studies of ionic clusters: The influence of Yuan T. Lee*. J. Chem. Phys., 2006. **125**(13): p. 132302.
42. Boo, D.W. and Y.T. Lee, *Vibrational spectroscopy and dynamics of ionic complexes of CH<sub>5</sub><sup>+</sup>, CH<sub>5</sub><sup>+</sup>(A)<sub>x</sub>(B)<sub>y</sub> (A, B = Ar, N<sub>2</sub>, CH<sub>4</sub>; x, y = 0–5)*. Int. J. Mass Spectrom. Ion Processes, 1996. **159**(1): p. 209-229.
43. Okumura, M., L.I. Yeh, J.D. Myers and Y.T. Lee, *Infrared spectra of the cluster ions H<sub>7</sub>O<sup>+</sup>+3·H<sub>2</sub> and H<sub>9</sub>O<sup>+</sup>+4·H<sub>2</sub>*. J. Chem. Phys., 1986. **85**(4): p. 2328-2329.
44. Roithová, J., A. Gray, E. Andris, J. Jašík and D. Gerlich, *Helium Tagging Infrared Photodissociation Spectroscopy of Reactive Ions*. Acc. Chem. Res., 2016. **49**(2): p. 223-230.
45. Kelleher, P.J., C.J. Johnson, J.A. Fournier, M.A. Johnson and A.B. McCoy, *Persistence of Dual Free Internal Rotation in*

- NH<sub>4</sub><sup>+</sup>(H<sub>2</sub>O) · He<sub>n=0-3</sub> Ion-Molecule Complexes: Expanding the Case for Quantum Delocalization in He Tagging.* J. Phys. Chem. A, 2015. **119**(18): p. 4170-4176.
46. Kuhn, M., M. Renzler, J. Postler, S. Ralser, S. Spieler, M. Simpson, H. Linnartz, A.G.G.M. Tielens, J. Cami, A. Mauracher, Y. Wang, M. Alcamí, F. Martín, M.K. Beyer, R. Wester, A. Lindinger and P. Scheier, *Atomically resolved phase transition of fullerene cations solvated in helium droplets.* Nature Communications, 2016. **7**: p. 13550.
47. Leidlmair, C., Y. Wang, P. Bartl, H. Schöbel, S. Denifl, M. Probst, M. Alcamí, F. Martín, H. Zettergren, K. Hansen, O. Echt and P. Scheier, *Structures, Energetics, and Dynamics of Helium Adsorbed on Isolated Fullerene Ions.* Phys. Rev. Lett., 2012. **108**(7): p. 076101.
48. Bieske, E.J., A.M. Soliva, A. Friedmann and J.P. Maier, *Electronic spectra of N+2-(He)<sub>n</sub> (n=1, 2, 3).* J. Chem. Phys., 1992. **96**(1): p. 28-34.
49. Masson, A., E.R. Williams and T.R. Rizzo, *Molecular hydrogen messengers can lead to structural infidelity: A cautionary tale of protonated glycine.* J. Chem. Phys., 2015. **143**(10): p. 104313.
50. Majima, T., G. Santambrogio, C. Bartels, A. Terasaki, T. Kondow, J. Meinen and T. Leisner, *Spatial distribution of ions in a linear octopole radio-frequency ion trap in the space-charge limit.* Physical Review A, 2012. **85**(5): p. 053414.

51. Kassel, L.S., *Studies in Homogeneous Gas Reactions. I.* J. Phys. Chem., 1927. **32**(2): p. 225-242.
52. Steinfeld, J.I., J.S. Francisco and W.L. Hase, *Chemical Kinetics and Dynamics.* 1989: Prentice Hall.
53. Pereverzev, A.Y., X. Cheng, N.S. Nagornova, D.L. Reese, R.P. Steele and O.V. Boyarkin, *Vibrational Signatures of Conformer-Specific Intramolecular Interactions in Protonated Tryptophan.* J. Phys. Chem. A, 2016. **120**(28): p. 5598-5608.
54. Nagornova, N.S., T.R. Rizzo and O.V. Boyarkin, *Cover Picture: Exploring the Mechanism of IR-UV Double-Resonance for Quantitative Spectroscopy of Protonated Polypeptides and Proteins (Angew. Chem. Int. Ed. 23/2013).* Angew. Chem. Int. Ed., 2013. **52**(23): p. 5887-5887.
55. Zabuga, A.V., M.Z. Kamrath, O.V. Boyarkin and T.R. Rizzo, *Fragmentation Mechanism of UV-excited Peptides in the Gas Phase.* J. Chem. Phys., 2014. **141**(15): p. 154309.



# Chapter 3. Protonated serine octamer and its homochiral preference<sup>1</sup>

Enhanced intensities for certain sizes of specific atomic, molecular or ionic clusters in mass spectra are indicative of species with unusually high stabilities and, in many cases, special geometries. Well-known examples are fullerenes [1], icosahedral rare gas clusters [2] or metallocarbohedranes [3]. While amino acids have the tendency to self-assemble when produced in the gas phase by electrospray ionization (ESI), in most cases, the intensity distributions in the mass spectrum vary smoothly with cluster size, suggesting a smooth and continuous evolution of properties [4, 5]. However, clusters of the amino acid serine behave differently. Some time ago, it was observed that the ESI mass spectra of solutions containing serine yield either cationic or anionic serine octamer clusters of exceptional abundance relative to their neighboring clusters. The first of these observations was on the protonated serine octamer ( $\text{Ser}_8\text{H}^+$ ) [6-9], followed by several alkali ion complexed octamers such as  $\text{Ser}_8\text{Li}^+$  and  $\text{Ser}_8\text{Na}^+$  [10]. An additional striking property of serine octamer clusters is their homochiral preference. When D- and L-serine are mixed, the resulting octamer ions do not contain

---

<sup>1</sup> The content of this chapter is partially based on the material from the article: V. Scutelnic, M. Perez, M. Marianski, S. Warnke, A. Gregor, U. Rothlisberger, M. T. Bowers, C. Baldauf, G. von Helden, T. R. Rizzo, and J. Seo: "The structure of the protonated serine octamer", JACS, 2018. It is available online at: <https://pubs.acs.org/doi/abs/10.1021/jacs.8b02118>

a statistical distribution of the two but prefer eight serines of the same chirality, and this has led to the suggestion that such clusters may have played a role in homochirogenesis [11-18].

These observations triggered numerous experimental and theoretical studies aimed at revealing the special structures of serine octamer ions, most of which focused on the protonated species,  $\text{Ser}_8\text{H}^+$ . For example, ion mobility spectrometry (IMS) has been applied to  $\text{Ser}_8\text{H}^+$ , and its relatively small collision cross section (CCS) ( $191 \text{ \AA}^2$  and  $187 \text{ \AA}^2$ ) [7, 9] suggested a compact structure. Another notable experimental observation is that up to two serine units in the homochiral  $\text{Ser}_8\text{H}^+$  can be easily substituted with either other amino acids, or serine of opposite chirality [11, 15, 19-21]. Several stable, compact structures with eight zwitterionic serines have been proposed to explain these experimental observations [7, 9, 22]. For example, Counterman and Clemmer proposed a tightly packed, distorted block-like octamer, consisting of seven zwitterionic serines with the eighth having a protonated amine and a neutral carboxylic acid [7]. Julian *et al.* suggested a zwitterionic structure as well, but one in which eight serines form a flattened cube consisting of two tetramer units with eight points of contact between them [9]. Schalley and Weis further explored the conformational space and proposed another zwitterionic flattened cube type structure that contains chains of  $\text{O-H}\cdots\text{O}$  hydrogen bonds between the hydroxyl side chain and the carboxylate of an adjacent serine [22]. While all of these proposed structures for  $\text{Ser}_8\text{H}^+$  show good agreement with the observed CCS value,

none of them provide a clear reason for either the homochiral preference or the facile substitution of two serine units.

Despite major efforts in performing room-temperature infrared (IR) spectroscopy on  $\text{Ser}_8\text{H}^+$  in the N–H and O–H stretching region [23-25], a clear structural assignment had not yet been achieved. The chirally selective aggregation observed for the protonated serine octamer in the gas phase suggests the presence of a specific and highly stable structure.

In this chapter, we determine this structure by means of cryogenic IR spectroscopy and quantum mechanical computations [26]. Cryogenic IR spectroscopy is a unique tool for structural elucidation of the protonated serine octamer because it provides well-resolved vibrational bands that are highly sensitive to the nature of hydrogen-bonding interactions. Simulated annealing *ab initio* molecular dynamics is used to identify a low-energy conformer that is consistent with all the experimental findings.

### 3.1. Magic number and homochiral preference

First, we verify that under the experimental conditions of our laboratory, the relative abundance of  $\text{Ser}_8\text{H}^+$  is consistent with previous studies [6, 27]. The mass spectrum in Figure 3.1a indeed exhibits an exceptionally abundant octamer. Moreover, the mass spectrum obtained by spraying a 50:50 mixture of D- and L-serine- $^{13}\text{C}_3,^{15}\text{N}_1$  (Figure 3.1b) demonstrates its strong homochiral preference.

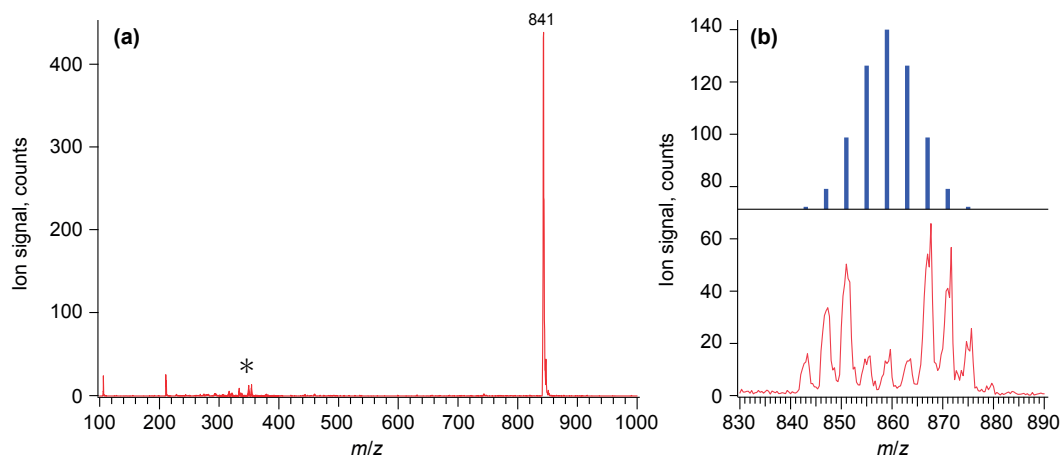


Figure 3.1. a) Mass spectrum of the acidified serine solution (5 mM); the peaks indicated with an asterisk are electrospray impurities. b) Mass spectrum of the mixture of D- and isotopically labeled L-serine compared with a statistical distribution.

### 3.2. Hydrogen-deuterium exchange in the ion source

Using hydrogen-deuterium exchange, we observe a unimodal distribution when exchanging protons with water vapor in the source background gas (Figure 3.2), suggesting that only a single structure is produced by electrospray. This is in contrast to the experiments of Takats *et al.* [20] in which they identified two structures of the serine octamer that exchange protons with water vapor at different rates.

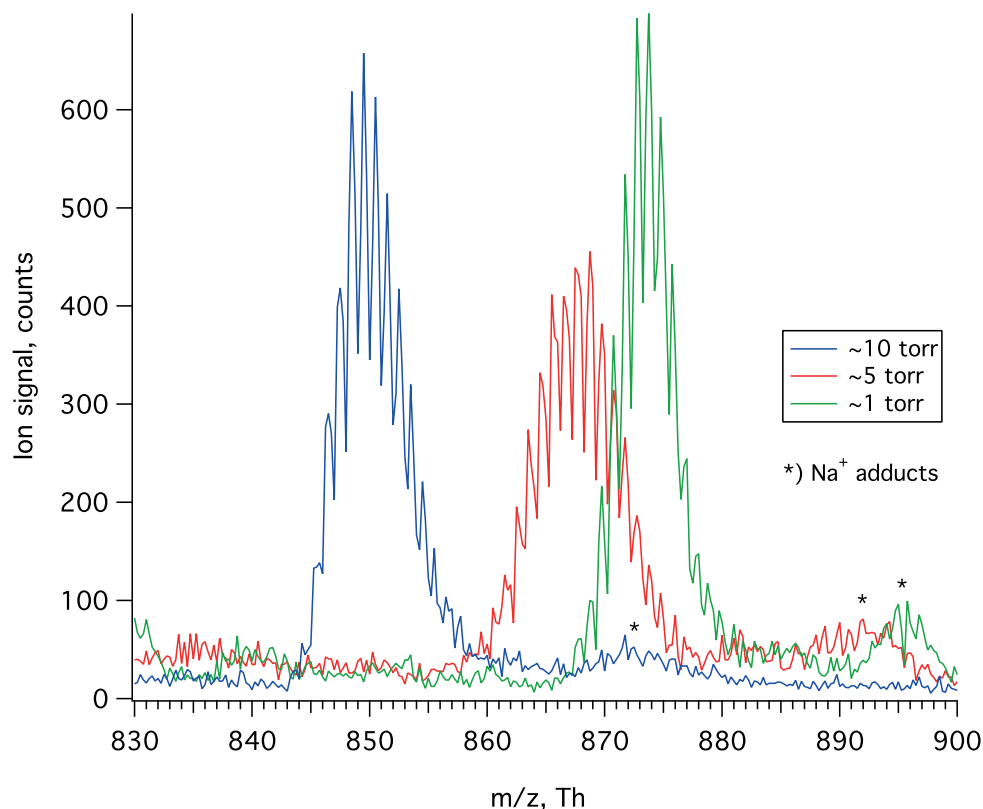


Figure 3.2. *H/D exchange of deuterated  $\text{Ser}_8\text{H}^+$  at different water vapor pressures gives rise to a unimodal distribution.*

### 3.3. Infrared spectroscopy

The IR spectrum of the He-tagged  $\text{Ser}_8\text{H}^+$  in the 2900–3700  $\text{cm}^{-1}$  region is shown in Figure 3.3. The spectrum displays broad features in the region 2900–3200  $\text{cm}^{-1}$  and four sharp peaks appearing at 3317, 3358, 3395, and 3677  $\text{cm}^{-1}$ . We assign the sharp lines by labeling the serine amine group with  $^{15}\text{N}$  or the carboxylic acid with  $^{18}\text{O}$ . Nitrogen-15 labeling shifts the peak at 3317  $\text{cm}^{-1}$  (Figure 3.4), confirming its assignment as an N–H stretch band. The sharp bands at 3358, 3395, and 3677  $\text{cm}^{-1}$  do not shift upon either  $^{15}\text{N}$

or  $^{18}\text{O}$  substitution, indicating that they correspond to O–H stretching modes of the serine hydroxyl side-chain.

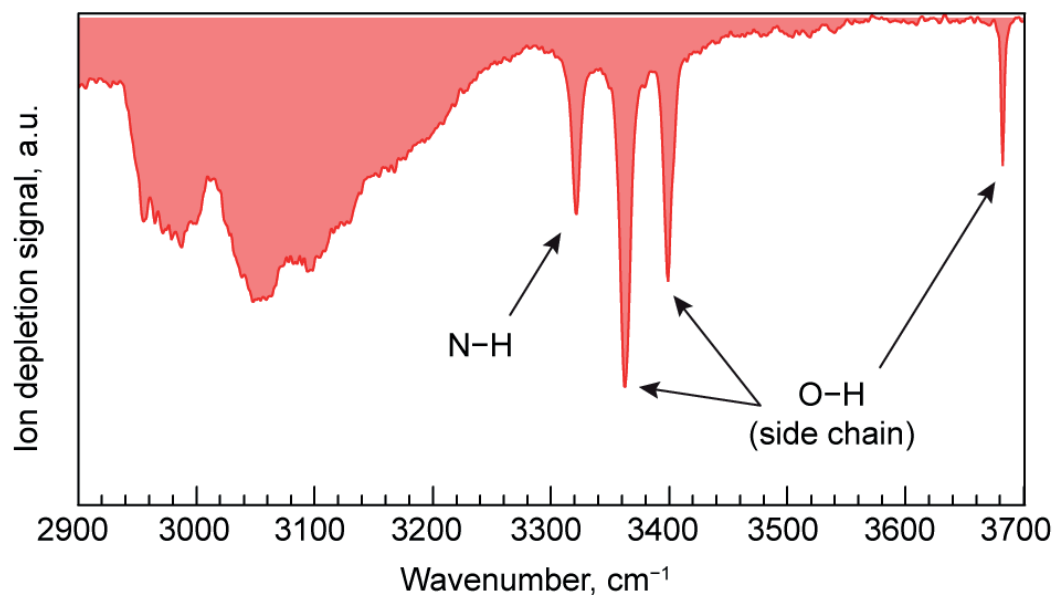
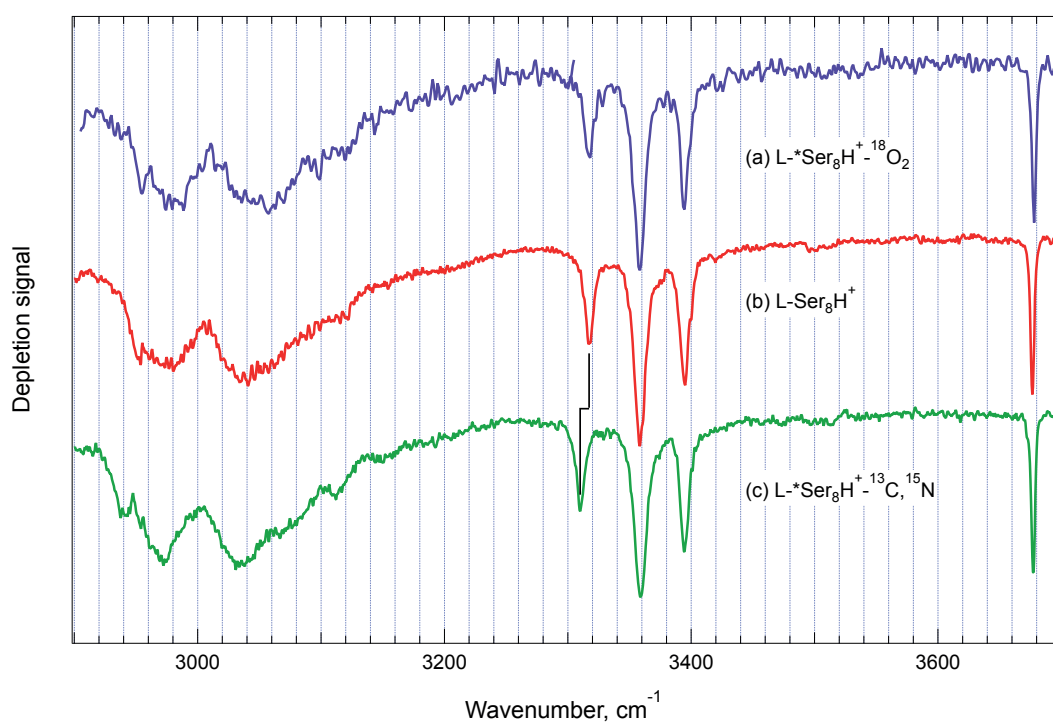


Figure 3.3. Infrared spectrum of the He-tagged  $\text{Ser}_8\text{H}^+$ .



*Figure 3.4. Cold ion infrared spectra of the serine octamers with various isotopic substitutions, (a) (L-Ser- $^{18}\text{O}_2$ ) $_8\text{H}^+$ , (b) (L-Ser) $_8\text{H}^+$  and (c) (L-Ser- $^{13}\text{C}_3, ^{15}\text{N}_1$ ) $_8\text{H}^+$  in the 2900–3700  $\text{cm}^{-1}$  region.*

### 3.4. Cysteine substitution

To gain further insight into the structure of the serine octamer, we electrosprayed 50:50 mixtures of serine and cysteine. As shown in Figure 3.5, the IR spectra of the  $\text{Ser}_7\text{Cys}_1\text{H}^+$  and  $\text{Ser}_6\text{Cys}_2\text{H}^+$  species resemble that of  $\text{Ser}_8\text{H}^+$ , but with a few small differences. Upon the first substitution, the bands at 3320 and 3677  $\text{cm}^{-1}$  decrease in intensity and a new band appears at 3258  $\text{cm}^{-1}$ , while other parts of the spectrum remain the same. The second substitution leads to similar changes, but now the two bands at 3317 and 3677  $\text{cm}^{-1}$  disappear completely and the band at 3258  $\text{cm}^{-1}$  grows by a factor of two in intensity. The disappearance of the free OH band at 3677  $\text{cm}^{-1}$  upon these two substitutions suggests that the two serines with a free OH side-chain are substituted by cysteines.

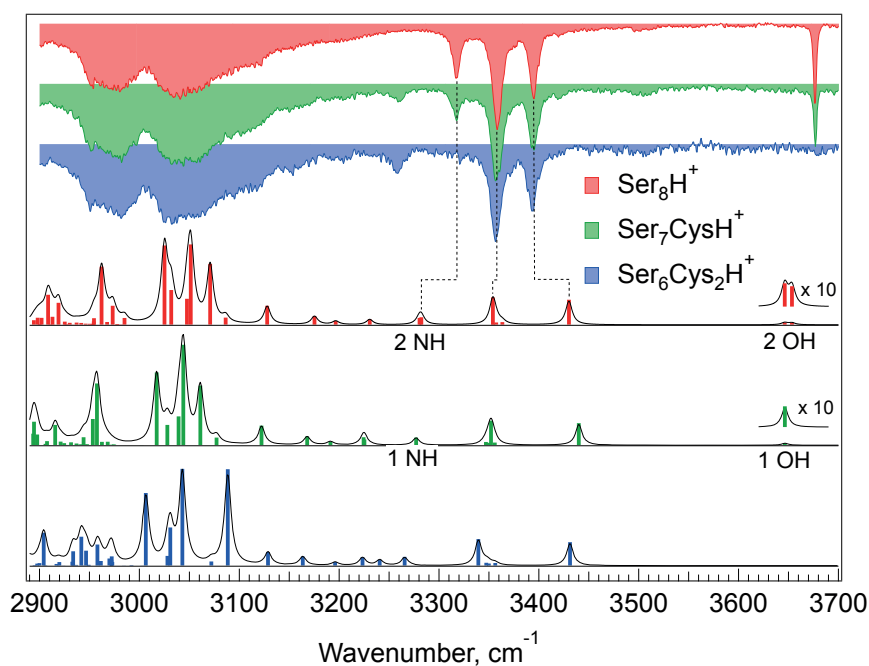


Figure 3.5. Experimental and theoretical IR spectra of the protonated serine octamer with cysteine substitutions. Red, green, and blue spectra represent the protonated serine octamer with no, one, and two cysteine substitutions, respectively.

Moreover, the spectra of  $\text{Ser}_7\text{Cys}_1\text{H}^+$  and  $\text{Ser}_8\text{H}^+$  are practically identical in the lower frequency range (Figure 3.6 (b,c)), which implies that the internal hydrogen-bonding pattern of the octamer is not affected by the cysteine substitution. In analogy with cysteine substitution, the high degree of similarity between  $\text{Ser}_7\text{Ala}_1\text{H}^+$  and  $\text{Ser}_8\text{H}^+$  (Figure 3.6 (a,c)) shows that the hydrogen bonding pattern in the cluster remains intact upon alanine substitution as well.



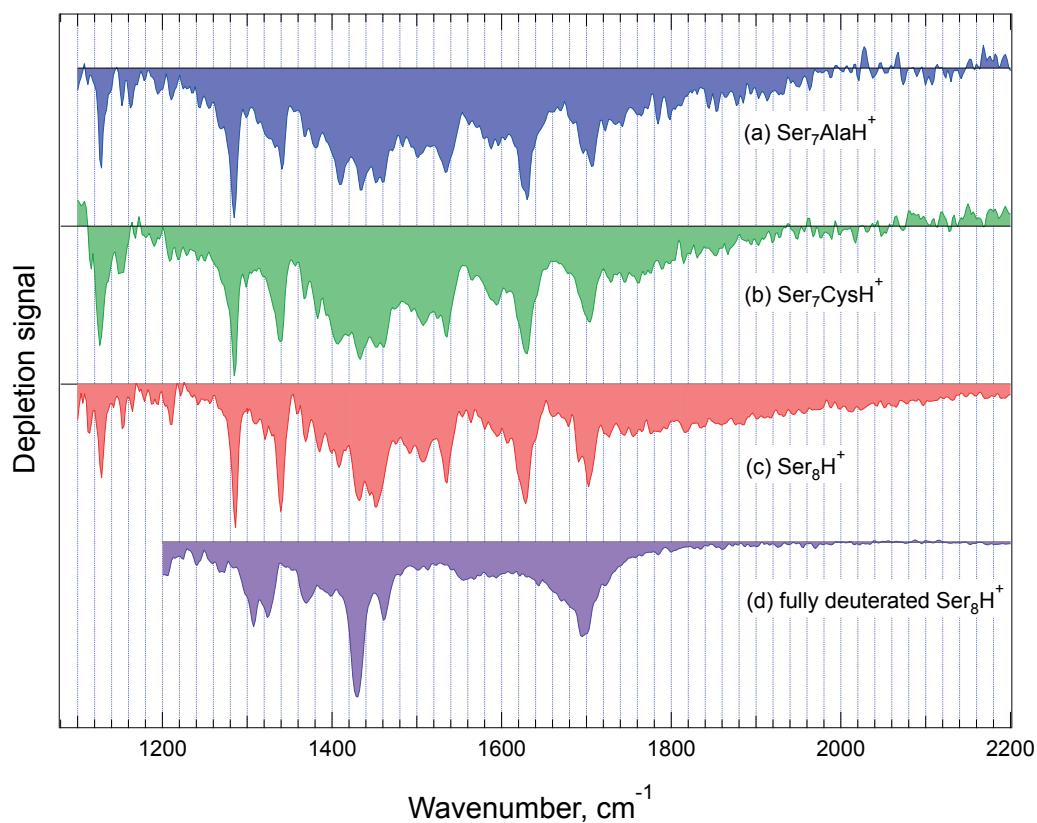


Figure 3.6. Infrared spectra of the a) alanine and b) cysteine substituted serine octamer; c) normal and d) fully deuterated octamer.

Marta Perez from the Laboratory of Computational Chemistry and Biochemistry conducted quantum mechanical computations and successfully identified the structure of the protonated serine octamer. All the theoretical results presented in this chapter are the result of collaboration with her.

### 3.5. Quantum mechanical conformational search

To determine the structure of the cluster on the basis of the IR spectrum of Figure 3.3, we performed an extensive exploration of the conformational space. Rather than making assumptions about the level of symmetry or the protonation sites of the  $\text{Ser}_8\text{H}^+$  cluster [24], we use simulated-annealing *ab initio* molecular dynamics (SA-AIMD), which can deal with mobile protons, to determine the most stable location of the protons simultaneously with conformational exploration. It has been previously demonstrated that SA-AIMD is effective in exploring potential energy surfaces (PES) and finding low energy structures [28, 29]. While the starting structures for our SA-AIMD runs were both symmetric and non-symmetric clusters of  $\text{Ser}_8\text{H}^+$  (with both neutral and zwitterionic forms considered), intriguingly, the simulations consistently converge to non-symmetric  $\text{Ser}_8\text{H}^+$  structures.

The key aspects of the conformational search follow. For each initial structure, simulated annealing *ab initio* molecular dynamics (SA-AIMD) runs were performed with the Terachem [30-32] program using the functional B3LYP [33], and a 6-31G or 6-31G(d,p) basis set [34]. During the SA-AIMD runs, the conformers were heated to high temperatures to accelerate phase-space sampling and then slowly cooled to 6K. For a wider sampling, different maximal heating temperatures (between 700K and 900K) and different cooling rates were applied. During the simulations, several proton jumps and conformational rearrangements occurred. The total simulation time was on average 50 ps/run, from which 50000

geometries were extracted all throughout the annealing run. A total of 150 unique conformational families were obtained from these SA-AIMD runs, including the final cooling products and different candidate structures from fast quenches at finite temperature.

The relative energies at the B3LYP/6-31G(d,p) level of theory and the collision cross-section (CCS) for candidate structures are summarized in Figure 3.7. The zwitterionic and compact structure proposed by the previous work [22] is found to be  $>25$  kcal/mol higher in energy than our most stable structure (A). The lowest energy structure obtained from the exhaustive force-field screening (FF) followed by DFT optimizations lies  $\sim 8$  kcal mol $^{-1}$  above the structure (A). The low-energy region of the plot is populated solely by zwitterionic, non-symmetric complexes, and we observe that imposing symmetry or constraining to canonical (non-zwitterionic) forms of serine yield higher energy conformers.

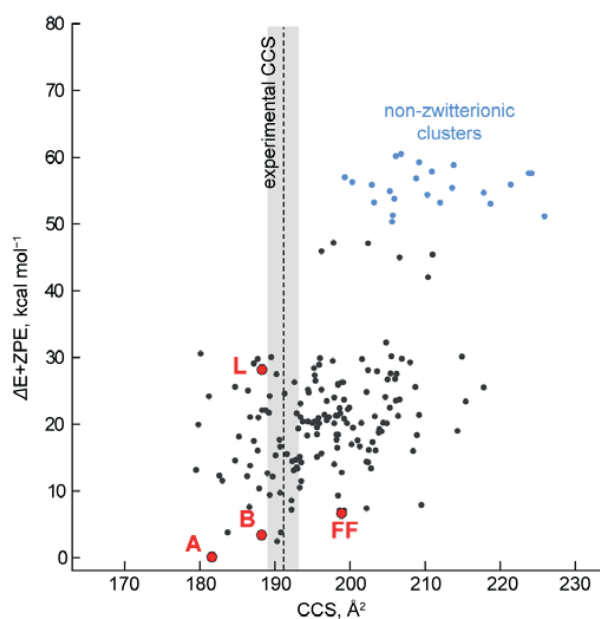


*Figure 3.7. Energy level and collision cross-section (CCS) diagram of candidate structures for the protonated serine octamer. The x-axis represents the CCS value calculated with the trajectory method. The y-axis represents the relative energies at the B3LYP//6-31G(d,p) level of theory. The most stable structure found by force field based sampling (FF), the zwitterionic flattened cube structure based on the previous literature (L) [22], the lowest-energy structure overall (A), and the structural candidate (B) are labeled in red. The dotted line and shaded region represent the measured CCS and the estimated error by our collaborators in FHI Berlin.*

The lowest-energy structure A (Figure 3.8) is stabilized by multiple short, strong hydrogen bonds in which carboxylate groups strongly interact with neighboring  $-\text{CH}_2\text{OH}$  or  $-\text{NH}_3^+$  groups. It has three protons which are shared between adjacent functional groups. Two of them are in  $-\text{NH}_3^+$  groups, each of which is shared with an adjacent carboxylate group ( $\text{COO}^- \cdots \text{H}^+ \cdots \text{NH}_2$ ). The extra proton on the cluster is also shared between two carboxylate groups ( $\text{COO}^- \cdots \text{H}^+ \cdots \text{OOC}^-$ ) with O–H distances of 1.1 Å and 1.4 Å. These shared protons are highlighted as spheres in Figure 3.8.

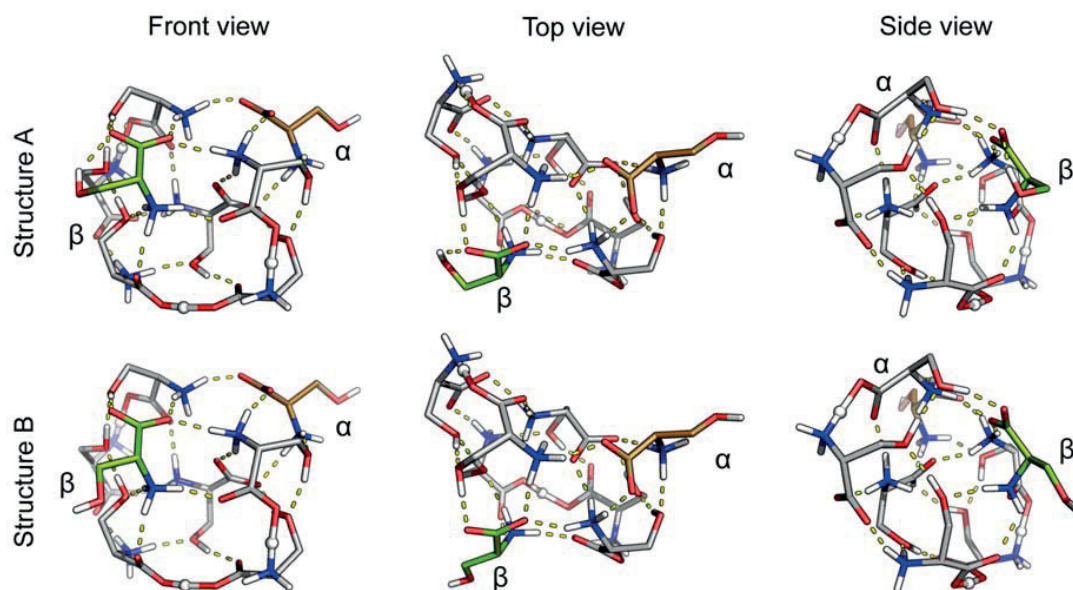


Figure 3.8. Different views of two structures of the protonated serine octamer (structures A and B in Figure 3.7). Non-polar hydrogens are omitted for clarity. The white spheres are a shared proton between two carboxylate groups and other two shared protons at  $\text{COO}^- \cdots \text{H}^+ \cdots \text{NH}_2$ .

The structure A contains six serines with their side chains tightly incorporated into the hydrogen bonding network and two serines that have their side chains either free (serine  $\alpha$ ) or loosely hydrogen-bonded to the core (serine  $\beta$ ). The second lowest energy structure in Figure 3.7 is similar to the structure A, and its serine  $\beta$  has a side chain forming a loose hydrogen bond with a different carboxylate. These lowest-energy structures of type A can easily adopt structure B (Figure 3.8), in which the hydrogen bond of the hydroxy group in serine  $\beta$  is broken. While the structures A and B differ in energy by  $3.3 \text{ kcal mol}^{-1}$  at 0 K, their free energy difference at 300 K decreases to  $1.6 \text{ kcal mol}^{-1}$  using harmonic vibrational corrections. In the

AIMD simulations at 300 K, which inherently include anharmonic effects, structure B is more abundant than structure A: a 10 ps trajectory (B3LYP/6-31G(d,p)) shows that the probability of the occurrence of a  $-\text{CH}_2\text{OH}\cdots\text{O}$  hydrogen bond in serine  $\beta$  is 24% and further decreases to less than 10% at 600 K (see Figure 3.9). Structure B has a CCS value of  $189 \pm 1 \text{ \AA}^2$ , which is in good agreement with the experimental values either in the present work ( $191 \pm 2 \text{ \AA}^2$ ) or in the previous literature (187 and  $191 \text{ \AA}^2$ ) [7, 9].

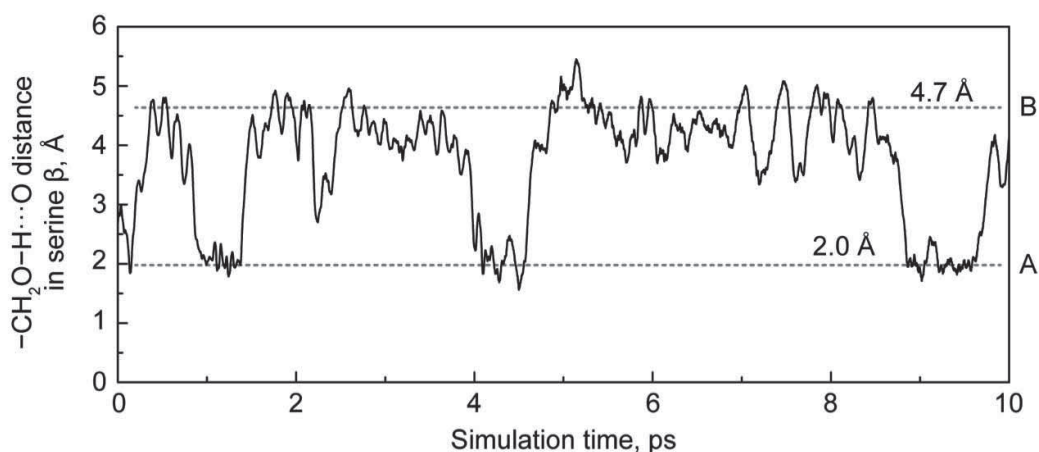


Figure 3.9. The  $-\text{CH}_2\text{OH}\cdots\text{O}$  distance in serine  $\beta$  during the *ab initio* MD simulation with B3LYP/6-31G(d,p) level of theory at 300 K. The  $-\text{CH}_2\text{OH}\cdots\text{O}$  distances in the structures A and B (2.0 and 4.7  $\text{\AA}$  respectively) are shown as dashed lines.

Using an analogous procedure to determine the lowest-energy structure of the nonamer shows that the binding energy per monomer in  $\text{Ser}_9\text{H}^+$  is roughly  $5.3 \text{ kcal mol}^{-1}$  less than that in  $\text{Ser}_8\text{H}^+$ , which rationalizes the magic number of eight (Figure 3.10). Moreover, the predicted structure

of  $\text{Ser}_9\text{H}^+$  suggests that the compact octamer has a complete shell, and an extra serine monomer initiates a new shell that surrounds  $\text{Ser}_8\text{H}^+$ .

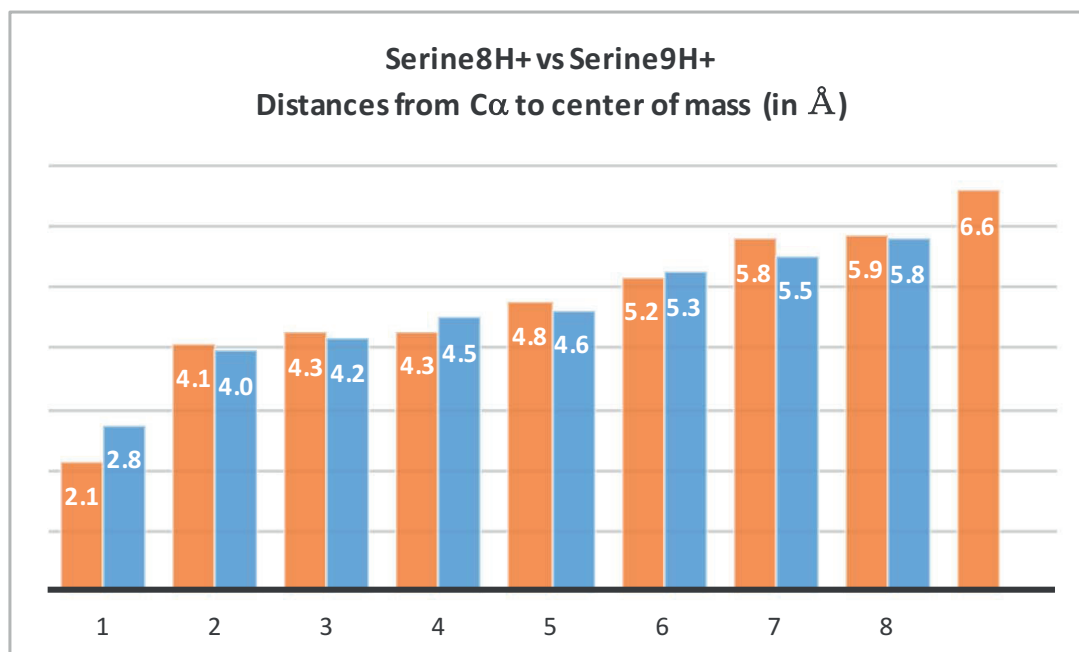


Figure 3.10.  $\text{Ser}_8\text{H}^+$  vs  $\text{Ser}_9\text{H}^+$ . Distances from  $\text{C}\alpha$  of each serine to the center of mass of the cluster presented in blue for  $\text{Ser}_8\text{H}^+$  and in orange for  $\text{Ser}_9\text{H}^+$ .  $E(\text{Ser}_8\text{H}^+ \text{ binding per monomer}) = -5.3 \text{ kcal mol}^{-1}$  lower.

### 3.6. Theoretical predictions vs. experiment

Figure 3.5 compares the measured IR spectrum (red trace) with the calculated spectrum of structure B (red sticks). In the latter, we find two stretch modes of the free side chain OH groups ( $\alpha$  and  $\beta$  in Figure 3.8) at  $3653$  and  $3646 \text{ cm}^{-1}$ , which fit well to the experimental band position of  $3677 \text{ cm}^{-1}$ . The computed spectrum of structure A (blue sticks in Figure 3.11) contains only one stretch mode of the free side chain OH group ( $\alpha$  in Figure 3.8) that appears at  $3642 \text{ cm}^{-1}$  and a hydrogen bonded OH side-chain mode

of  $\beta$  serine at  $3506\text{ cm}^{-1}$ . This characteristic frequency shift allows us to distinguish the structure B from structure A and conclude that structure A is not populated in our experimental conditions.

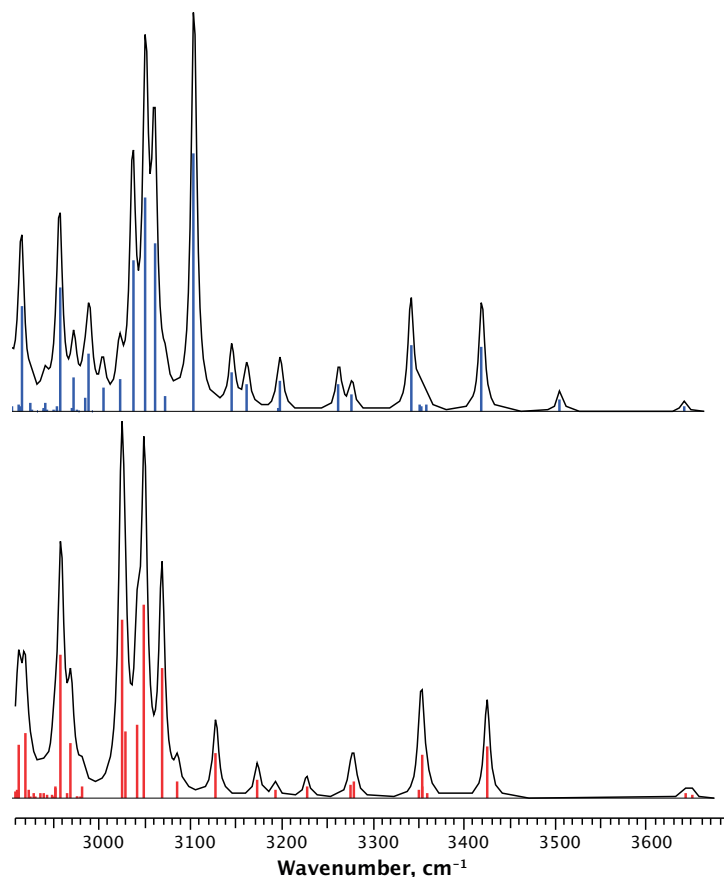


Figure 3.11. Theoretical spectra of structure A (blue sticks) and structure B (red sticks). Because the absorption line at  $\sim 3500\text{ cm}^{-1}$  of the structure A is absent in the experimental spectrum (Figure 3.3), we conclude that the conformer A is not populated in the experiment.

In structure B, stretch modes of hydrogen-bonded OH side-chains appear at  $3430$  and  $3353\text{ cm}^{-1}$ , in good agreement with the measured bands at  $3395$  and  $3358\text{ cm}^{-1}$ , which were assigned to side chain OH stretch modes



by isotope labeling (Figures Figure 3.3 and Figure 3.4). Two vibrational bands from the  $\text{NH}_2$  asymmetric stretch of  $-\text{NH}_3^+$  groups that have one H weakly hydrogen-bonded appear at  $3280\text{ cm}^{-1}$  (corresponding to the measured band at  $3317\text{ cm}^{-1}$ ). In the region between  $2900$  and  $3200\text{ cm}^{-1}$ , a large number of ammonium stretch modes gives rise to unresolved overlapping bands in both the experiment and the calculated spectra. The good agreement between the calculations and the well-resolved experimental bands gives strong support for an assignment to conformer B.

Calculations of  $\text{Ser}_7\text{Cys}_1\text{H}^+$  and  $\text{Ser}_6\text{Cys}_2\text{H}^+$  have shown that cysteine substitution represents minimal perturbation to the serine octamer cluster, and again the calculated and experimental spectra are in good agreement (see green and blue stick spectra in Figure 3.5). The two cysteines replace the two serines in which the OH side chain is not H-bonded (i.e. serine  $\alpha$  and  $\beta$  in Figure 3.8). This replacement preserves the strong H-bond character of the cluster, maintaining its maximum stability. Cysteine replacement in any other position results in a less stable structure and yields an IR spectrum that does not match with the experiment.  $\text{Ser}_7\text{CysH}^+$  lacks one free OH from  $\text{Ser}_8\text{H}^+$ , which appears at  $3653\text{ cm}^{-1}$ , because it is replaced by SH that shifts this line down to  $2562\text{ cm}^{-1}$ . Likewise, the intensity of the band at  $3280\text{ cm}^{-1}$  is decreased for  $\text{Ser}_7\text{Cys}_1\text{H}^+$ , because the replacement of serine by cysteine red-shifts the NH stretching vibration by  $50\text{ cm}^{-1}$ . Thus, the calculated spectrum of  $\text{Ser}_7\text{Cys}_1\text{H}^+$  exhibits one peak at  $\sim 3280\text{ cm}^{-1}$  and two peaks at  $\sim 3230\text{ cm}^{-1}$ , justifying the decrease in intensity of the NH band

experimentally observed at  $3317\text{ cm}^{-1}$  and the increase in intensity of the measured band at  $3258\text{ cm}^{-1}$ . In  $\text{Ser}_6\text{Cys}_2\text{H}^+$ , both serine  $\alpha$  and  $\beta$  are replaced by cysteine, causing the second OH band at  $3646\text{ cm}^{-1}$  to disappear. Moreover, the second NH mode that shows up at  $3280\text{ cm}^{-1}$  in  $\text{Ser}_8\text{H}^+$  and in  $\text{Ser}_7\text{Cys}_1\text{H}^+$  is red-shifted by  $11\text{ cm}^{-1}$  in  $\text{Ser}_6\text{Cys}_2\text{H}^+$ , supporting the total disappearance of the band at  $3317\text{ cm}^{-1}$  in the experimental spectrum.

### 3.7. Cryogenic ion spectroscopy in the fingerprint region

To further confirm our structural assignment, we compared the IR spectrum of the serine octamer in the wavenumber range of  $1100\text{--}2200\text{ cm}^{-1}$  with theoretical predictions. For amino acids, the C=O stretch bands of a neutral carboxylic acid should appear in the range  $1700\text{--}1800\text{ cm}^{-1}$  [35, 36]. Carboxylate groups, on the other hand, give symmetric and antisymmetric stretch bands in the  $1300\text{--}1450\text{ cm}^{-1}$  and  $1600\text{--}1650\text{ cm}^{-1}$  region, respectively [37, 38].

In the experimental spectra (Figure 3.6 (c) and Figure 3.12 (a)), the IR bands at  $\sim 1620\text{ cm}^{-1}$  can be assigned to carboxylate groups and the NH bending mode of  $-\text{NH}_3^+$ . The band at  $\sim 1420\text{ cm}^{-1}$  confirms the presence of carboxylates. The observed IR band at  $\sim 1695\text{ cm}^{-1}$  indicates the presence of a strongly hydrogen-bonded carbonyl (C=O) group of a carboxylic acid. Additional experiments further support these assignments, which show that the intense IR bands at  $\sim 1695$  and  $1410\text{--}1430\text{ cm}^{-1}$  do not shift to lower wavenumber upon H/D exchange (see Figure 3.6 (c,d)). Some broad

features at 1560–1620  $\text{cm}^{-1}$  also remain after H/D exchange. These results suggest the presence of both carboxylic acids and carboxylates.

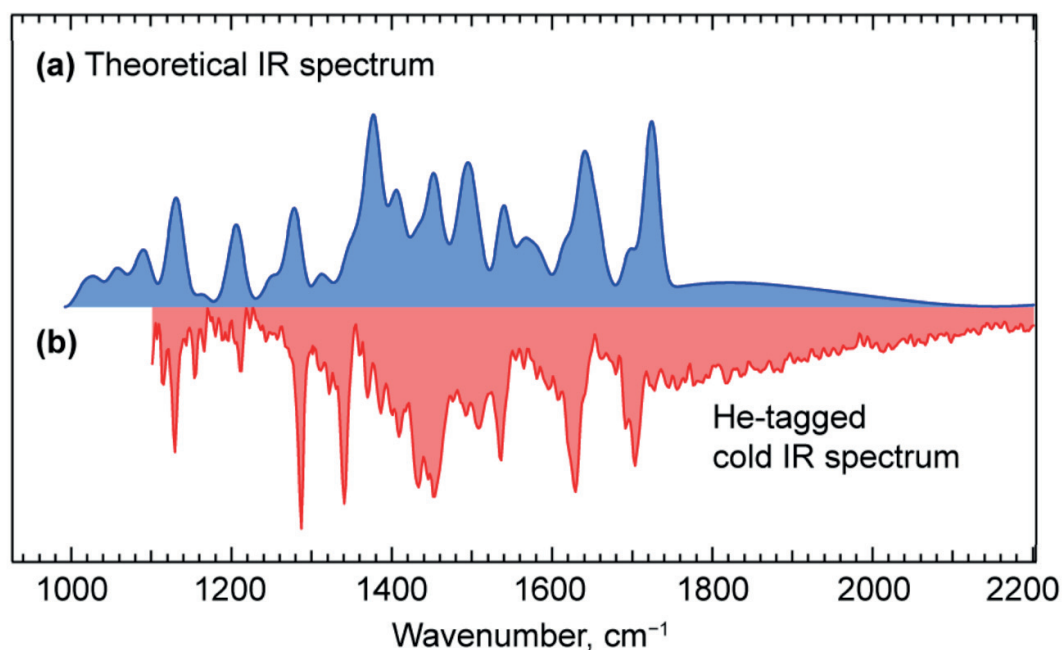


Figure 3.12. (a) Theoretical IR spectrum of structure B of the  $\text{Ser}_8\text{H}^+$  and (b) experimental cold IR spectrum of the He-tagged  $\text{Ser}_8\text{H}^+$ .

The calculated IR spectrum for structure B in this wavenumber region is shown in Figure 3.12 (a). Each line in the theoretical vibrational spectrum is represented by a Gaussian with full width at half maximum (FWHM) of 20  $\text{cm}^{-1}$  except for bands  $>1750 \text{ cm}^{-1}$  where vibrational modes involving motion of the shared protons appear. Proton motions between two carboxylates and/or at  $\text{CO}\cdots\text{H}-\text{N}$  give rise to bands at 2346, 1896, and 1780  $\text{cm}^{-1}$ . Typically, vibrational modes of such shared protons are highly anharmonic and give rise to broad spectral features [39, 40]. For this reason, we set the FWHM of the Gaussian of the vibrations in the region  $>1750$

$\text{cm}^{-1}$  to  $200 \text{ cm}^{-1}$ . The experimentally observed broad IR features at  $>1750 \text{ cm}^{-1}$  fits well to theory, which further confirms the presence of the proton-sharing carboxylates. Complete H/D exchange shifts all these broad features in both the cryogenic IR spectrum (Figure 3.6 (d)), which gives additional support for the assignment as shared proton modes.

Theory predicts IR bands at  $\sim 1695 \text{ cm}^{-1}$  corresponding to antisymmetric stretch modes of three carboxylates with shared protons ( $\text{COO}^- \cdots \text{H}^+ \cdots \text{OOC}$  and  $\text{COO}^- \cdots \text{H}^+ \cdots \text{NH}_2$ ). The strongly shared protons increase acidic character of carboxylates, which makes antisymmetric stretches of carboxylate similar to the carbonyl stretches of strongly H-bonded carboxylic acids. Therefore, they appear at  $\sim 1695 \text{ cm}^{-1}$ , which is higher than typically found for the antisymmetric stretch of carboxylates. Antisymmetric and symmetric stretch modes of all other  $\text{COO}^-$  groups are calculated to appear at  $\sim 1620 \text{ cm}^{-1}$  and  $\sim 1440 \text{ cm}^{-1}$ , which are once again in agreement with the experimental observations. All these results in the  $1000\text{--}2200 \text{ cm}^{-1}$  region corroborate our proposed structure for  $\text{Ser}_8\text{H}^+$ .

### 3.8. Chiral substitution

We also measured spectra of serine octamers with mixed chirality in the  $2900\text{--}3700 \text{ cm}^{-1}$  region (Figure 3.13). The theoretical vibrational spectra of the lowest energy structures match well the experimental IR spectra. The structure of  $(\text{L-Ser}_7+\text{D-Ser}_1)\text{H}^+$  consists in the replacement of L-Ser  $\alpha$  with D-Ser. In  $(\text{L-Ser}_6+\text{D-Ser}_2)\text{H}^+$  both  $\alpha$  and  $\beta$  are substituted.  $(\text{L-Ser}_7+\text{D-Ser}_1)\text{H}^+$  is  $1 \text{ kcal mol}^{-1}$  less stable than cluster A at 300K and  $(\text{L-Ser}_6+\text{D-Ser}_2)\text{H}^+$  is  $2 \text{ kcal mol}^{-1}$  less stable than cluster A at 300K.

$\text{Ser}_2)\text{H}^+$  is already 4 kcal mol<sup>-1</sup> less stable. Any other substitution with more than two D-serines is not tolerated, because all the other six L-Ser side chain OHs establish strong H-bond interactions in the core of the cluster and the replacement of a third L-Ser totally disrupts the H-bond network of the cluster.

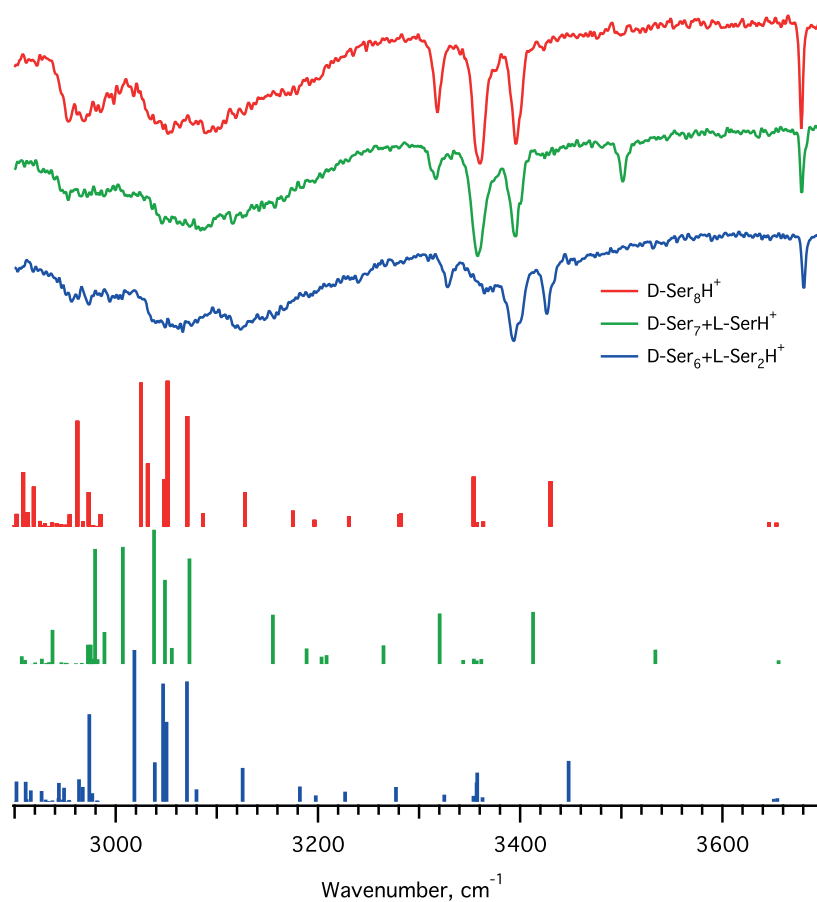


Figure 3.13. Chiral replacement in the serine octamer. L-Ser was mixed with isotopically labeled D-Ser for isolating  $(\text{L-Ser}_7^+\text{D-Ser}_1)\text{H}^+$  and  $(\text{L-Ser}_6^+\text{D-Ser}_2)\text{H}^+$  species.

The preference for homochirality is the consequence of the three-point interactions between the serine units, as previously suggested [9, 22]. In such

three-point interactions, three functional groups of a serine (a carboxylate, an ammonium, and a sidechain hydroxyl) form intermolecular hydrogen bonds with adjacent serines. Due to the chirality of serine, such three-point interactions will have a certain directionality, and the entire network of three-point interactions will depend on the chiral nature of its components. However, while the protonated serine octamer is strongly homochiral, it is not absolutely homochiral as shown in Figure 3.1 (b), and the structure we propose nicely explains this. In conformer B, two serine units ( $\alpha$  and  $\beta$ ) have free side chains, and thus are only involved in intrinsically non-chiral, two-point interactions, while other six are forming three-point interactions. They are thus more loosely bound in the cluster than the other six and more easily able to be substituted by other amino acids (including serine of opposite chirality) without inducing a major change of the octamer structure.

### 3.9. Additional amino acid substitutions

The serine octamer accepts a variety of amino acids in different proportions [15]. As seen before, replacing serine amino acids with cysteine leads to a selective shift of bands. While cysteine is structurally very similar to serine, it is intriguing to test whether other amino acids will lead to analogous peculiar changes in the infrared spectrum.

Vibrational spectra of mixed serine/glycine clusters exhibit similar features with the pure serine octamer (Figure 3.14). The sharp bands at 3358 and 3395  $\text{cm}^{-1}$  appear unchanged upon one substitution, while the

intensity of the bands at 3317 and 3677  $\text{cm}^{-1}$  diminishes comparably as in the case of cysteine substitution. Upon a double substitution with glycine, the spectrum of the cluster varies significantly from the green and blue spectra (Figure 3.14). The band at 3358  $\text{cm}^{-1}$  becomes less intense and a new band appears at 3425  $\text{cm}^{-1}$ .

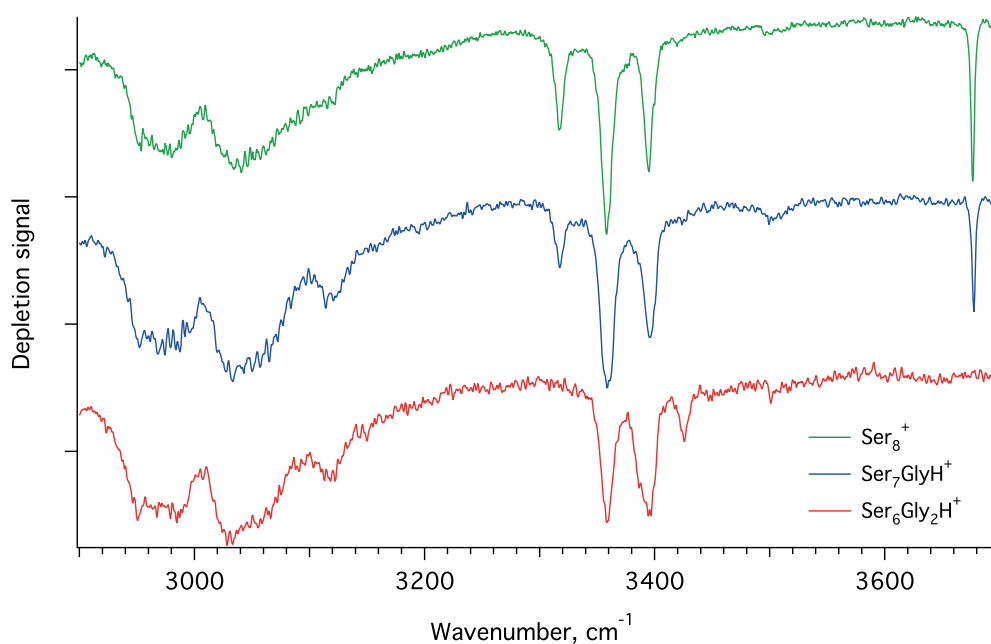


Figure 3.14. Sequential substitution of serine with glycine.

The power dependence of the 3677  $\text{cm}^{-1}$  band provides us with a better picture of the changes that take place in the spectrum (Figure 3.15). At high laser power, the transition at 3677  $\text{cm}^{-1}$  tends to saturate. Variable  $a1$  in the fitting curve is proportional to absorption cross section, thus the found decrease of  $a1$  by a factor of  $2.01 \pm 0.15$  after one glycine substitution hints that the absorption cross section of the two free OH oscillators is equal. The variable  $c$  in the fit is the theoretical depletion of the fully

saturated transition and corresponds to the relative abundance of the probed conformer in the trap. The  $c$  parameters do not reach -1, because the IR laser beam does not fully overlap with the disperse ion cloud in the octupole trap.

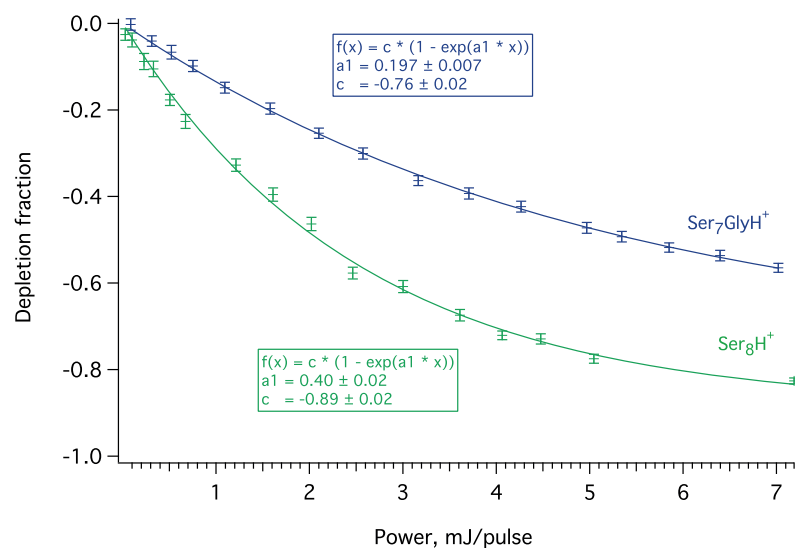


Figure 3.15. The intensity of the free OH band ( $3677 \text{ cm}^{-1}$ ) decreases upon the first substitution with glycine.

The band at  $3358 \text{ cm}^{-1}$  saturates at lower laser power (as seen in Figure 3.16), which indicates a high absorption cross section of this hydrogen bonded OH. Moreover, the transition at  $3358 \text{ cm}^{-1}$  of Ser<sub>6</sub>Gly<sub>2</sub>H<sup>+</sup> saturates at  $\sim 67\%$  – significantly less than for the other two clusters ( $\sim 90\%$ ) – suggesting that a new conformer forms and has substantial abundance.



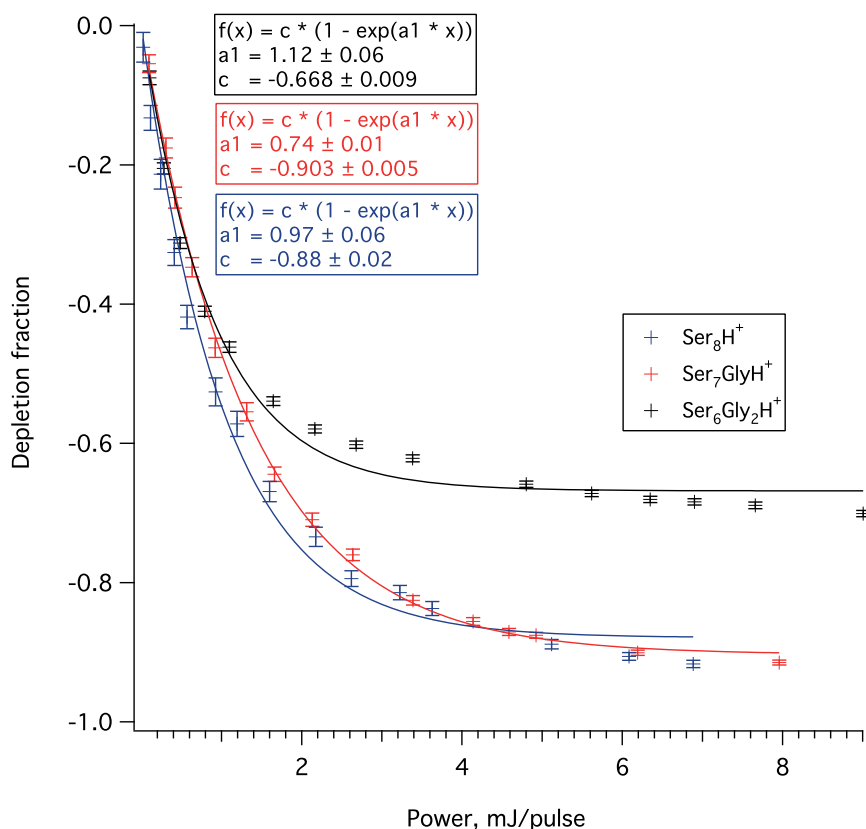


Figure 3.16. Power dependence of the hydrogen bonded OH band ( $3358 \text{ cm}^{-1}$ ) in substituted serine clusters with glycine.

Nanita *et al.* found that threonine replaces quite efficiently serine subunits in Ser<sub>8</sub>H<sup>+</sup> [15]. We also observe larger distribution of threonine/serine mixed clusters than for cysteine and glycine substituted clusters (Figure 3.17). The infrared spectrum of Ser<sub>4</sub>Thr<sub>4</sub>H<sup>+</sup> exhibits a similar pattern of bands that appear broadened and blue-shifted (Figure 3.18). A tentative explanation is the moderate expansion of the cluster due to the methyl side chain of threonine keeping the same hydrogen bonding pattern. The same effect can explain the observed broader distribution of

the serine/threonine mixed clusters. Further studies are needed to give a more detailed picture of this phenomenon.

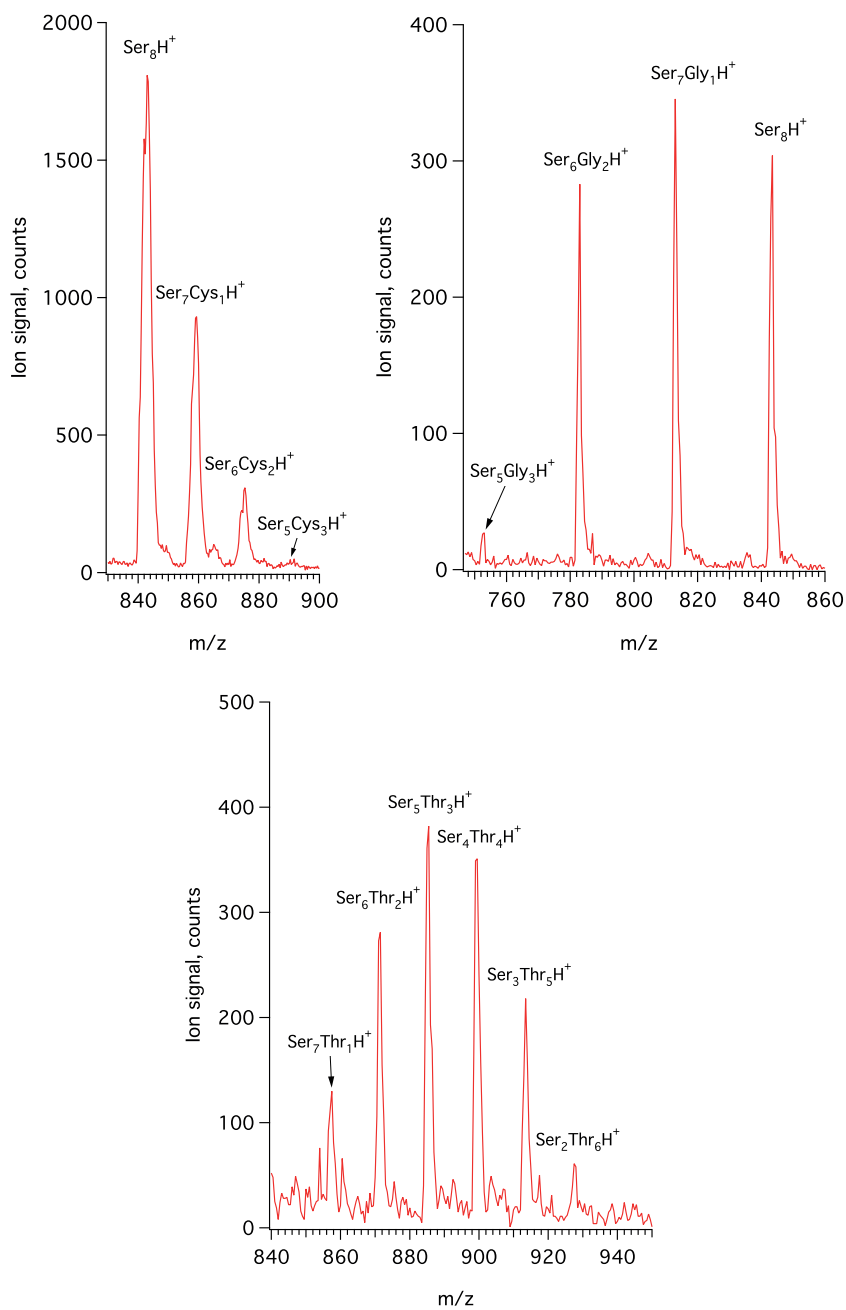


Figure 3.17. Intensity distributions for cysteine, glycine and threonine substituted serine clusters.

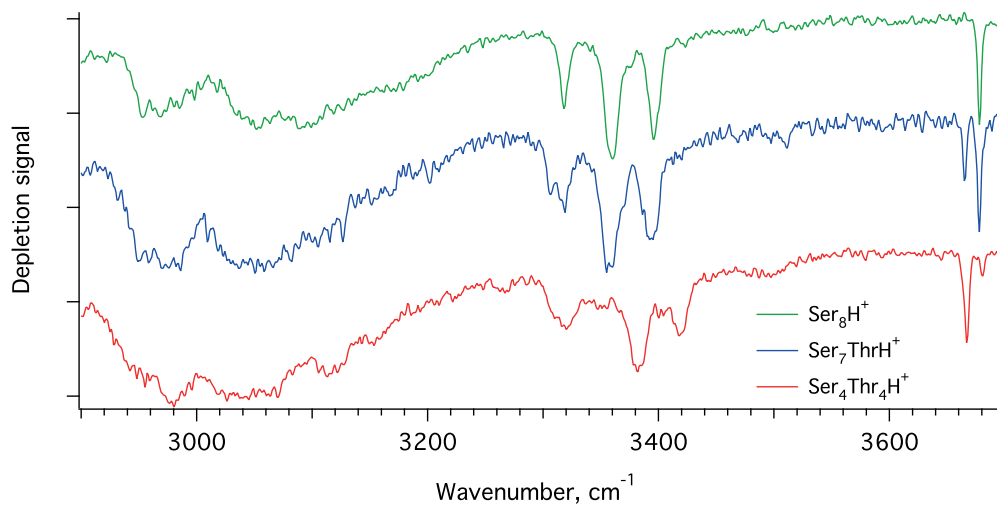


Figure 3.18. Substitution of serine with threonine.

### 3.10. Influence of He tags on the spectrum of Ser<sub>8</sub>H<sup>+</sup>

All the IR spectra shown thus far were acquired on singly tagged ions. In this section we turn our attention to ionic clusters with multiple He tags. A rather high efficiency of He tagging in our octopole ion trap (Figure 3.19) allows us to acquire IR spectra of the doubly and triply tagged protonated serine octamer as well (Figure 3.20).

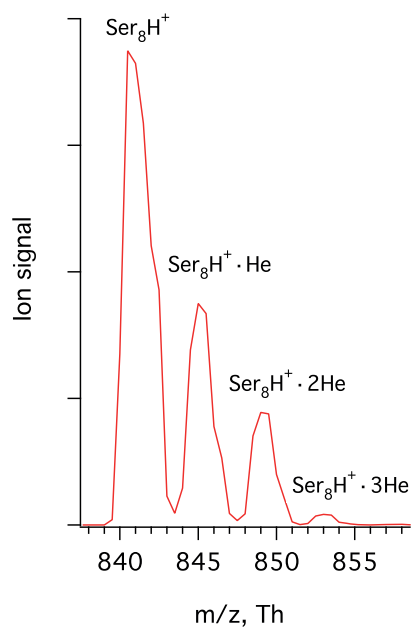


Figure 3.19. Mass spectrum representing the He tagging efficiency.

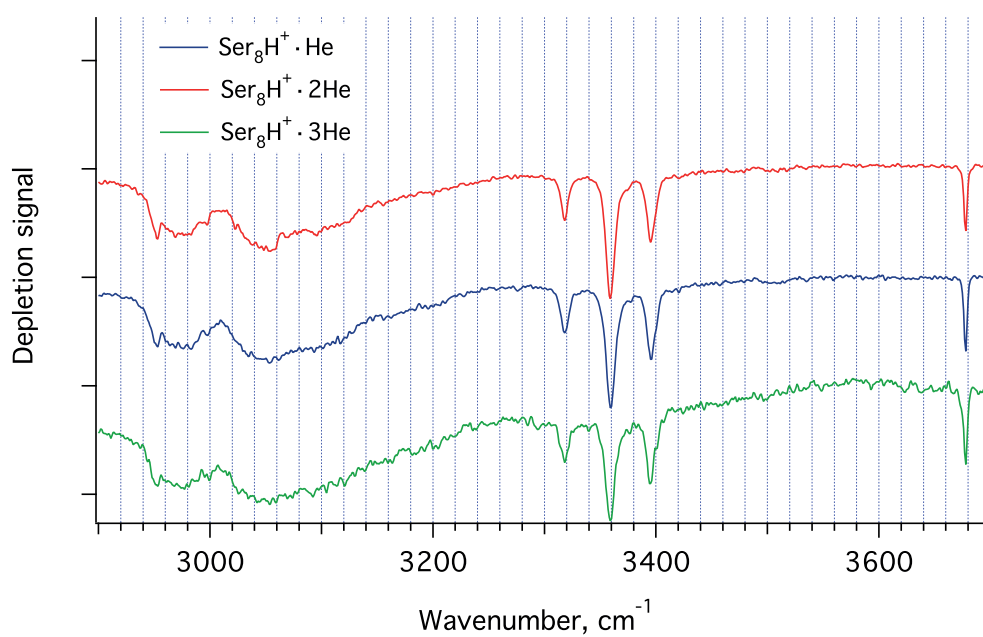


Figure 3.20. IR spectra of ion clusters with different number of bound He atoms.

The positions of sharp bands appear at nearly identical frequencies upon sequential increase of the number of tags. We infer from this observation that the He tags do not perturb significantly the IR spectrum of  $\text{Ser}_8\text{H}^+$ .

### 3.11. IR spectroscopy of protonated serine oligomers

Harsher transmission of ions in the high-pressure region leads to a large number of various size serine clusters. We assigned some of the peaks in Figure 3.21 to protonated or sodiated serine clusters. They can form because of the fragmentation of the serine octamer or from fragmentation of higher mass metaclusters [41].

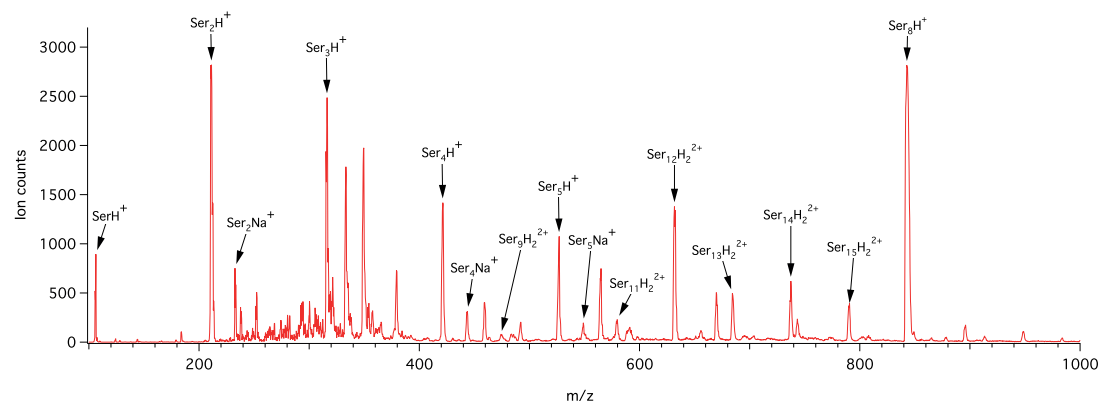


Figure 3.21. Mass spectrum of serine solution (5 mM) obtained in energizing conditions.

Previously it has been suggested that  $\text{Ser}_2\text{H}^+$  is the building unit of the serine octamer and that the structure of smaller size clusters might give a hint on the formation of the magic number  $\text{Ser}_8\text{H}^+$  [6]. We acquire the infrared multiple photon dissociation (IRMPD) mass spectrum of  $\text{Ser}_8\text{H}^+$ ,

shown in Figure 3.22. The smooth distribution of intensities of the  $\text{Ser}_3\text{H}^+$  fragments implies that there is no preference in losing more than one serine amino acid subunit at a time. As a result, we conclude that the two serine subunits in  $\text{Ser}_2\text{H}^+$  do not interact stronger than inside  $\text{Ser}_3\text{H}^+$ .

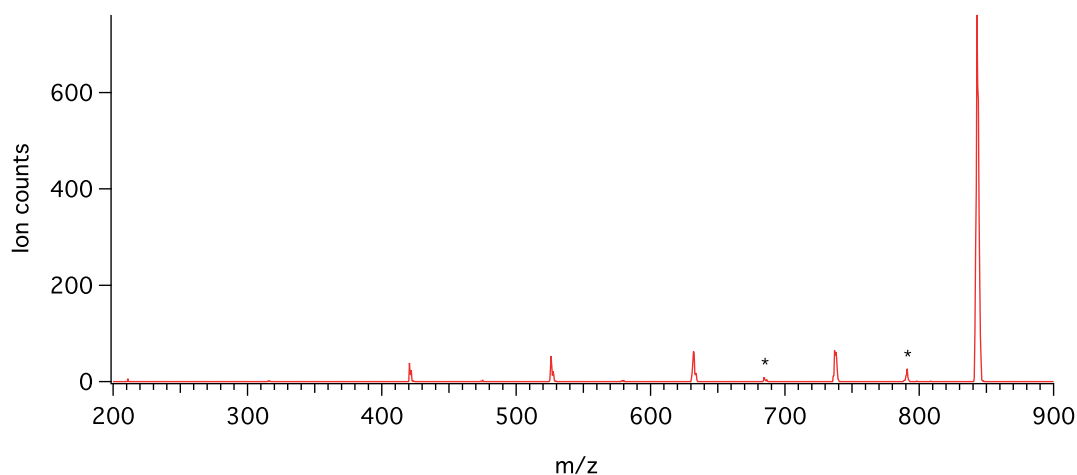


Figure 3.22. Fragmentation of mass selected  $m/z=841$  ions from intense  $10.6 \mu\text{m}$  ( $\text{CO}_2$  laser) radiation. The starred lines are fragments of  $\text{Ser}_{16}\text{H}_2^{2+}$ .

The high abundance of miscellaneous fragment ions in activating conditions allows registering IR spectra of the serine oligomers depicted in Figure 3.23. Comparing all the spectra, the sparsity of the IR spectrum of  $\text{Ser}_8\text{H}^+$  is rather striking. All the other clusters have numerous IR bands, the most prominent example is the  $\text{Ser}_4\text{H}^+$  spectrum. A plausible explanation is that the fragment clusters might adopt multiple conformations.

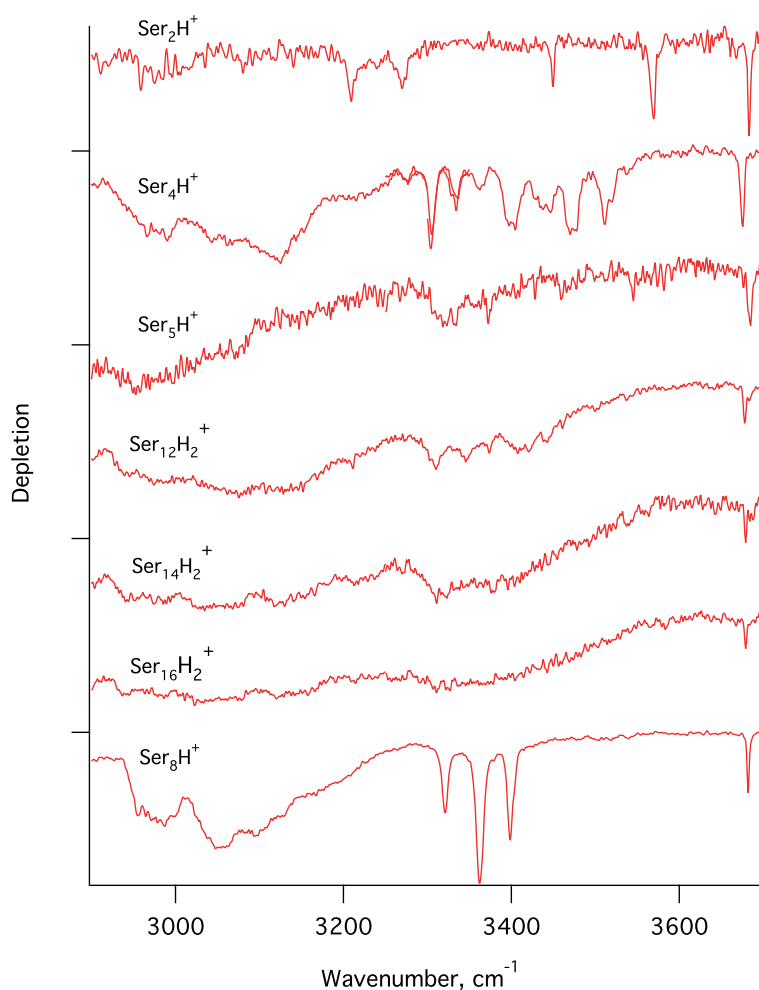


Figure 3.23. IR spectroscopy of various size protonated serine clusters.

A particular question about the structure of serine oligomers other than the octamer is whether their structure is zwitterionic or not. One can have an educated guess about this inspecting the spectra of oligomers in two characteristic regions: (1) the broad band between  $\sim 2900\text{-}3200\text{ cm}^{-1}$  is specific for hydrogen bonded  $\text{NH}_3^+$  group vibrations [42-46], and (2) the absence of a free carboxylic OH at  $3570\text{ cm}^{-1}$  means that the carboxylic acid group is deprotonated (in the case of a zwitterion) or it is hydrogen bonded. The spectrum of  $\text{Ser}_2\text{H}^+$  has a free carboxyl OH group at  $3570\text{ cm}^{-1}$  and the

intensity of the band around  $3000\text{ cm}^{-1}$  is rather low, that leads us to suppose that serine subunits in  $\text{Ser}_2\text{H}^+$  are not zwitterionic. This prediction is consistent with the quantum mechanical computations and IRMPD spectroscopy of the dimer in [25], which found the neutral form to be the most stable. The spectral resolution of cryogenic IR spectroscopy is higher than IRMPD and allows the unambiguous assignment of the computed structure named homo-N6 in [25] to the one present in our experimental conditions. However, the spectrum of  $\text{Ser}_4\text{H}^+$  displays a more intense band between  $3000\text{-}3200\text{ cm}^{-1}$ , and no absorption at the diagnostic  $3570\text{ cm}^{-1}$  frequency, hence we conclude that the protonated serine tetramer is likely zwitterionic. The same reasoning applies to all the other larger oligomers. This hypothesis might be tested with the application of  $^{18}\text{O}$ -labeling in the carboxylic group.

### 3.12. Summary

In this chapter we present the structure of the protonated serine octamer identified by a combination of experimental and high-level theoretical techniques: cryogenic infrared spectroscopy and simulated annealing *ab initio* molecular dynamics. The proposed structure B (Figure 3.8) fulfills the constraints derived from experiments: a) it is consistent with the measured IR spectrum and collisional cross section; b) it is of exceptional stability, implying a nearly perfect hydrogen bonding pattern; c) it has a strong preference for homochirality; d) it permits the facile substitution of up to two amino acids, either with serine of different chirality



or other amino acids. The calculated IR spectra are in excellent agreement with the measured spectra of Figures 3.5 and 3.12, as verified by isotopic substitution. The predicted CCS value ( $189 \pm 1 \text{ \AA}^2$ ) also agrees well with the experimental value. The preference for homochirality is a result of the strong hydrogen bonding between the three functional groups of the serine units. The strong hydrogen bonding network is disrupted when replacing another subunit than  $\alpha$  or  $\beta$  serines with a different amino acid. Threonine is exceptional, allowing a more efficient substitution of serine subunits due to its high degree of similarity to serine – the core structure of  $\text{Ser}_8\text{H}^+$  can be maintained, albeit expanded. Helium is found to be an innocent tag for  $\text{Ser}_8\text{H}^+$ , because the positions of sharp bands appeared at nearly identical frequencies in IR spectra of singly, doubly and triply tagged  $\text{Ser}_8\text{H}^+$  clusters.

A future direction for this project can be a deeper study of other types of amino acid substitutions in the serine cluster. IR spectroscopy of protonated serine oligomers combined with high-level theory might reveal the smallest size of the cluster, when the serine subunits transit from the neutral to zwitterionic form. The structure of the serine octamer can be used as a small and relatively complex system with strong hydrogen bonding for developing computational methods for biomolecular structure modeling *in silico*.

References:

1. Kroto, H.W., J.R. Heath, S.C. O'Brien, R.F. Curl and R.E. Smalley, *C<sub>60</sub>: Buckminsterfullerene*. Nature, 1985. **318**: p. 162.
2. Miehle, W., O. Kandler, T. Leisner and O. Echt, *Mass spectrometric evidence for icosahedral structure in large rare gas clusters: Ar, Kr, Xe*. Journal of Chemical Physics, 1989. **91**(10): p. 5940-5952.
3. Guo, B.C., S. Wei, J. Purnell, S. Buzza and A.W. Castleman, *Metallo-Carbohedrenes [ $M_8C_{12}^+$  ( $M = V, Zr, Hf, \text{ and } Ti$ )]: A Class of Stable Molecular Cluster Ions*. Science, 1992. **256**(5056): p. 515-516.
4. Nemes, P., G. Schlosser and K. Vekey, *Amino acid cluster formation studied by electrospray ionization mass spectrometry*. J. Mass Spectrom., 2005. **40**(1): p. 43-49.
5. Do, T.D., N.E.C. de Almeida, N.E. LaPointe, A. Chamas, S.C. Feinstein and M.T. Bowers, *Amino Acid Metaclusters: Implications of Growth Trends on Peptide Self-Assembly and Structure*. Anal. Chem., 2016. **88**(1): p. 868-876.
6. Cooks, R.G., D. Zhang, K.J. Koch, F.C. Gozzo and M.N. Eberlin, *Chiroselective Self-Directed Octamerization of Serine: Implications for Homochirogenesis*. Anal. Chem., 2001. **73**(15): p. 3646-3655.
7. Counterman, A.E. and D.E. Clemmer, *Magic Number Clusters of Serine in the Gas Phase*. Journal of Physical Chemistry B, 2001. **105**(34): p. 8092-8096.

8. Koch, K.J., F.C. Gozzo, D.X. Zhang, M.N. Eberlin and R.G. Cooks, *Serine octamer metaclusters: formation, structure elucidation and implications for homochiral polymerization*. Chem. Commun., 2001(18): p. 1854-1855.
9. Julian, R.R., R. Hodyss, B. Kinnear, M.F. Jarrold and J.L. Beauchamp, *Nanocrystalline Aggregation of Serine Detected by Electrospray Ionization Mass Spectrometry: Origin of the Stable Homochiral Gas-Phase Serine Octamer*. Journal of Physical Chemistry B, 2002. **106**(6): p. 1219-1228.
10. Nanita, S.C., E. Sokol and R.G. Cooks, *Alkali metal-cationized serine clusters studied by sonic spray ionization tandem mass spectrometry*. J. Am. Soc. Mass. Spectrom., 2007. **18**(5): p. 856-868.
11. Takats, Z., S.C. Nanita and R.G. Cooks, *Serine Octamer Reactions: Indicators of Prebiotic Relevance*. Angew. Chem. Int. Ed., 2003. **42**(30): p. 3521-3523.
12. Julian, R.R., S. Myung and D.E. Clemmer, *Spontaneous anti-resolution in heterochiral clusters of serine*. J. Am. Chem. Soc., 2004. **126**(13): p. 4110-4111.
13. Nanita, S.C., Z. Takats, R.G. Cooks, S. Myung and D.E. Clemmer, *Chiral enrichment of serine via formation, dissociation, and soft-landing of octameric cluster ions*. J. Am. Soc. Mass. Spectrom., 2004. **15**(9): p. 1360-1365.

14. Takats, Z. and R.G. Cooks, *Thermal formation of serine octamer ions*. Chem. Commun., 2004(4): p. 444-445.
15. Nanita, S.C. and R.G. Cooks, *Serine Octamers: Cluster Formation, Reactions, and Implications for Biomolecule Homochirality*. Angew. Chem. Int. Ed., 2006. **45**(4): p. 554-569.
16. Yang, P.X., R.F. Xu, S.C. Nanita and R.G. Cooks, *Thermal formation of homochiral serine clusters and implications for the origin of homochirality*. J. Am. Chem. Soc., 2006. **128**(51): p. 17074-17086.
17. Perry, R.H., C.P. Wu, M. Neffliu and R.G. Cooks, *Serine sublimates with spontaneous chiral amplification*. Chem. Commun., 2007(10): p. 1071-1073.
18. Weissbuch, I. and M. Lahav, *Crystalline Architectures as Templates of Relevance to the Origins of Homochirality*. Chem. Rev., 2011. **111**(5): p. 3236-3267.
19. Koch, K.J., F.C. Gozzo, S.C. Nanita, Z. Takats, M.N. Eberlin and R.G. Cooks, *Chiral Transmission between Amino Acids: Chirally Selective Amino Acid Substitution in the Serine Octamer as a Possible Step in Homochirogenesis*. Angew. Chem. Int. Ed., 2002. **41**(10): p. 1721-1724.
20. Takats, Z., S.C. Nanita, G. Schlosser, K. Vekey and R.G. Cooks, *Atmospheric Pressure Gas-Phase H/D Exchange of Serine Octamers*. Anal. Chem., 2003. **75**(22): p. 6147-6154.

21. Gronert, S., R.A.J. O'Hair and A.E. Fagin, *Ion/molecule reactions of the protonated serine octamer*. Chem. Commun., 2004(17): p. 1944-1945.
22. Schalley, C.A. and P. Weis, *Unusually stable magic number clusters of serine with a surprising preference for homochirality*. Int. J. Mass spectrom., 2002. **221**(1): p. 9-19.
23. Kong, X., I.A. Tsai, S. Sabu, C.-C. Han, Y.T. Lee, H.-C. Chang, S.-Y. Tu, A.H. Kung and C.-C. Wu, *Progressive Stabilization of Zwitterionic Structures in  $[H(\text{Ser})_{2-8}]^+$  Studied by Infrared Photodissociation Spectroscopy*. Angew. Chem. Int. Ed., 2006. **45**(25): p. 4130-4134.
24. Kong, X., C. Lin, G. Infusini, H.-B. Oh, H. Jiang, K. Breuker, C.-C. Wu, O.P. Charkin, H.-C. Chang and F.W. McLafferty, *Numerous Isomers of Serine Octamer Ions Characterized by Infrared Photodissociation Spectroscopy*. ChemPhysChem, 2009. **10**(15): p. 2603-2606.
25. Sunahori, F.X., G. Yang, E.N. Kitova, J.S. Klassen and Y. Xu, *Chirality recognition of the protonated serine dimer and octamer by infrared multiphoton dissociation spectroscopy*. Phys. Chem. Chem. Phys., 2013. **15**(6): p. 1873-1886.
26. Scutelnic, V., M.A.S. Perez, M. Marianski, S. Warnke, A. Gregor, U. Rothlisberger, M.T. Bowers, C. Baldauf, G. von Helden, T.R. Rizzo

- and J. Seo, *The Structure of the Protonated Serine Octamer*. J. Am. Chem. Soc., 2018.
27. Julian, R.R., R. Hodyss, B. Kinnear, M.F. Jarrold and J.L. Beauchamp, *Nanocrystalline Aggregation of Serine Detected by Electrospray Ionization Mass Spectrometry: Origin of the Stable Homochiral Gas-Phase Serine Octamer*. J. Phys. Chem. B, 2002. **106**(6): p. 1219-1228.
28. Aseev, O., M.A.S. Perez, U. Rothlisberger and T.R. Rizzo, *Cryogenic Spectroscopy and Quantum Molecular Dynamics Determine the Structure of Cyclic Intermediates Involved in Peptide Sequence Scrambling*. J. Phys. Chem. Lett., 2015. **6**(13): p. 2524-2529.
29. Masson, A., M.Z. Kamrath, M.A.S. Perez, M.S. Glover, U. Rothlisberger, D.E. Clemmer and T.R. Rizzo, *Infrared Spectroscopy of Mobility-Selected  $H^+$ -Gly-Pro-Gly-Gly (GPGG)*. J. Am. Soc. Mass. Spectrom., 2015. **26**(9): p. 1444-1454.
30. Ufimtsev, I.S. and T.J. Martinez, *Quantum Chemistry on Graphical Processing Units. 2. Direct Self-Consistent-Field Implementation*. Journal of Chemical Theory and Computation, 2009. **5**(4): p. 1004-1015.
31. Ufimtsev, I.S. and T.J. Martinez, *First principles molecular dynamics simulation of proteins on graphical processing units*. Abstr Pap Am Chem S, 2009. **237**.
32. *TeraChem v 1.5, PetaChem, LLC.* , 2011: <http://www.petachem.com>.

33. Bogar, F. and J. Ladik, *Correlation corrected band structures of homopolypeptides v. B3LYP band structures of 19 homopolypeptides*. Int. J. Quantum Chem, 2004. **99**(1): p. 47-52.
34. Hehre, W.J., R. Ditchfield and J.A. Pople, *Self-Consistent Molecular-Orbital Methods .12. Further Extensions of Gaussian-Type Basis Sets for Use in Molecular-Orbital Studies of Organic-Molecules*. Journal of Chemical Physics, 1972. **56**(5): p. 2257-2261.
35. Antony, J., G.v. Helden, G. Meijer and B. Schmidt, *Anharmonic midinfrared vibrational spectra of benzoic acid monomer and dimer*. Journal of Chemical Physics, 2005. **123**(1): p. 014305.
36. Linder, R., K. Seefeld, A. Vavra and K. Kleinermanns, *Gas phase infrared spectra of nonaromatic amino acids*. Chem. Phys. Lett., 2008. **453**(1): p. 1-6.
37. Kapota, C., J. Lemaire, P. Maître and G. Ohanessian, *Vibrational Signature of Charge Solvation vs Salt Bridge Isomers of Sodiated Amino Acids in the Gas Phase*. J. Am. Chem. Soc., 2004. **126**(6): p. 1836-1842.
38. Oomens, J., J.D. Steill and B. Redlich, *Gas-Phase IR Spectroscopy of Deprotonated Amino Acids*. J. Am. Chem. Soc., 2009. **131**(12): p. 4310-4319.
39. Roscioli, J.R., L.R. McCunn and M.A. Johnson, *Quantum structure of the intermolecular proton bond*. Science, 2007. **316**(5822): p. 249-254.

40. Van Hoozen Jr., B.L. and P.B. Petersen, *Origin of the 900 cm<sup>-1</sup> broad double-hump OH vibrational feature of strongly hydrogen-bonded carboxylic acids*. Journal of Chemical Physics, 2015. **142**(10): p. 104308.
41. Spencer, E.A.C., T. Ly and R.R. Julian, *Formation of the serine octamer: Ion evaporation or charge residue?* Int. J. Mass spectrom., 2008. **270**(3): p. 166-172.
42. Voronina, L., A. Masson, M. Kamrath, F. Schubert, D. Clemmer, C. Baldauf and T. Rizzo, *Conformations of Prolyl–Peptide Bonds in the Bradykinin 1–5 Fragment in Solution and in the Gas Phase*. J. Am. Chem. Soc., 2016. **138**(29): p. 9224-9233.
43. Pereverzev, A.Y., X. Cheng, N.S. Nagornova, D.L. Reese, R.P. Steele and O.V. Boyarkin, *Vibrational Signatures of Conformer-Specific Intramolecular Interactions in Protonated Tryptophan*. J. Phys. Chem. A, 2016. **120**(28): p. 5598-5608.
44. Lorenz, U.J. and T.R. Rizzo, *Multiple Isomers and Protonation Sites of the Phenylalanine/Serine Dimer*. J. Am. Chem. Soc., 2012. **134**(27): p. 11053-11055.
45. Voss, J.M., K.C. Fischer and E. Garand, *Revealing the structure of isolated peptides: IR-IR predissociation spectroscopy of protonated triglycine isomers*. J. Mol. Spectrosc., 2018. **347**: p. 28-34.



46. Masson, A., E.R. Williams and T.R. Rizzo, *Molecular hydrogen messengers can lead to structural infidelity: A cautionary tale of protonated glycine*. J. Chem. Phys., 2015. **143**(10): p. 104313.



## Chapter 4. Spectroscopy of glycans

Glycans span a large spectrum of biological functions. Most notoriously, glycans decorate the surface of cells, where they take part in the recognition processes of cells of the same organism and pathogen cells *via* interactions with intrinsic and extrinsic glycan-binding proteins [1, 2]. It has been shown in mammals that removal of certain glycans from the surface of cells leads to inflammation and defects in immunity. Also, the blood type is determined by the presence of specific glycans exposed on the surface of red blood cells. Furthermore, glycan structure undergoes dramatic modifications in cancerous cells, which accelerates cancer progression [3]. For these reasons, analyzing glycan structure is crucial for the fundamental understanding of cell-to-cell and cell-to-host signaling pathways. However, structural characterization of glycans is complex due to a few reasons:

- (1) Unlike DNA or proteins, glycan synthesis is not template driven.
- (2) The majority of glycan building blocks – monosaccharides – are diastereomers of each other.
- (3) Monosaccharides can attach at different hydroxyl moieties producing regioisomers and branched structures.

The intrinsic isomeric nature of glycans presents difficulties for mass spectrometric determination of their primary structure. Vibrational spectroscopy holds great potential for identifying carbohydrates, owing to different hydrogen bonding patterns of their isomers. For example, infrared multiple photon dissociation (IRMPD) spectroscopy proved to distinguish

isomeric forms of monosaccharides [4, 5] and disaccharides [6, 7]. However, room-temperature spectral fingerprints of larger glycans might have broad features, which could hinder an unambiguous identification. Cryogenic infrared spectroscopy is very sensitive to the slightest change in structure of biomolecules [8-13]. Rizzo and coworkers proposed a combination of messenger-tagging spectroscopy with ion mobility spectrometry (IMS) and mass spectrometry (MS) for glycan identification [9]; data collected for glycans with known structure are deposited into a database, which can be ultimately used to characterize unknown samples. Recently, Garand and coworkers identified eight conformers of sodiated glucose *via* IR-IR spectroscopy. This result shows that carbohydrates are prone to adopt multiple kinetically-trapped conformers in the gas phase [14].

With an alternative combination of techniques, we aim to explore the conformational preferences in a prototype system – protonated glucosamine. For this goal, we use: (1) conformer-selective cryogenic IR spectroscopy, (2) quantum mechanical computations, and (3) isotopic substitution of the reducing end to determine the anomericity of a benchmark system – protonated glucosamine.

### 4.1. Glucosamine as a benchmark

Glucosamine presents a few advantages for testing and validating the new combination of techniques: (1) it protonates easily due to a basic amino group, (2) its compact size and rather rigid ring structure restrict the number of possible conformations and allow a deeper understanding of the

system, and (3) the presence of two types of oscillators (NH and OH) give rise to bands in two different regions of the spectrum that will allow to distinguish them.

### 4.1.1. Infrared laser setup for conformer-selective spectroscopy

In order to obtain infrared spectra of individual conformers, two IR pulses are used, a pump and a probe, separated by a 1  $\mu$ s delay. The IR OPO used for the pump (firing at 5 Hz) is fixed at a frequency specific for a vibrational band of one glucosamine conformer, and the frequency of the probe IR OPO (firing at 10 Hz) is scanned [12, 15]. Because the probe IR pulse induces depletion only when in resonance with any other conformer [16] than the pumped one, the difference of the cycle with and without probe laser produces a dip spectrum of the pumped conformer.

For an improved signal-to-noise ratio, the fluence of the pump IR pulse is increased to saturate the transition of a given conformer. A 50 cm focal length lens, placed at  $\sim$ 60 cm from the cryogenic trap, tightly focuses the pump IR radiation onto the ion cloud. The linearity of the measured IR spectra is maintained due to the low fluence of the probe IR OPO. We achieve weak focusing of the probe pulse by placing a 1 m focal length lens at  $\sim$ 1.5 m from the trap. In this configuration, the divergent light produced in OPO is refocused. Moreover, the horizontal movement of the OPO beam encountered during IR wavelength scanning is substantially reduced in the trap. This has largely enhanced the day-to-day reproducibility of the acquired IR spectra. A periscope installed after the pump OPO changes the

polarization of the OPO radiation from vertical to horizontal, allowing the light to be efficiently transmitted through the entrance window installed at Brewster's angle, thus lowering the amount of reflected light. This may increase the transmitted pump IR power in the trap by a third, increasing the fluence for more exhaustive saturation of the pumped conformer. In addition, the light of the probe OPO, which is counterpropagating with the pump OPO, changes in polarization from vertical to horizontal, and fully reflects from the silicon filter of the pump OPO. The IR pump beam is blocked from entering the probe OPO due to same reasoning. As a consequence, the two IR beams are disentangled.

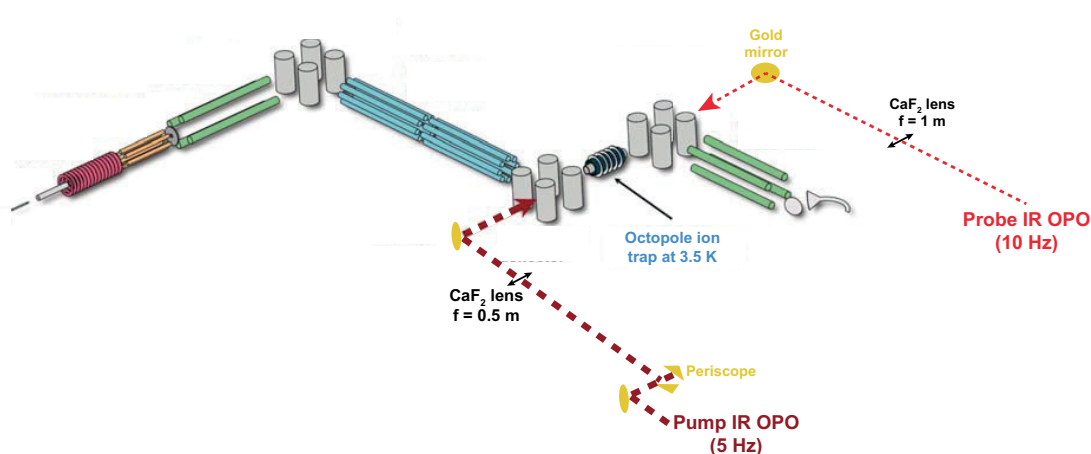


Figure 4.1. Layout of laser optics for IRIR spectroscopy.

#### 4.1.2. Sample preparation

$^{18}\text{O}$  labeling of the reducing end is achieved by dissolving 1.5 mg of dry glucosamine hydrochloride (Sigma-Aldrich, 99% purity) in 150  $\mu\text{L}$  of  $\text{H}_2^{18}\text{O}$  (Sigma-Aldrich, 97% purity) and maintaining the mixture at room

temperature for 48 hours. To increase the  $^{18}\text{O}$ -labeling reaction yield, the reacting mixture is diluted 1:10 in fresh  $\text{H}_2^{18}\text{O}$ . Before electrospraying, the solution is diluted in MeOH (1:100) to reach  $\mu\text{molar}$  range [17, 18]. The isotopically labeled glucosamine is easily separated from the unlabeled one in the quadrupole mass filter.

Galactosamine hydrochloride (99% purity) is purchased from Sigma-Aldrich. The penta- and disaccharides are purchased from Carbosynth (95% purity).

#### 4.1.3. $^{18}\text{O}$ labeling at the reducing end

In the range of  $3150\text{-}3750\text{ cm}^{-1}$ , NH and OH stretch vibrations are the most prominent. The infrared spectrum of protonated glucosamine, which we report in Figure 4.2 (red trace), exhibits 13 distinct lines – more than the total number of NH and OH group oscillators in this molecule. This implies that multiple conformers are produced in the electrospray. Among all the NH and OH groups, only the reducing end OH can be easily isotopically labeled by dissolving dry glucosamine in  $\text{H}_2^{18}\text{O}$ . The  $^{18}\text{O}$  substituted glucosamine spectrum (blue trace in Figure 4.2) differs by two bands from the normal glucosamine- $\text{H}^+$  (red trace in Figure 4.2). The shift of these two bands by  $12\text{ cm}^{-1}$  allows us to assign the two lines to anomeric OH vibrations. The  $12\text{ cm}^{-1}$  shift is consistent with the change in the frequency of an ideal harmonic oscillator, representing the OH group, due to its larger reduced mass. One line shifts per each conformer, indicating that at least two conformers coexist in the gas phase.

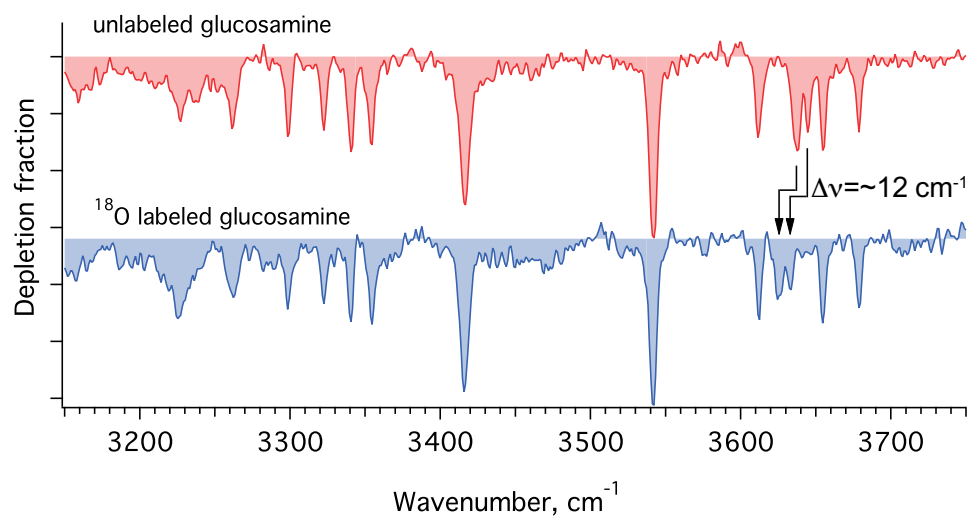


Figure 4.2. IR spectrum of glucosamine- $\text{H}^+$  (red) and glucosamine- $\text{H}^+$  labeled at the glycosidic OH with  $^{18}\text{O}$  (blue).

#### 4.1.4. Conformer-selective spectroscopy of He-tagged protonated glucosamine

The contribution of multiple conformers to the one-laser infrared spectrum renders its interpretation ambiguous. Therefore, we applied IR-IR ion dip spectroscopy to acquire vibrational fingerprints of individual conformers. OH group vibrations are expected to appear in the  $>3400 \text{ cm}^{-1}$  spectral region [14], and NH group vibrations usually appear lower than  $3400 \text{ cm}^{-1}$  [19]. We attempted to sample individual conformers by selectively fixing the pump laser on strongly hydrogen bonded OH bands. Fixing the pump laser at  $3542 \text{ cm}^{-1}$  produces a spectrum with eight bands – more than the total number of stretch vibrations in the molecule – indicating that multiple conformers absorb at  $3542 \text{ cm}^{-1}$  (Figure 4.3). However, pumping at  $3417 \text{ cm}^{-1}$  we seem to obtain a spectrum of a single conformer (A), which



consists of five bands (see Figure 4.4). Fewer bands than the total number of stretch vibrations indicates that they are strongly broadened or overlapping other bands. Exploring the NH stretch region, we identify two other conformers. Fixing the pump laser at  $3340\text{ cm}^{-1}$  we obtain the fingerprint IR spectrum of conformer B, and fixing the pump at  $3323\text{ cm}^{-1}$  produces the spectrum of the conformer C.

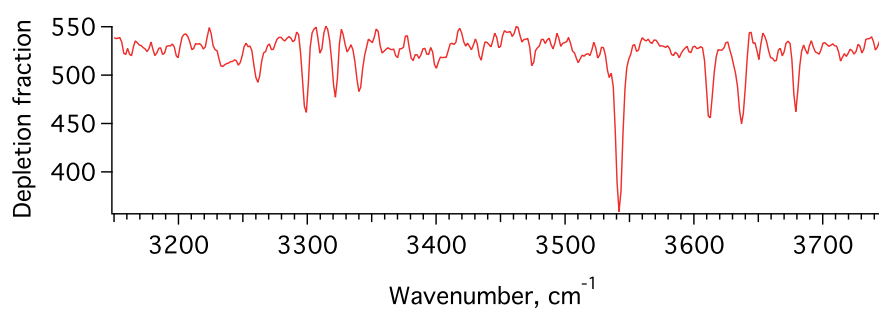


*Figure 4.3. IR spectrum acquired with the pump laser fixed at  $3542\text{ cm}^{-1}$ , while the probe laser is scanned. The presence of 8 well-resolved bands suggests that at least two conformers absorb at  $3542\text{ cm}^{-1}$ .*

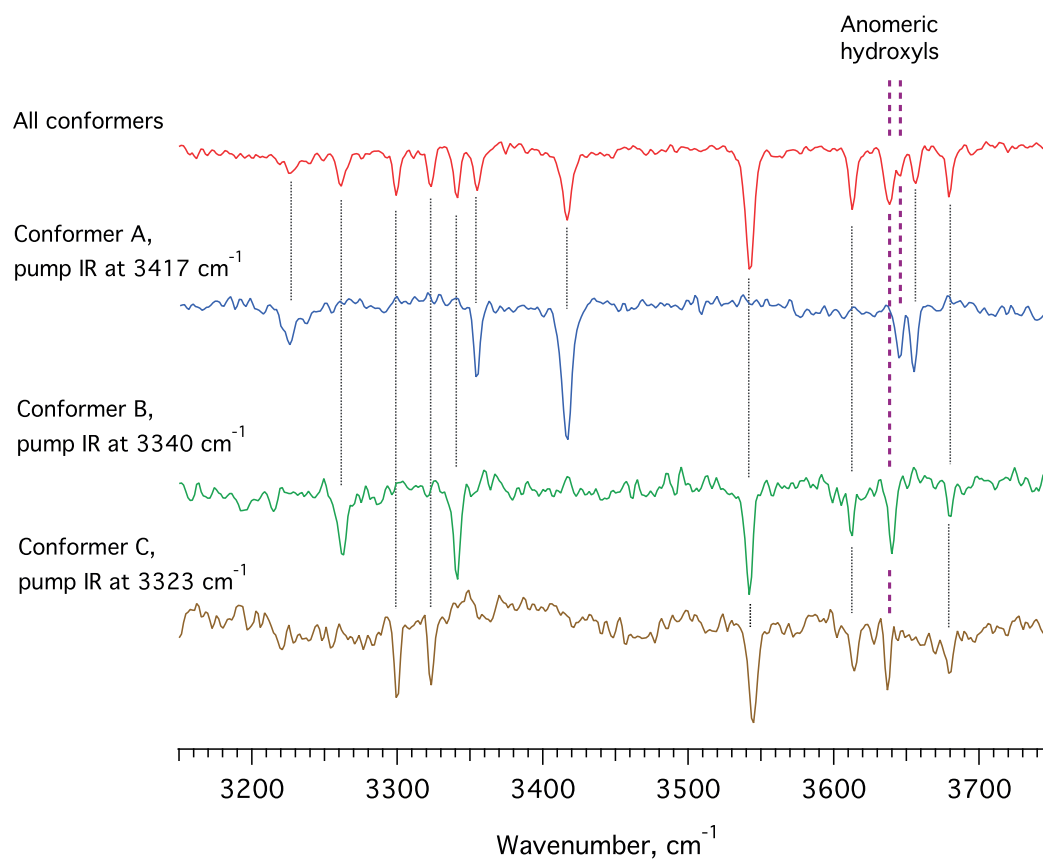


Figure 4.4. Red trace is the non-conformer specific spectrum. Blue, green and brown traces are double resonance spectra. Purple dashed lines indicate the bands assigned to anomeric hydroxyl via  $^{18}\text{O}$  substitution (Figure 4.2).

The sum of conformer-specific spectra A, B and C (Figure 4.5), reproduces well the one-laser spectrum, meaning that all the most abundant conformers of glucosamine- $\text{H}^+$  are successfully sampled. The overlap of the anomeric OH bands in spectra B and C gives the justification for the shift of two lines – and not three – in the  $^{18}\text{O}$  isotopic labeling experiment (Figure 4.2).

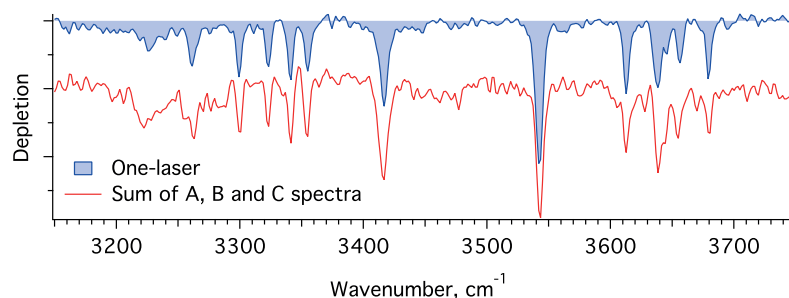


Figure 4.5. Comparison between one-laser spectrum and the sum of all the conformer-selective spectra.

The distinctive OH band pattern of the spectrum A, compared with B and C, indicates a different hydrogen-bond network of the OH groups in the conformer A. Even though the positions of the OH bands are nearly identical in the spectra B and C, NH bands are highly sensitive to fine structural changes of their environment, allowing us to definitively distinguish conformers B and C. Considering the isotopic labeling (Figure 4.2) and the IR spectra of each conformer (Figure 4.4), we identify the bands of the anomeric OH groups: 3645, 3640 and 3637  $\text{cm}^{-1}$  (in spectra A, B and C, respectively).

#### 4.1.5. Synergistic effect and saturation of the detector

A direct subtraction of the signal in cycles with and without pump laser, fixed at 3417  $\text{cm}^{-1}$ , leads to IR spectra with gain bands that correspond to the conformers B and C (blue trace in Figure 4.6). The origin of these bands is in the synergistic effect of two IR pulses, *i.e.* two IR pulses deplete more helium tags than when each IR laser fires in separate cycles. Jašík *et*

*al.* [16] observed a similar effect. The most feasible explanation for this phenomenon is the nonlinear response (saturation) of the channeltron detector.

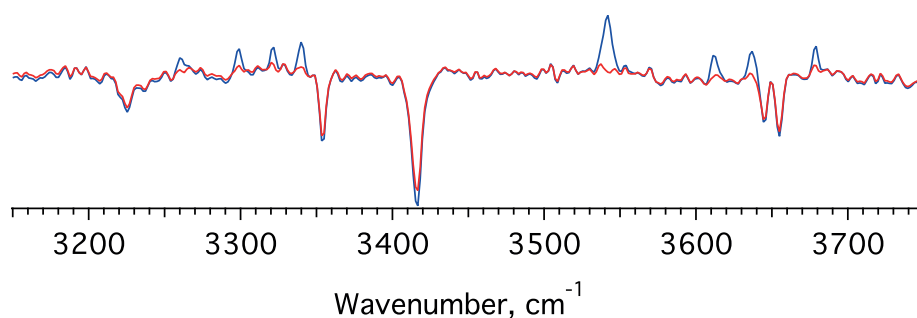


Figure 4.6. Blue: direct subtraction of signals in cycles with and without pump laser fixed at  $3417\text{ cm}^{-1}$ . Red: subtraction after correction for channeltron nonlinearity.

The hypothesis of detector saturation is supported by the measured isotope ratio of a dipeptide ( $\text{GlyTrpH}^+$ ). The ratio of the  $^{13}\text{C}$  isotope peak to the monoisotopic peak is consistent with the expected isotope ratio (0.1552 for  $\text{GlyTrpH}^+$ ) only at low number of detected ions. When the ion packet of the monoisotopic mass ions is  $>100$  ions, the counted number of ions deviates nearly linearly from the real number of ions (Figure 4.7). We assume that the  $^{13}\text{C}$  isotope ions are counted correctly, which is a fair approximation, since in this range the number of  $^{13}\text{C}$  isotope ions is up to  $\sim 100$  counts. This allows to derive a calibration curve (Figure 4.8), which is used to correct the measured ion signal. After considering the calibration of the detector, the false gain peaks disappear (red trace in Figure 4.6). The

same calibration is applied to all the conformer-selective IR spectra in Figure 4.4.

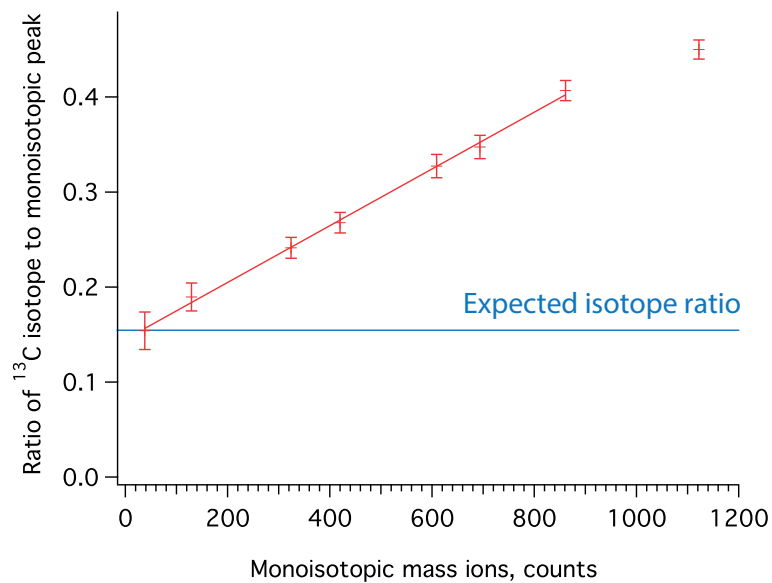


Figure 4.7. Ratio of the measured  $^{13}\text{C}$  isotope peak to the monoisotopic peak of  $\text{GlyTrpH}^+$  peptide.

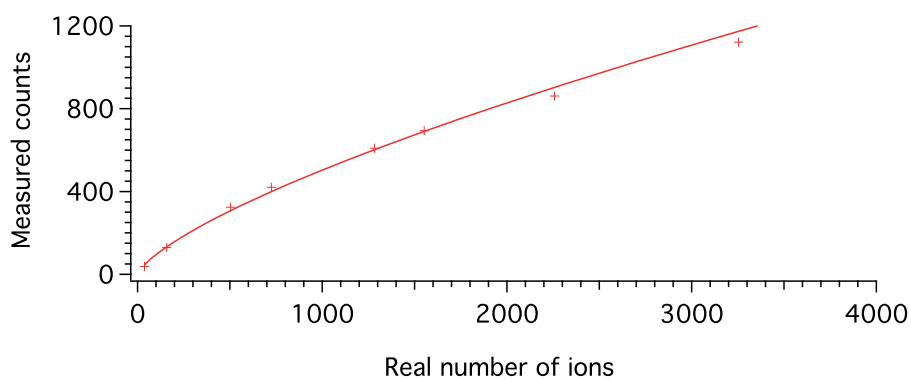


Figure 4.8. Calibration curve for the measured ion signal on the channeltron.

#### 4.1.6. Conformational space sampling

In order to determine the structures of the three conformers we proceed with a conformational search for protonated glucosamine. Given the simplicity of the system, the candidate low-energy conformations are determined following a set of rules: 1) the pyranose cycle can adopt chair, boat or skew-boat conformations (half-chair and envelope are usually transition-state geometries) [20, 21]; 2) the group repulsion (in the case of large axial substituents in chair conformations) imposes an energetic penalty that can be compensated with efficient hydrogen bonds; 3) charge directs the hydrogen bonding pattern [22, 23], and 4) hydrogen bonds that complete a ring of 6 or 7 atoms are stronger than 5-atom rings. The generated pool of conformers is further optimized at a B3LYP/6-31+G(d,p) level of theory.

#### 4.1.7. Predicted structures of protonated glucosamine

Figure 4.9 illustrates the comparison of the experimental and calculated spectra of glucosamine. Theoretical vibrational spectra of the computed structures agree well with the experimental spectra; moreover, they are consistent with the assignments of the reducing end OH bands (Figure 4.4). Conformers A and B are  $\alpha$ -anomers, and C is a  $\beta$ -anomer. The computed structure A (Figure 4.9a) adopts a  ${}^1C_4$  chair conformation, in contrast to the  ${}^4C_1$  structures for B and C (Figure 4.9b,c). This explains the difference in the OH stretch region of the spectrum. Conformer A is the lowest energy structure due to strong hydrogen bonding (in a 7-membered cycle) that is reflected in the large shift of the OH band to  $3417\text{ cm}^{-1}$ ; the corresponding hydrogen-bond length of this OH group is  $1.8\text{ \AA}$  (Figure 4.9a).

## Chapter 4. Spectroscopy of glycans

In structure B, two OH groups form hydrogen bonds with lengths of 2.0 and 2.5 Å, their corresponding frequencies being 3542 and 3611  $\text{cm}^{-1}$  (in good agreement with [14]). The pattern of OH bands of conformer C strongly resembles the one for conformer B, although some OH bands are slightly blue-shifted (by  $\sim 3 \text{ cm}^{-1}$ ). The anomeric OH group participates in hydrogen bonding with the neighboring amino group, which makes the NH spectral region susceptible to structural changes in  $\alpha$ - and  $\beta$ -anomers.

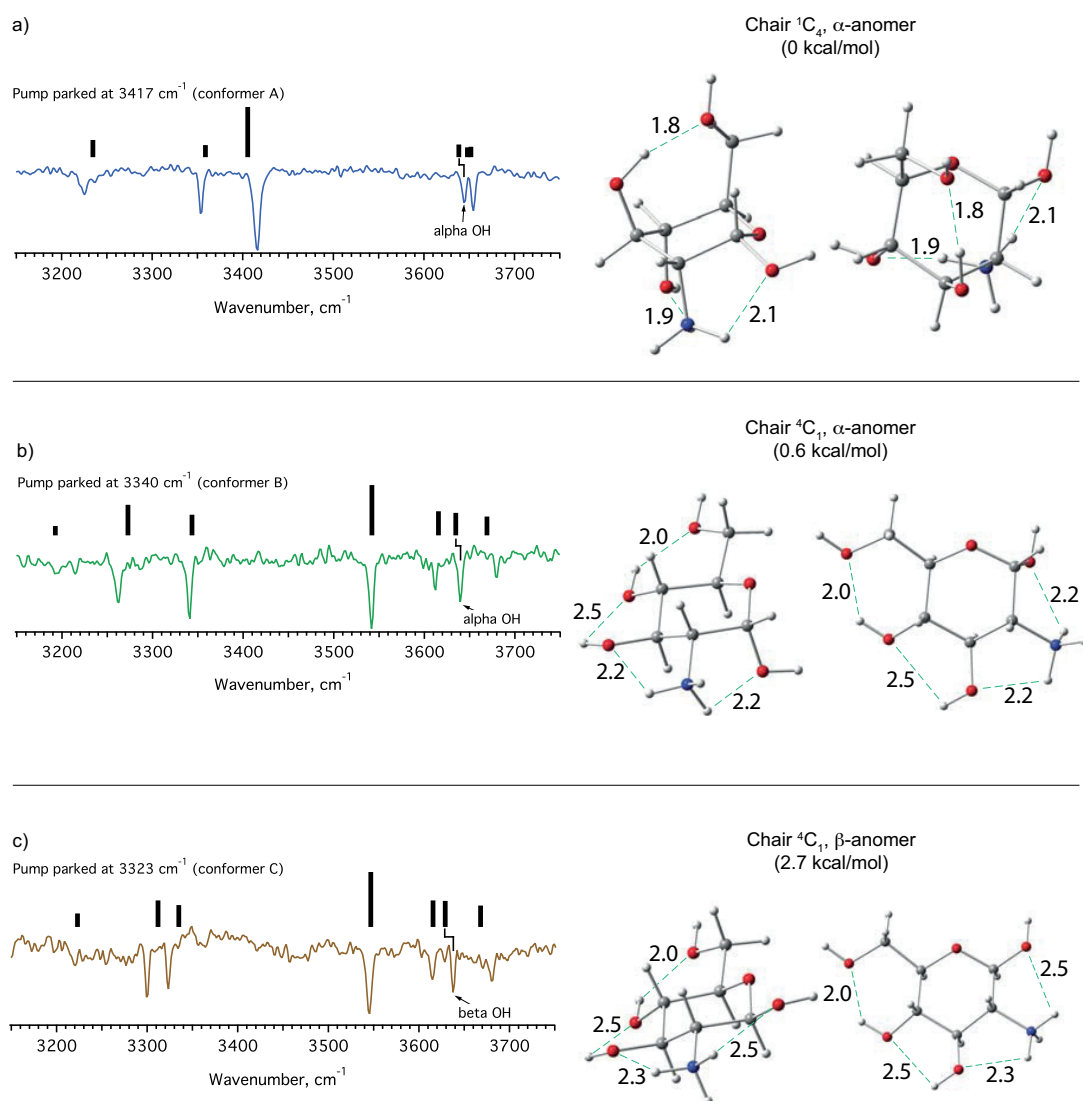


*Figure 4.9. Computed spectra of conformers that match experiment and their corresponding structures are shown from two viewpoints. A uniform 0.955 anharmonic scaling factor is used in all cases. Relative energies including zero-point energy corrections are given in brackets. Hydrogen bonds are depicted with green dashes and their length is given in Å.*

The free anomeric OH bands occur around  $3640\text{ cm}^{-1}$ , in contrast to the highest resonant frequency of the alcohol OH group ( $3680\text{ cm}^{-1}$ ). The reason for this redshift is the strong inductive (electronic withdrawing) effect of the neighboring oxygen atom inside the pyranose ring, which weakens the reducing end OH bond force constant.

#### 4.1.8. Power dependence and abundance of conformers

Previous studies determined the  $\alpha:\beta$  ratio of glucosamine in solution as 1.7:1 (polarimetric measurements and NMR [24]) and 2.6:1 (microchip capillary electrophoresis [25]). In the gas phase, one can use the IR fluence dependence of the depletion (see Equation 2.27) to determine the abundance of the corresponding conformer. We tune the IR OPO to a frequency, where only one conformer absorbs and change the IR fluence, which is achieved by changing the IR power and keeping the photon beam area the same [16]. Assuming that any He-tagged ion that absorbs an IR photon loses the tag, and extrapolating to infinite power, one obtains the approximate abundance of the given conformer in the irradiated volume of the ion cloud. In this way, we estimate the relative conformer population (Figure 4.10): 0.19 for



conformer A, 0.14 for conformer B, and 0.19 for conformer C, or 1.3:1:1.3. The individual populations do not add up to unity, because part of the ion cloud is not irradiated.

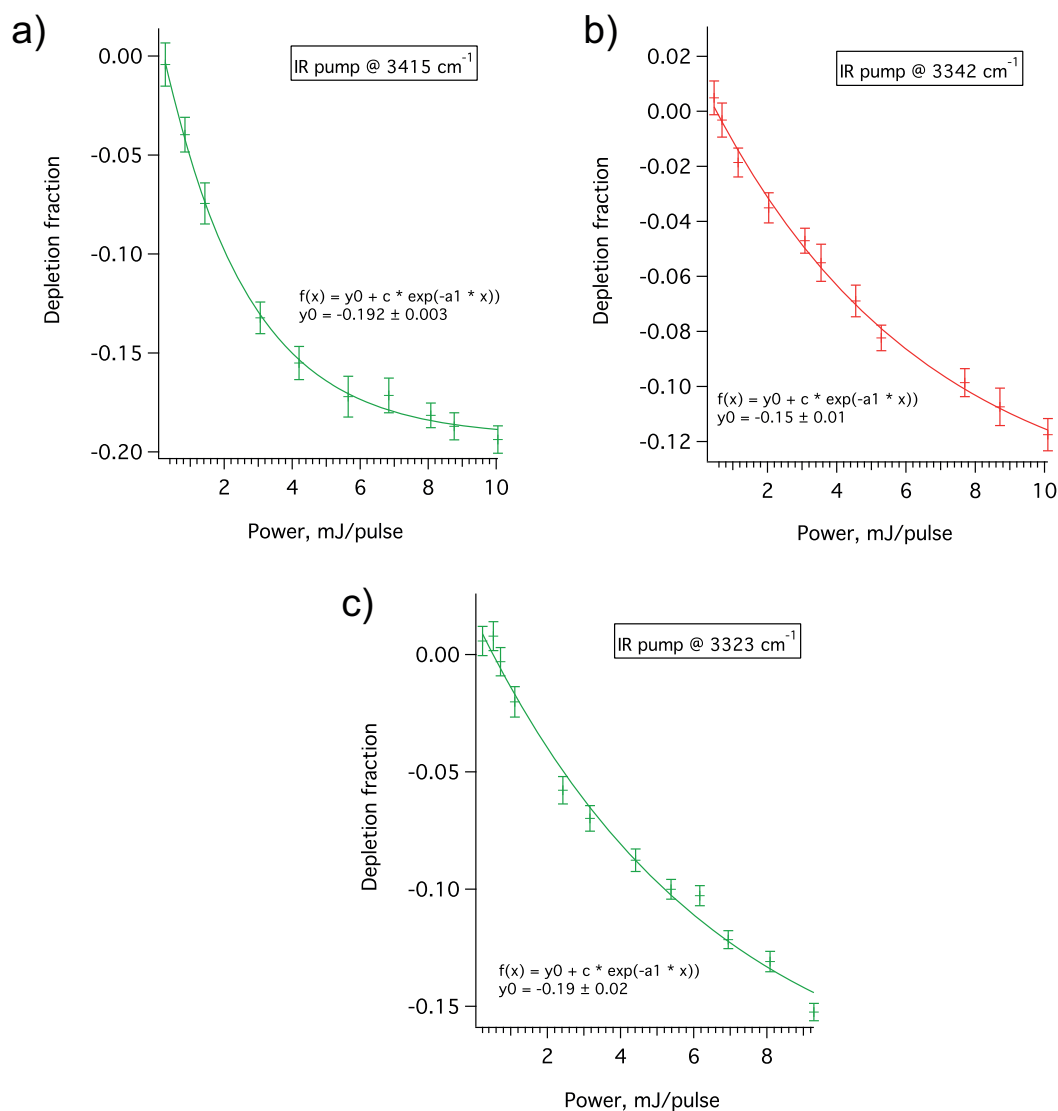


Figure 4.10. Measurement of the conformer population. The ions are irradiated with IR light resonant with one conformer, and the power is increased to saturate the IR transition. The power dependence is fitted with an exponential function, where  $y_0$  is the depletion at infinite power.

Consequently, the  $\alpha:\beta$  ratio of the gas-phase protonated glucosamine is  $\sim 1.8:1$  – comparable to the solution-phase ratio. This is not surprising, since the large energy barrier does not allow the  $\alpha/\beta$  mutarotation in the gas phase. However, the conformers A and B – both  $\alpha$ -anomers – are free to interchange in the gas phase, and the equal population of A and B found in experiment is consistent with the small difference between their predicted free energies (0.6 kcal/mol at 0K, which further decreases to -0.1 kcal/mol at 300K). In contrast to protonated glucosamine, the  $\text{Na}^+(\text{glucose})$  adduct exhibits a larger number of conformers due to strong binding of the coordinating metal to a few hydroxyl groups that hinders the interconversion of conformers [14, 21]. The presence of a proton in glucosamine does not hinder the interconversion of conformers as strongly as the coordinating metal.

#### 4.2. Protonated galactosamine

Galactosamine and glucosamine are structurally very similar: the only difference between these two monosaccharides is the stereochemistry of the C-4 atom. Nevertheless, the IR spectrum of protonated galactosamine is strikingly different from the one of protonated glucosamine (Figure 4.11). Since we resolve fewer bands in the former compared to the latter (10 *vs.* 13 bands), this suggests the presence of only two conformers for galactosamine- $\text{H}^+$ .

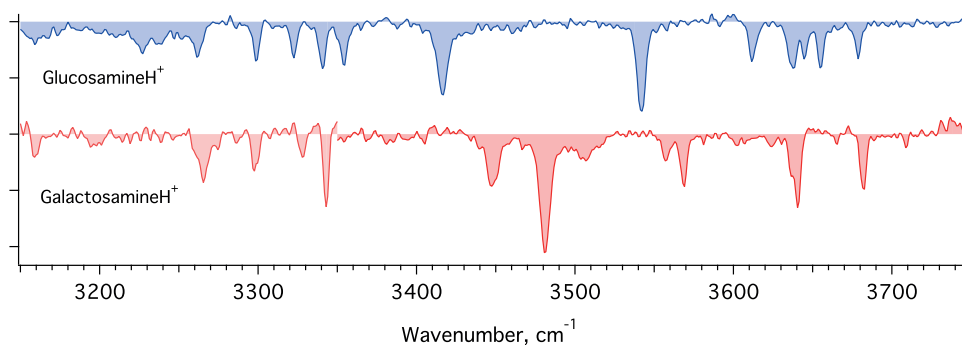
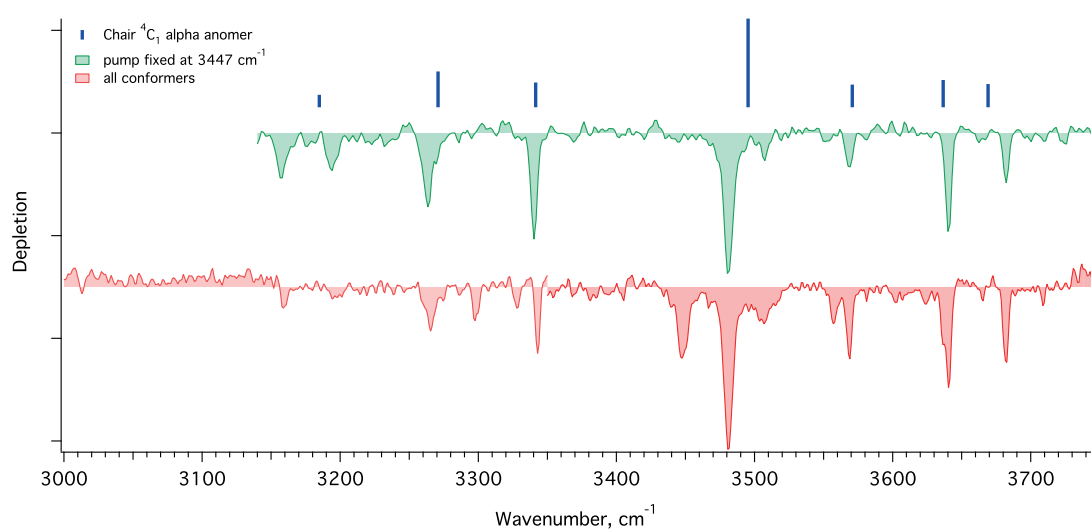


Figure 4.11. IR spectra of protonated glucosamine and galactosamine exhibit different vibrational features.

Burned the minor conformer at 3447 cm<sup>-1</sup> with the pump laser, we obtained another spectrum of the protonated galactosamine (green trace in Figure 4.12). Quantum mechanical modeling shows that the green spectrum corresponds to the <sup>4</sup>C<sub>1</sub> α anomer (image in Figure 4.12). The fine differences between the hydrogen bonding network of <sup>4</sup>C<sub>1</sub> α anomer of galactosamine-H<sup>+</sup> and of <sup>4</sup>C<sub>1</sub> α anomer of glucosamine-H<sup>+</sup> are the cause of such distinctly different IR spectra.



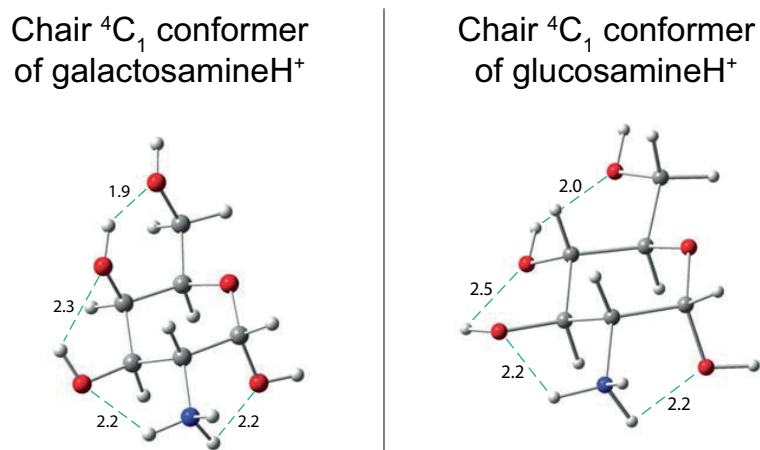


Figure 4.12. Red trace: IR spectrum of all the conformers of galactosamine- $H^+$ ; green trace: IR spectrum obtained by burning the conformer at  $3447\text{ cm}^{-1}$ ; blue sticks: theoretical spectrum of the chair  ${}^4C_1$   $\alpha$  anomer that matches the green spectrum. Bottom left: candidate structure of protonated galactosamine; bottom right: structure of conformer B of glucosamine- $H^+$  (reproduced from Figure 4.9).

Further experiments are needed to obtain the structures of all galactosamine- $H^+$  conformers and to establish the relation between the abundance of the  $\alpha:\beta$  anomers in the gas phase and in solution.

#### 4.3. IR spectroscopy of a deprotonated pentasaccharide

The database approach for glycan identification proposed by Rizzo and coworkers is based on the spectroscopic identification of glycans complexed with  $\text{Na}^+$ , which proved to have unique fingerprint IR spectra [9]. Glycans easily form complexes with alkali ions due to their multiple hydroxyl groups. Another efficient way to charge glycans is by

deprotonation, and it is plausible that anionic glycans could provide suitable spectra for the database. However, Struwe *et al.* identified that the deprotonation site in negatively ionized glycans may migrate in the gas phase [26]. Such a charge migration might cause multiple conformations to be trapped at 10K, and as a result, the IR spectrum would be highly congested.

To test this line of reasoning, we electrospray a pentasaccharide in negative mode and obtain an IR spectrum using our helium tagging technique (blue trace in Figure 4.13). Indeed, the characteristic bands observed in the IR fingerprint of the He-tagged sodiated pentasaccharide (around  $3320\text{ cm}^{-1}$ ,  $3500\text{ cm}^{-1}$  and  $3650\text{ cm}^{-1}$ ) disappear in the broad spectrum of the deprotonated mannopentaose. Such a structureless spectrum might present difficulties to be distinguished from other spectra of glycans. However, comparing He and  $\text{N}_2$  tagging, we observe similar prominent features in both spectra (red and green traces in Figure 4.13).

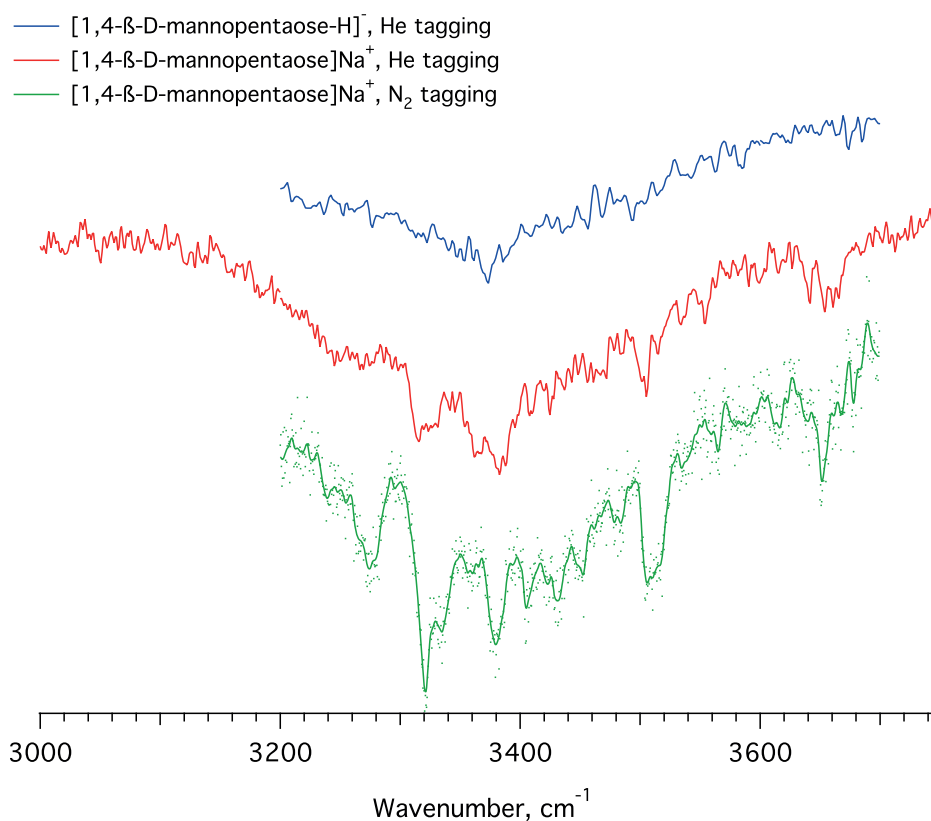


Figure 4.13. IR spectra of 1,4-β-D-mannopentaose in positive and negative mode. N<sub>2</sub> tagging spectrum is adapted from ref. [9].

#### 4.4. Collision-induced dissociation

Schindler *et al.* provided some examples, in which glycan fragments retain anomeric memory of the glycosidic bond from the precursor glycan [6], and proposed to sequence glycans analyzing spectroscopically the fragments. In this section we explore the cryogenic IR spectroscopy of disaccharide fragments produced *via* collision-induced dissociation (CID). Throughout this chapter we name the CID fragments of disaccharides according to Domon-Costello nomenclature [27] (Figure 4.14).

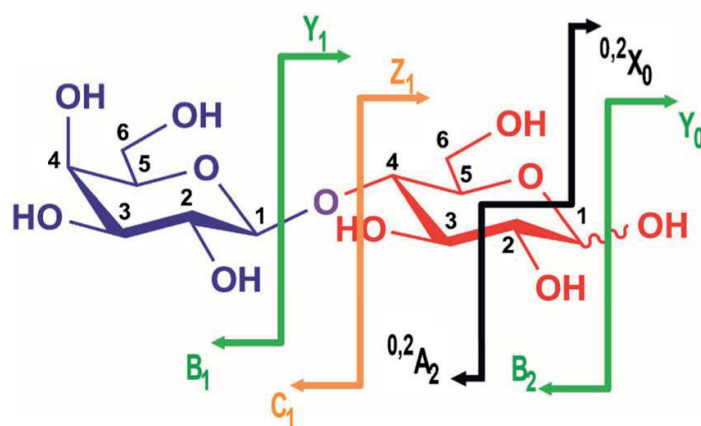


Figure 4.14. Domon-Costello nomenclature for glycan fragmentation (reproduced from ref. [28]).

We induce fragmentation of electrosprayed glycans at the interface of the funnel and hexapole ion guide applying a high voltage drop (30-60 V) from the last electrode of the funnel to the pole bias of the hexapole ion trap (see Figure 2.1).

In the first experiment, we electrospray protonated disaccharides. The IR spectra of the c fragments of GalNAc( $\beta$ 1-3)GalH<sup>+</sup> and GalNAc( $\alpha$ 1-3)GalH<sup>+</sup> are given in the Figure 4.15 (green and red traces, respectively). The IR spectrum of the c fragment of GalNAc( $\beta$ 1-3)GalH<sup>+</sup> resembles that of its anomeric homologue – the c fragment of GalNAc( $\alpha$ 1-3)GalH<sup>+</sup>; both fragments have a striking similarity to the spectrum of GalNAcH<sup>+</sup> electrosprayed from solution (blue trace in Figure 4.15). This result suggests that the protonated c fragments structurally resemble the protonated

GalNAc. The additional lines in the green spectrum might be due to a new conformer produced during fragmentation.

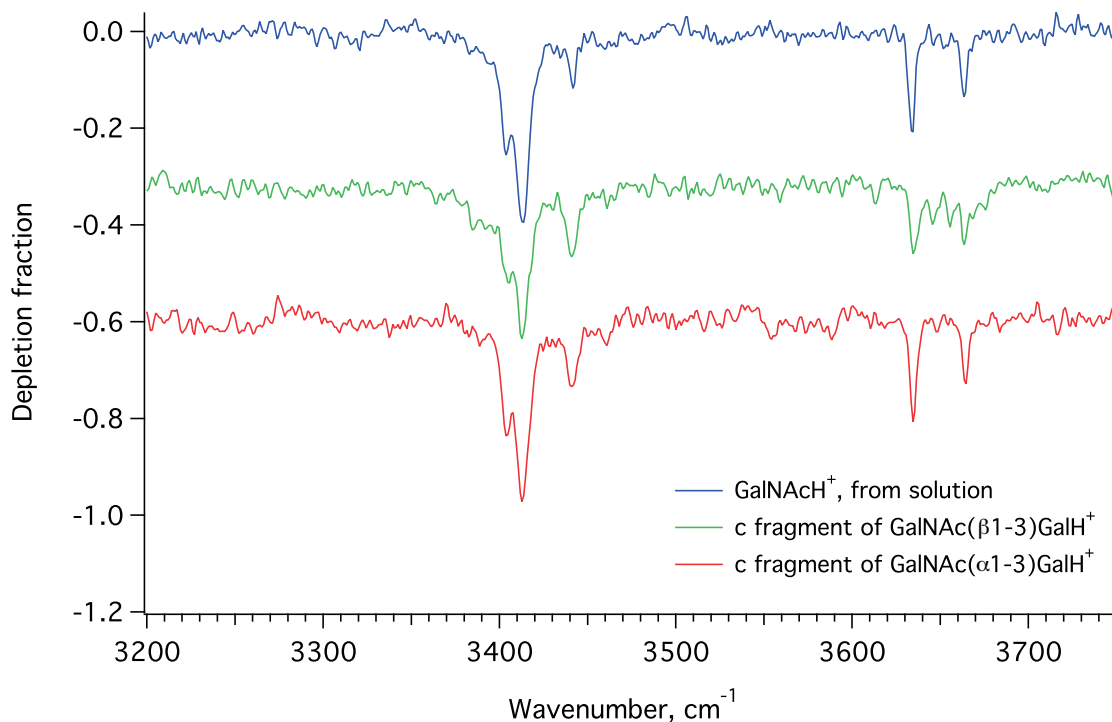


Figure 4.15. IR spectrum of protonated GalNAc from solution (blue), protonated c fragment originating from GalNAc( $\beta$ 1-3)GalH<sup>+</sup> (green) and protonated GalNAc( $\alpha$ 1-3)GalH<sup>+</sup> (red).

In the second experiment, we induce fragmentation of the Gal( $\beta$ 1-3)GalNAcNa<sup>+</sup> disaccharide, and we select the sodiated c fragment – the one corresponding to galactose complexed with Na<sup>+</sup>. The IR fingerprint for the sodiated c fragment has no similarity to that of sodiated galactose (Figure 4.16). We conclude that sodium cation interferes with the disaccharide fragmentation and gives rise to a structure that differs from the sodiated galactose. Further investigation with the aid of quantum mechanical



computations is necessary to elucidate the fragmentation mechanism in the presence of  $\text{Na}^+$ .

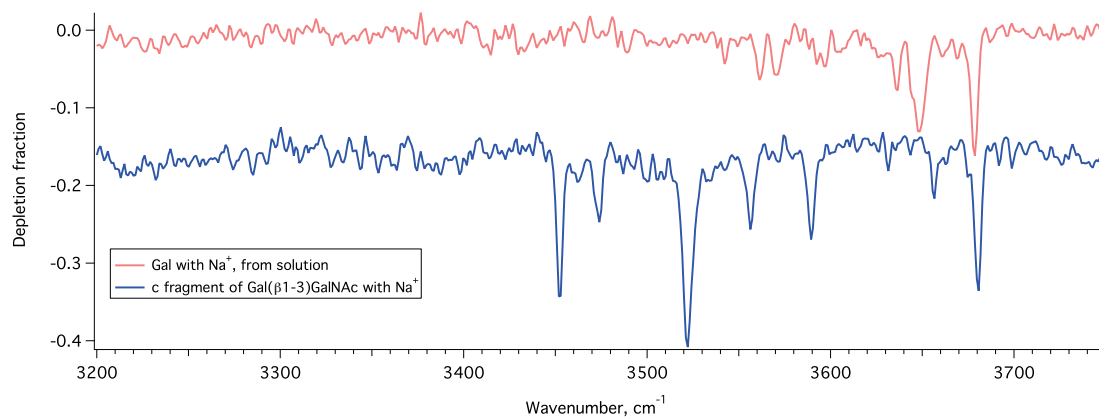


Figure 4.16. Sodiated galactose from solution (red) and sodiated *c* fragment (blue) of  $\text{Gal}(\beta 1-3)\text{GalNAcNa}^+$ .

#### 4.5. Summary

In this chapter we use conformer-selective infrared spectroscopy as a sensitive tool for structural identification of protonated glucosamine. The well-resolved spectra provide critical insights into the nature of hydrogen-bonding interactions in the studied monosaccharide. The facile  $^{18}\text{O}$  labeling of the reducing end combined with cryogenic IR spectroscopy of a carbohydrate allows us to estimate its conformational heterogeneity – the number of shifting bands indicates the minimal number of the gas-phase conformers. Conformer-selective cryogenic ion spectroscopy and isotopic labeling may provide important information about fragmentation mechanisms of larger glycans that could assist the development of a universal glycan *de novo* sequencing scheme.

References:

1. Varki, A., *Biological roles of glycans*. Glycobiology, 2017. **27**(1): p. 3-49.
2. Rudd, P.M., T. Elliott, P. Cresswell, I.A. Wilson and R.A. Dwek, *Glycosylation and the Immune System*. Science, 2001. **291**(5512): p. 2370-2376.
3. Varki, A., R.D. Cummings and J.D. Esko, *Essentials of Glycobiology*. 2015-2017, Cold Spring Harbor Laboratory Press: Cold Spring Harbor (NY).
4. Contreras, C.S., N.C. Polfer, J. Oomens, J.D. Steill, B. Bendiak and J.R. Eyler, *On the path to glycan conformer identification: Gas-phase study of the anomers of methyl glycosides of N-acetyl-D-glucosamine and N-acetyl-D-galactosamine*. Int. J. Mass spectrom., 2012. **330-332**: p. 285-294.
5. Tan, Y., N. Zhao, J. Liu, P. Li, C.N. Stedwell, L. Yu and N.C. Polfer, *Vibrational Signatures of Isomeric Lithiated N-acetyl-D-hexosamines by Gas-Phase Infrared Multiple-Photon Dissociation (IRMPD) Spectroscopy*. J. Am. Soc. Mass. Spectrom., 2017. **28**(3): p. 539-550.
6. Schindler, B., L. Barnes, G. Renois, C. Gray, S. Chambert, S. Fort, S. Flitsch, C. Loison, A.-R. Allouche and I. Compagnon, *Anomeric memory of the glycosidic bond upon fragmentation and its consequences for carbohydrate sequencing*. Nature Communications, 2017. **8**(1): p. 973.

7. Gray, C.J., B. Schindler, L.G. Migas, M. Pičmanová, A.R. Allouche, A.P. Green, S. Mandal, M.S. Motawia, R. Sánchez-Pérez, N. Bjarnholt, B.L. Møller, A.M. Rijs, P.E. Barran, I. Compagnon, C.E. Eyers and S.L. Flitsch, *Bottom-Up Elucidation of Glycosidic Bond Stereochemistry*. *Anal. Chem.*, 2017. **89**(8): p. 4540-4549.
8. Masson, A., M.Z. Kamrath, M.A.S. Perez, M.S. Glover, U. Rothlisberger, D.E. Clemmer and T.R. Rizzo, *Infrared Spectroscopy of Mobility-Selected H<sup>+</sup>-Gly-Pro-Gly-Gly (GPGG)*. *J. Am. Soc. Mass. Spectrom.*, 2015. **26**(9): p. 1444-1454.
9. Masellis, C., N. Khanal, M.Z. Kamrath, D.E. Clemmer and T.R. Rizzo, *Cryogenic Vibrational Spectroscopy Provides Unique Fingerprints for Glycan Identification*. *J. Am. Soc. Mass. Spectrom.*, 2017. **28**(10): p. 2217-2222.
10. Voronina, L., A. Masson, M. Kamrath, F. Schubert, D. Clemmer, C. Baldauf and T. Rizzo, *Conformations of Prolyl–Peptide Bonds in the Bradykinin 1–5 Fragment in Solution and in the Gas Phase*. *J. Am. Chem. Soc.*, 2016. **138**(29): p. 9224-9233.
11. Zabuga, A.V. and T.R. Rizzo, *Capping Motif for Peptide Helix Formation*. *J. Phys. Chem. Lett.*, 2015. **6**(9): p. 1504-1508.
12. Pereverzev, A.Y., X. Cheng, N.S. Nagornova, D.L. Reese, R.P. Steele and O.V. Boyarkin, *Vibrational Signatures of Conformer-Specific Intramolecular Interactions in Protonated Tryptophan*. *J. Phys. Chem. A*, 2016. **120**(28): p. 5598-5608.

13. Stearns, J.A., C. Seaiby, O.V. Boyarkin and T.R. Rizzo, *Spectroscopy and Conformational Preferences of Gas-Phase Helices*. Phys. Chem. Chem. Phys., 2009. **11**(1): p. 125-132.
14. Voss, J.M., S.J. Kregel, K.C. Fischer and E. Garand, *IR-IR Conformation Specific Spectroscopy of Na+(Glucose) Adducts*. J. Am. Soc. Mass. Spectrom., 2017.
15. Pereverzev, A.Y., V. Kopysov and O.V. Boyarkin, *High Susceptibility of Histidine to Charge Solvation Revealed by Cold Ion Spectroscopy*. Angew. Chem. Int. Ed., 2017. **56**(49): p. 15639-15643.
16. Jašík, J., D. Gerlich and J. Roithová, *Two-Color Infrared Predissociation Spectroscopy of C<sub>6</sub>H<sub>6</sub><sup>2+</sup> Isomers Using Helium Tagging*. J. Phys. Chem. A, 2015. **119**(11): p. 2532-2542.
17. Tan, Y. and N.C. Polfer, *Linkage and Anomeric Differentiation in Trisaccharides by Sequential Fragmentation and Variable-Wavelength Infrared Photodissociation*. J. Am. Soc. Mass. Spectrom., 2015. **26**(2): p. 359-368.
18. Fang, T.T. and B. Bendiak, *The Stereochemical Dependence of Unimolecular Dissociation of Monosaccharide-Glycolaldehyde Anions in the Gas Phase: A Basis for Assignment of the Stereochemistry and Anomeric Configuration of Monosaccharides in Oligosaccharides by Mass Spectrometry via a Key Discriminatory Product Ion of Disaccharide Fragmentation, m/z 221*. J. Am. Chem. Soc., 2007. **129**(31): p. 9721-9736.

19. Stearns, J.A., S. Mercier, C. Seaiby, M. Guidi, O.V. Boyarkin and T.R. Rizzo, *Conformation-Specific Spectroscopy and Photodissociation of Cold, Protonated Tyrosine and Phenylalanine*. J. Am. Chem. Soc., 2007. **129**(38): p. 11814-11820.
20. Mayes, H.B., L.J. Broadbelt and G.T. Beckham, *How Sugars Pucker: Electronic Structure Calculations Map the Kinetic Landscape of Five Biologically Paramount Monosaccharides and Their Implications for Enzymatic Catalysis*. J. Am. Chem. Soc., 2014. **136**(3): p. 1008-1022.
21. Heaton, A.L. and P.B. Armentrout, *Experimental and Theoretical Studies of Sodium Cation Interactions with d-Arabinose, Xylose, Glucose, and Galactose*. J. Phys. Chem. A, 2008. **112**(41): p. 10156-10167.
22. Scutelnic, V., M.A.S. Perez, M. Marianski, S. Warnke, A. Gregor, U. Rothlisberger, M.T. Bowers, C. Baldauf, G. von Helden, T.R. Rizzo and J. Seo, *The Structure of the Protonated Serine Octamer*. J. Am. Chem. Soc., 2018.
23. Seo, J., S. Warnke, K. Pagel, M.T. Bowers and G. von Helden, *Infrared spectrum and structure of the homochiral serine octamer-dichloride complex*. Nat. Chem., 2017. **9**: p. 1263.
24. Horton, D., J.S. Jewell and K.D. Philips, *Anomeric Equilibria in Derivatives of Amino Sugars. Some 2-Amino-2-deoxy-D-hexose Derivatives 1-3*. The Journal of Organic Chemistry, 1966. **31**(12): p. 4022-4025.

25. Skelley, A.M. and R.A. Mathies, *Rapid on-column analysis of glucosamine and its mutarotation by microchip capillary electrophoresis*. J. Chromatogr. A, 2006. **1132**(1): p. 304-309.
26. Struwe, W.B., C. Baldauf, J. Hofmann, P.M. Rudd and K. Pagel, *Ion mobility separation of deprotonated oligosaccharide isomers - evidence for gas-phase charge migration*. Chem. Commun., 2016. **52**(83): p. 12353-12356.
27. Domon, B. and C.E. Costello, *A systematic nomenclature for carbohydrate fragmentations in FAB-MS/MS spectra of glycoconjugates*. Glycoconjugate J., 1988. **5**(4): p. 397-409.
28. Bythell, B.J., M.T. Abutokaikah, A.R. Wagoner, S. Guan and J.M. Rabus, *Cationized Carbohydrate Gas-Phase Fragmentation Chemistry*. J. Am. Soc. Mass. Spectrom., 2017. **28**(4): p. 688-703.

## Chapter 5. Electronic energy transfer<sup>2</sup>

In this chapter, we discuss the excited state dynamics in a gas-phase bichromophoric peptide of a well-defined geometry. The objective of this work is to measure electronic energy transfer rates of a gas-phase peptide of well-defined geometry in a cryogenic ion trap. We use infrared-ultraviolet (IR-UV) double resonance [1] to obtain a ground-state infrared (IR) spectrum of each conformer as well as to determine its contribution to the electronic spectrum. By comparing these highly resolved IR spectra with those computed for the lowest energy conformers determined by theory, we can define the distance between the chromophores and their relative orientation. We use an ultraviolet (UV) laser pulse to promote a single conformer to the excited state of a specific chromophore. An IR laser then probes the electronically excited molecules, producing a unique spectral fingerprint that is characteristic of each electronic state. Monitoring specific IR transitions as a function of the delay time between pump and probe pulses provides a measure of the excited state lifetimes and hence the absolute rates of electronic energy transfer.

---

<sup>2</sup> The content of this chapter is partially based on the material from the article: V. Scutelnic, A. Prlj, A. Zabuga, C. Corminboeuf, and T. Rizzo: “Infrared spectroscopy as a probe of electronic energy transfer”, *J. Phys. Chem. Lett.*, 2018, 9, p. 3217-3223. The article is available online under the link: <https://pubs.acs.org/doi/10.1021/acs.jpcclett.8b01216>

### 5.1. Model peptide for energy transfer studies

We chose to test notions about electronic energy transfer in a model peptide with the sequence Ac-FAYK-H<sup>+</sup>. The photochemistry of short peptides containing phenylalanine or tyrosine chromophores has been extensively characterized [2-8], making Ac-FAYK-H<sup>+</sup> an ideal system in which to study electronic energy transfer. The C-terminal lysine side chain induces strong hydrogen bonds with the backbone carbonyls [9], forming the capping motif [10] of a  $3_{10}$  helix [11]. This provides a well-defined scaffold for the two chromophores involved [12].

### 5.2. Experimental and theoretical methods

Conformer-selective, ground state IR spectra are acquired by means of an IR-UV double-resonance technique that consists in exciting the cold ions with a tunable infrared optical parametric oscillator (OPO) 100 ns before the UV laser, thus producing depletion in the UV-induced fragmentation yield [13]. By comparing these highly resolved IR spectra with those computed for the lowest energy conformers determined by theory, we can define the distance between the chromophores and their relative orientation.

Quantum mechanical computations of the ground state are carried out with Gaussian 16 [14]. The geometry optimization and harmonic frequencies are performed at B3LYP/6-31+G(d,p) [15-17] with the D3(BJ)



dispersion correction [18]. The harmonic frequencies are scaled with a 0.953 scaling factor [11].

To measure an IR spectrum in the excited electronic state, a UV pulse first excites a selected conformer, which is probed after a certain delay ( $\geq 5$  ns) with the IR pulse. Resonant IR absorption of the electronically excited species leads to an enhancement of the photofragment signal corresponding to the tyrosine side-chain loss channel. This UV-pump/IR-probe spectroscopic scheme was previously validated on tyrosine- or phenylalanine-containing protonated peptides by Zabuga [4]. Zwiernick group applied an analogous approach based on excited-state fluorescence-dip infrared spectroscopy on neutral molecules [19, 20]. An energy level diagram and the laser sequence for ground state and excited state spectroscopy is given in Figure 5.1.

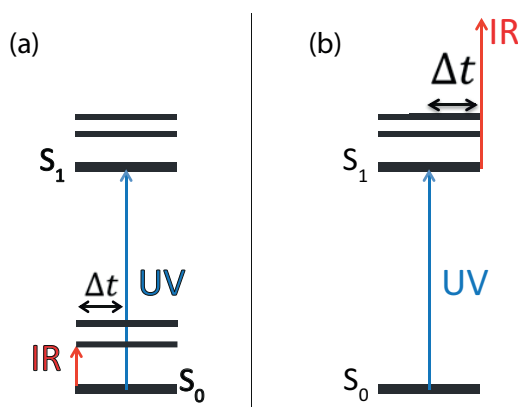


Figure 5.1. (a) IR-UV double resonance scheme for spectroscopy of the electronic ground state; (b) UV-pump/IR-probe excitation scheme for spectroscopy of the electronic excited state.

*Ab initio* excited state computations are performed with the TURBOMOLE 7.1 program suite [21] on the ground state equilibrium geometry determined with density functional theory. The excitation energies are computed with the ADC(2) (algebraic diagrammatic construction up to second order) method [22, 23] using the resolution-of-identity approximation for two-electron integrals [24] and the frozen core approximation. The def2-SVPD basis set augmented with diffuse functions is chosen for all atoms [25].

Electronic couplings are based on the TDDFT [26] (B3LYP, CAM-B3LYP [27]) and the equation-of-motion coupled-cluster method [28] (EOM-CCSD), and computed as implemented in Gaussian 16 [29, 30]. Natural transition orbital analysis is performed at the TDDFT and ADC(2) levels to determine excited state characters [31].

### 5.3. Ultraviolet photofragment spectroscopy

Upon electronic excitation of the cold AcFAYK-H<sup>+</sup> with a UV laser, a fraction of ions dissociates. Scanning the UV laser and monitoring the ion fragment signal generates an electronic action spectrum of AcFAYK-H<sup>+</sup> (Figure 5.2a, green trace).

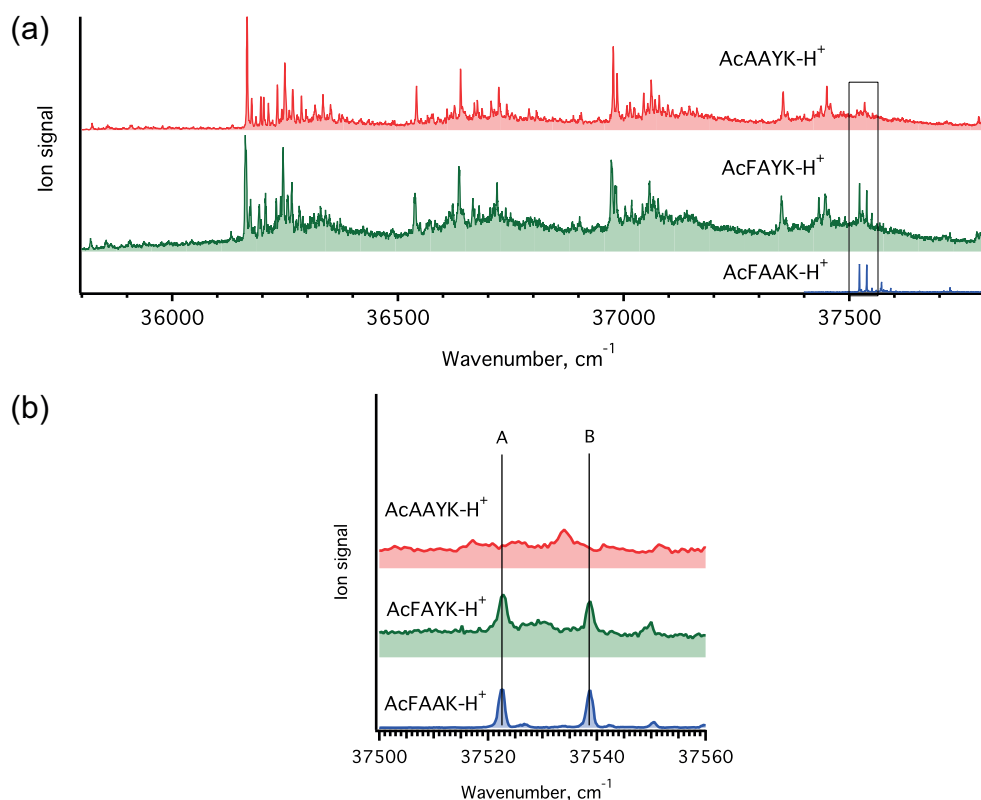


Figure 5.2. a) Electronic fragmentation spectrum of *AcAAYK-H<sup>+</sup>* (red), *AcFAYK-H<sup>+</sup>* (green) and *AcFAAK-H<sup>+</sup>* (blue); b) Blow-up of the rectangular slice. Vertical lines indicate electronic transitions of the two major conformers A and B.

Although the UV spectrum of *AcFAYK-H<sup>+</sup>* is congested due to the high Frank-Condon activity of the tyrosine chromophore [32, 33], the sharp band at 37522.8 cm<sup>-1</sup> can be assigned to the band origin of the phenylalanine chromophore absorption. In addition to being close in wavenumber to the band origin of protonated phenylalanine, this assignment is confirmed by comparison with the electronic spectrum of a peptide in which tyrosine was replaced by alanine (*AcFAAK-H<sup>+</sup>*, blue spectrum in Figure 5.2b). The nearly identical positions of the phenylalanine vibronic transitions in

AcFAYK-H<sup>+</sup> and AcFAAK-H<sup>+</sup> imply that the two peptides have similar structure, the confirmation of which is discussed below. Moreover, the UV spectrum of AcFAYK-H<sup>+</sup> resembles that of AcAAYK-H<sup>+</sup> (red trace in Figure 5.2a) to a surprisingly high degree, also implying a similar structure.

#### 5.4. Structural identification of ground state conformations

Electronic transitions at 37522.8 cm<sup>-1</sup> and 37538.8 cm<sup>-1</sup>, highlighted in Figure 5.2b, belong to the two dominant conformers of AcFAYK-H<sup>+</sup>, denoted as A and B. We measure an infrared spectrum for each peak in the phenylalanine absorption region of AcFAYK-H<sup>+</sup> by applying IR-UV double resonance, shown in Figure 5.3 along with the computed spectra and corresponding structures. The good agreement between measured and computed spectra allow us to assign the structures of the two conformers.

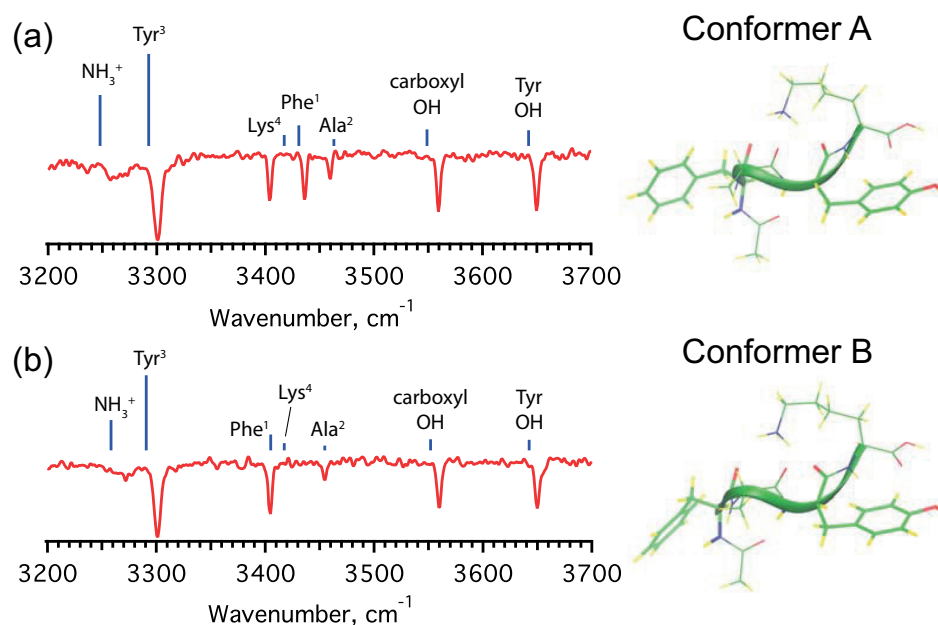


*Figure 5.3. Measured IR spectra of the conformers of AcFAYK-H<sup>+</sup> that exhibit electronic transitions at: a) 37522.8 cm<sup>-1</sup> (conformer A); and b) 37538.8 cm<sup>-1</sup> (conformer B) along with the theoretical IR spectra (blue lines) and the corresponding calculated structure. Assignments of the lines are made based on the computed vibrational spectra.*

Analysis of the structures shows that the only difference between conformers A and B consists in a 120° rotation of the Phe side chain around the C<sub>α</sub>-C<sub>β</sub> bond (Figure 5.4). In conformer B, this difference allows the Phe<sup>1</sup> amide NH to form a favorable π-hydrogen bond with the benzene ring, and this interaction shifts one band from 3436 cm<sup>-1</sup> to 3404 cm<sup>-1</sup>. The presence of two conformers that differ only by the phenylalanine side chain flip is a common property of 3<sub>10</sub> helices with phenylalanine at the N-terminus [10, 34, 35]. It is essential to stress that the distance between the chromophores remains virtually the same (11.7 and 11.3 Å for conformers A and B, respectively); only the relative orientation of the chromophores changes substantially.

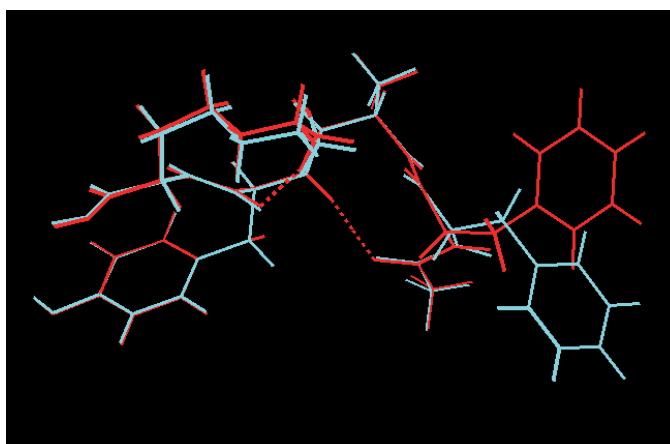
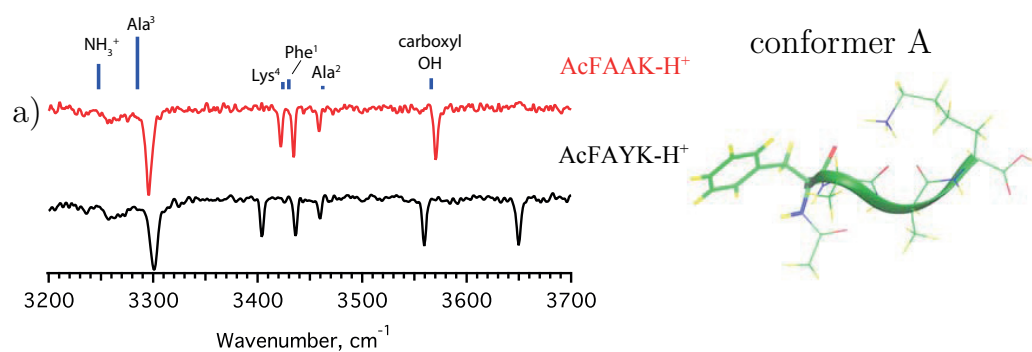


Figure 5.4. Conformers A (red) overlapped with conformer B (blue). The difference between the two conformers consists in a  $120^\circ$  rotation of the Phe side chain around  $C\alpha-C\beta$  bond.

Comparison of the AcFAYK- $H^+$  IR spectra with those of the monochromophoric peptides reveals similar features arising from the same hydrogen-bonding pattern of a  $3_{10}$  helix – the difference is exclusively due to a weak perturbation of the NH and OH groups in the vicinity of phenylalanine or tyrosine chromophores (Figure 5.5). In AcFAAK- $H^+$  the carboxyl OH group is free and it appears at  $3570\text{ cm}^{-1}$ ; the interaction of the tyrosine aromatic ring with the carboxyl OH red-shifts its frequency to  $3558\text{ cm}^{-1}$  in AcFAYK- $H^+$ . We can conclude that the presence of the tyrosine chromophore induces a small perturbation to the oscillator frequencies of AcFAAK- $H^+$ .



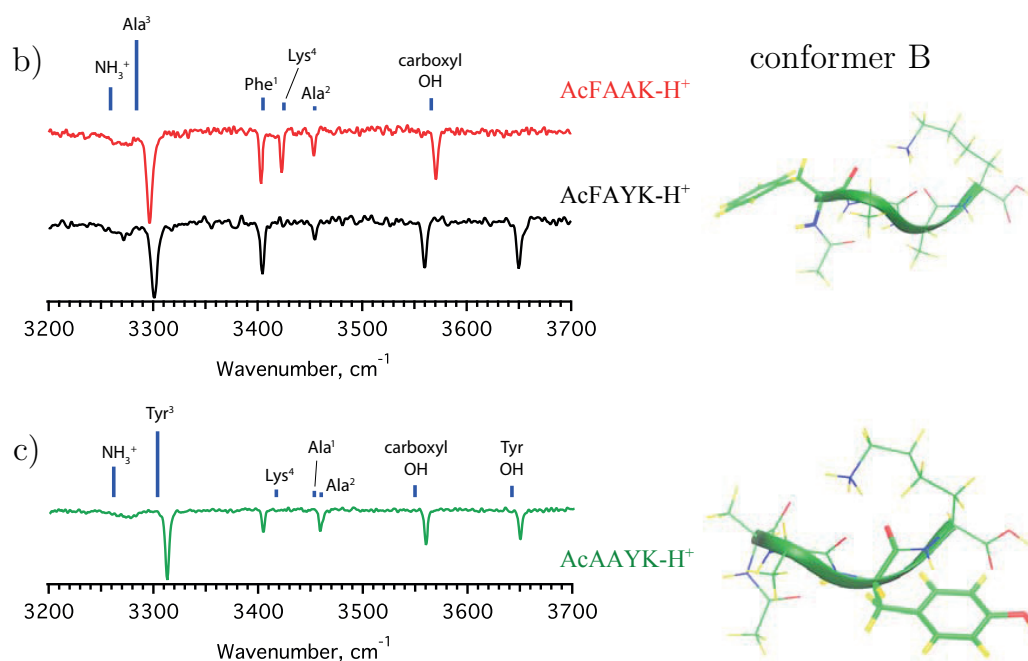


Figure 5.5. The experimental (red) and calculated (blue) IR spectra of conformer A (a) and conformer B (b) of AcFAAK-H<sup>+</sup> compared with the experimental IR spectra of the corresponding conformers of AcFAYK-H<sup>+</sup> (black). The optimized structures of conformer A (a) and conformer B (b) of AcFAAK-H<sup>+</sup> are based on the comparison with the computed IR spectrum (in blue). The UV laser is fixed at 37522.8 cm<sup>-1</sup> (conformer A) and 37538.8 cm<sup>-1</sup> (conformer B). (c) The experimental (green) and calculated (blue) IR spectra of AcAAYK-H<sup>+</sup>. The UV laser is fixed at 36166 cm<sup>-1</sup>.

### 5.5. IR spectroscopy of excited states

Excited state infrared spectra are measured by fixing the UV laser to a strong transition of either the tyrosine chromophore at 36193 cm<sup>-1</sup> or of the phenylalanine chromophore at 37522.8 cm<sup>-1</sup> related to conformer A and scanning the IR frequency. Because the tyrosine absorption spectrum

changes smoothly under the phenylalanine peaks (see Figure 5.2), we can correct for the tyrosine absorption under the sharp phenylalanine bands by subtracting from the gain spectra acquired on the peak of the phenylalanine chromophore transition ( $37522.8\text{ cm}^{-1}$ ) the signal that occurs when the laser is set at the wavenumber just next to it ( $37525.6\text{ cm}^{-1}$ ) [33]. As a result, we obtained a spectrum that corresponds to the species in which the phenylalanine chromophore is exclusively excited (Figure 5.6).

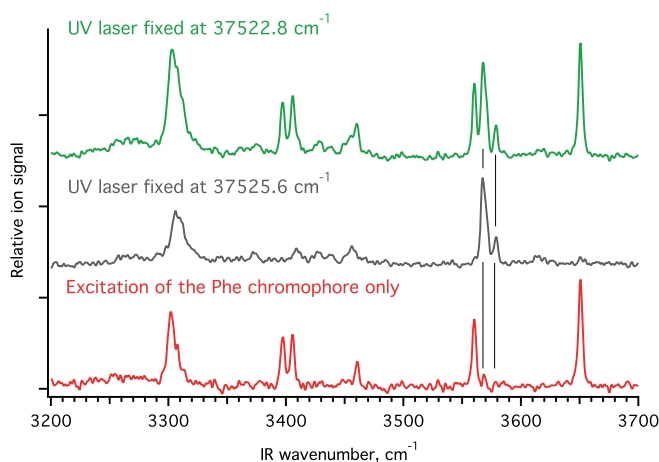


Figure 5.6. Green: excited state IR spectrum of AcFA YK- $H^+$  obtained fixing the UV laser at the phenylalanine chromophore excitation line of conformer A,  $37522.8\text{ cm}^{-1}$ . Gray: UV laser fixed at  $37525.6\text{ cm}^{-1}$ . Red: excited state IR spectrum after correction for the Tyr chromophore absorption. The transitions corresponding to tyrosine chromophore are marked with vertical lines.

The excited-state vibrational spectra (Figure 5.7a, shown in red) are recorded at the shortest ( $\sim 5\text{ ns}$ ) delay between the UV pump and IR probe lasers.



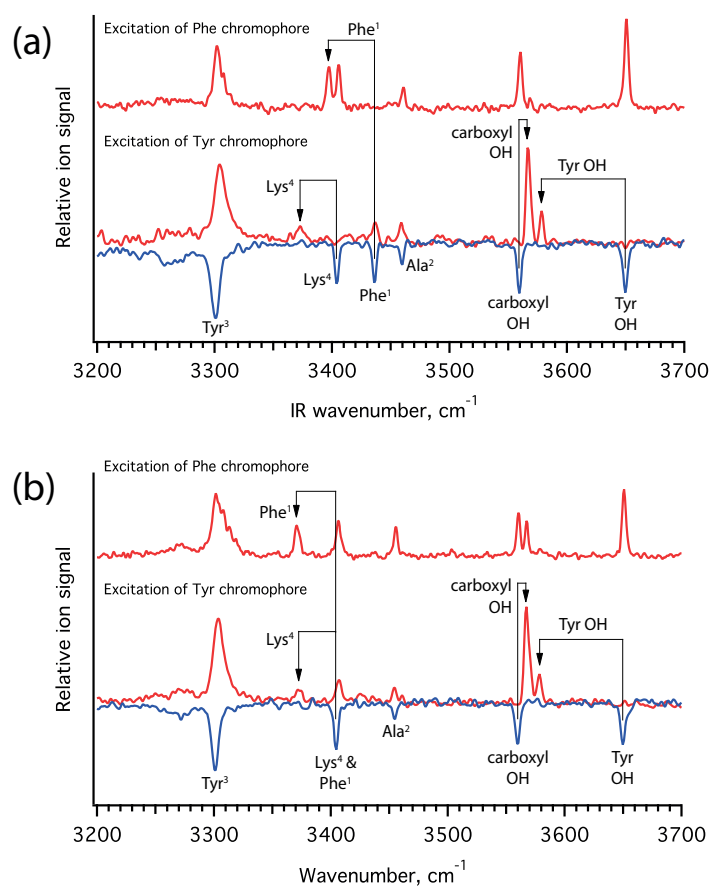
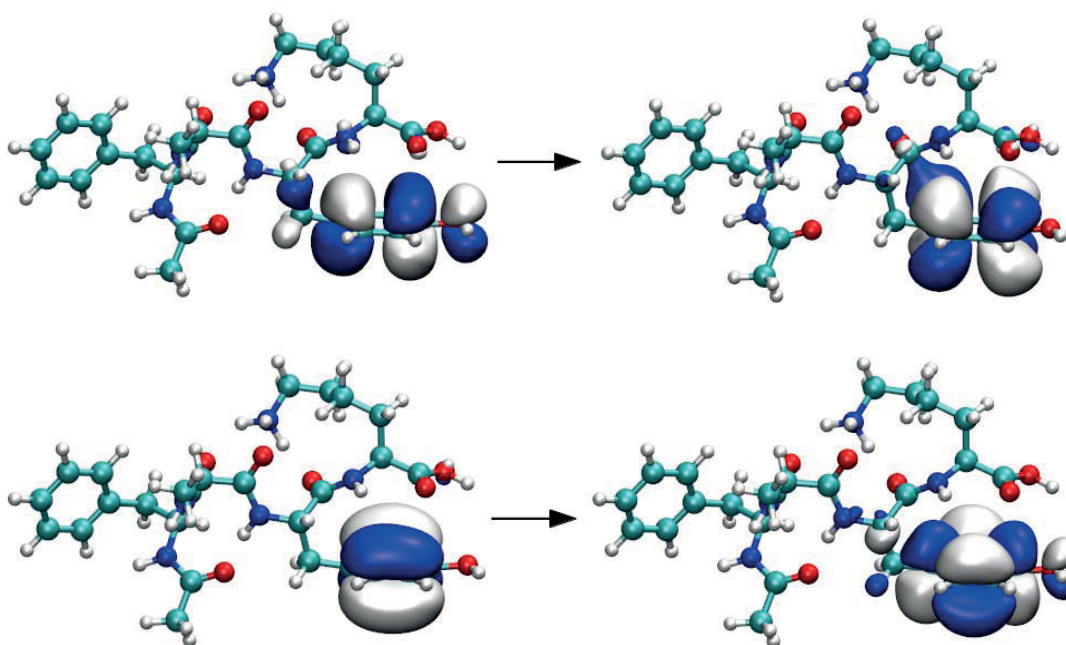


Figure 5.7. a) IR spectra of the excited states of conformer A (red) with the electronic excitation localized in the phenylalanine and tyrosine chromophores compared with the ground state (blue). The UV laser is fixed at  $37522.8\text{ cm}^{-1}$  and  $36193\text{ cm}^{-1}$  for pumping the phenylalanine and tyrosine chromophore respectively. b) For conformer B the phenylalanine and tyrosine chromophore transitions occur at  $37538.8\text{ cm}^{-1}$  and  $36197\text{ cm}^{-1}$  respectively.

The excited state vibrational spectra are similar to the corresponding ground state spectra, as only certain bands undergo a noticeable shift relative to their frequency in the ground state. The infrared spectrum of conformer A in the excited electronic state is different depending on which

chromophore is excited. The peak assignments of the ground state IR spectrum allow us to determine which NH and OH groups experience a frequency shift in the excited state. Thus, excitation of the phenylalanine chromophore shifts only the Phe<sup>1</sup> NH line by 39 cm<sup>-1</sup> from its ground state frequency. This indicates that the electronic energy is localized on the phenylalanine chromophore and not on the tyrosine. Excitation of the tyrosine chromophore results in shifts of other bands: the tyrosine OH appears redshifted by 71 cm<sup>-1</sup> (similar to the 76 cm<sup>-1</sup> redshift of OH upon S<sub>0</sub>-S<sub>1</sub> excitation of phenol [36]); the carboxyl OH is blue-shifted by 7 cm<sup>-1</sup>; and the Lys<sup>4</sup> NH band is redshifted by 32 cm<sup>-1</sup>. These groups are in close proximity to the tyrosine chromophore, suggesting that the perturbation of the electronic structure in this state is localized. Analogous changes in the IR spectra of conformer B occur upon electronic excitation (Figure 5.7b). Quantum chemical computations for AcFAYK-H<sup>+</sup> (Figure 5.8) show that the first and second excitations correspond to L<sub>b</sub> type transitions [37] of the tyrosine and phenylalanine chromophore respectively. The localized character of the excitations explains why the groups close to the chromophore experience the aforementioned shift in frequency. Moreover, the excited state spectra are sharp, indicating that the ions in these states are vibrationally cold [4]. On this basis we assign the IR spectra to singlet excited states of the tyrosine or phenylalanine chromophores.

$S_1$  transition (Tyr  $L_b$ ), 4.802 eV,  $f=0.0181$



$S_2$  transition (Phe  $L_b$ ), 5.162 eV,  $f=0.00017$

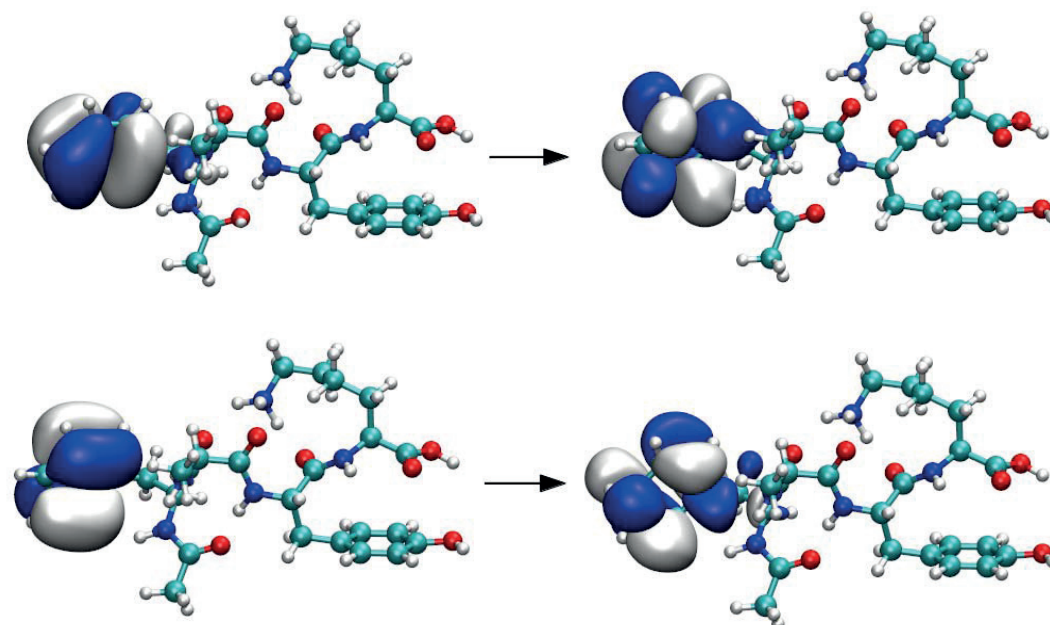


*Figure 5.8. Natural transition orbitals (NTOs) of the first two excitations in conformer A of AcFAYK-H<sup>+</sup>; the excitation energies and corresponding NTOs are computed with the ADC(2)/def2-SVPD method; isosurface connects the points with the wavefunction value = 0.02.*

## 5.6. Transient spectroscopy

The time evolution of the system in the excited state can be monitored by increasing the delay between UV-pump and IR-probe pulses, which produces changes in the IR spectrum, as shown in Figure 5.9. Emergence of lines corresponding to the singlet excited state of tyrosine upon excitation of phenylalanine indicates that electronic energy migrates between these chromophores. At longer delays, features of a new state appear (see Figure 5.10). The broadening of the IR bands indicates that a significant part of the initial excitation is converted into vibrational energy.

In this way, time-resolved IR spectroscopy reveals the fate of the electronic excitation. The excitation energy is initially deposited in the phenylalanine chromophore in its first singlet excited state. It then undergoes a nearly complete, non-radiative, singlet-singlet electronic energy transfer to the tyrosine chromophore, with the transfer rate being conformer-dependent. Finally, the peptide converts into a hot, long-lived state, from which the tyrosine side-chain loss occurs [4].

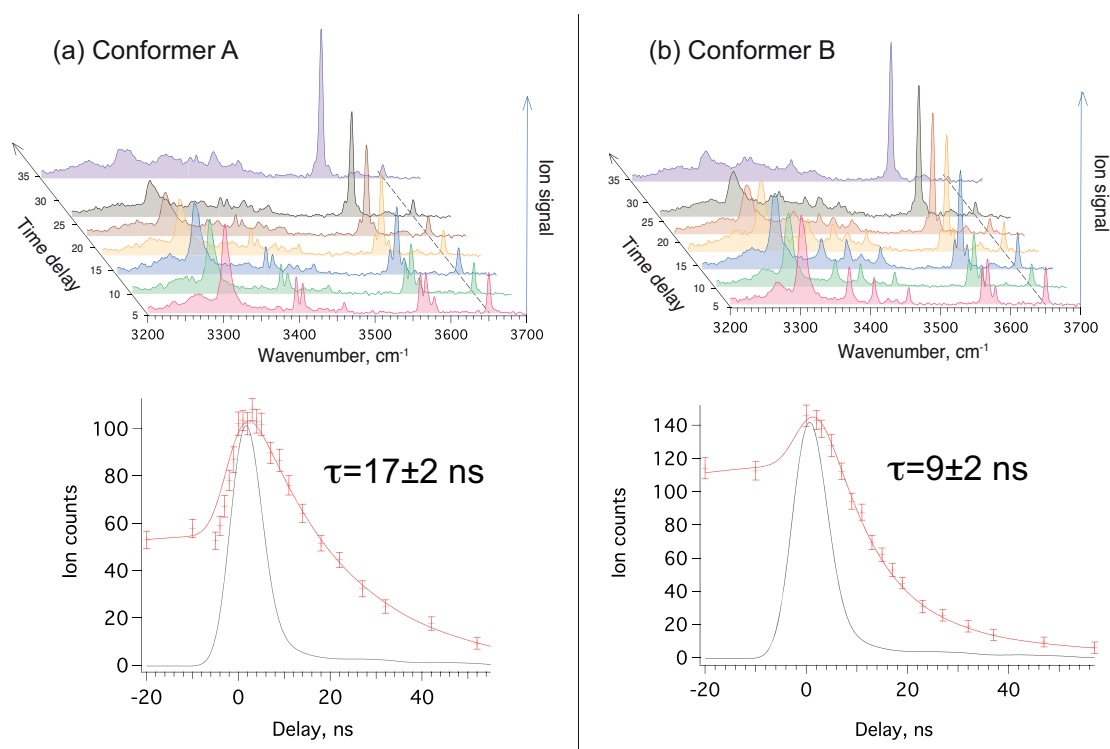
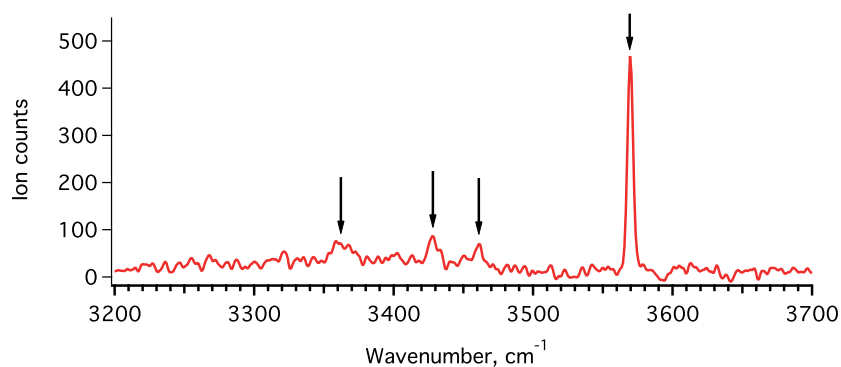


Figure 5.9. Transient signal (dots with error bars) of the singlet excited state of the phenylalanine chromophore a) in conformer A and b) in conformer B. The cross correlation of the two laser pulses is depicted in grey, and the solid red lines are convolutions of the cross-correlation signal with theoretical decays.



*Figure 5.10. The IR spectrum of the long-lived excited state. IR fires 100 ns after UV excitation of the tyrosine chromophore ( $36193\text{ cm}^{-1}$ ). The arrows indicate the distinct absorption bands that belong to the IR spectrum of this state.*

We select a band in the IR spectrum of the singlet excited state of phenylalanine at  $3650\text{ cm}^{-1}$ , which does not overlap with any vibrational transitions of the other excited states, to track its lifetime. The singlet excited state lifetime of the phenylalanine chromophore in conformer A is  $17\pm 2\text{ ns}$  (Figure 5.9a), while that of conformer B is  $9\pm 2\text{ ns}$  (Figure 5.9b).

It is illuminating to compare these values to the lifetime of phenylalanine  $S_1$  state in a peptide lacking tyrosine. A test experiment done on AcFAAK- $H^+$  has shown that the phenylalanine chromophore exhibits an  $S_1$  decay constant of  $83\pm 3\text{ ns}$  for conformer A and  $88\pm 5\text{ ns}$  for conformer B (see Figure 5.11). This is consistent with results obtained on the other Phe containing peptides [4].

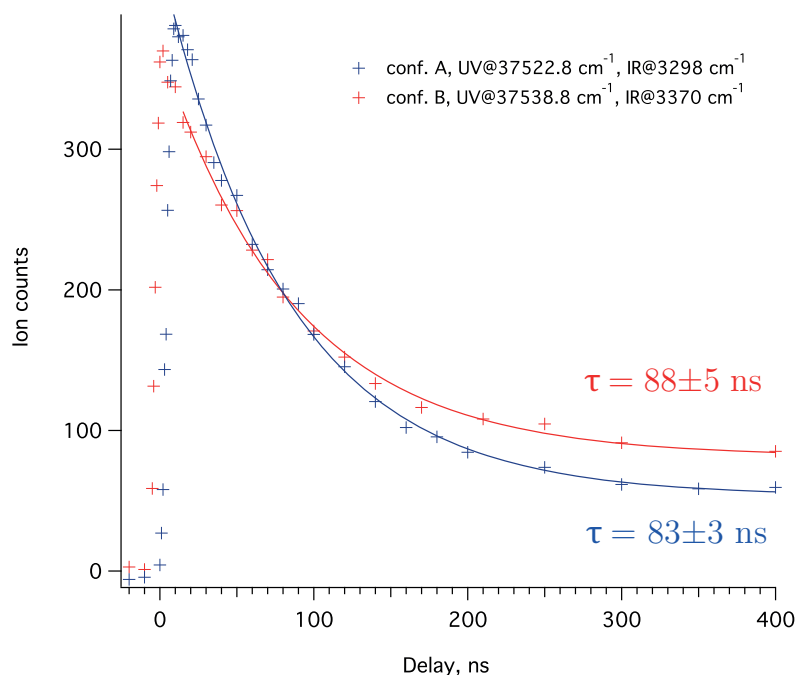


Figure 5.11. Decay of  $S_1$  state of the phenylalanine chromophore in  $AcFAAK-H^+$ . The decay constants for conformer A and conformer B are given in blue and red, respectively.

Assuming that the change in lifetime of the singlet excited state of the phenylalanine in the bichromophoric peptide is exclusively due to energy transfer to the acceptor chromophore, we can derive the rate of energy transfer in the following way:

$$k_{\text{transfer}} = \frac{1}{\tau_{AcFAAK-H^+}} - \frac{1}{\tau_{AcFAYK-H^+}},$$

hence  $k_{\text{transfer}}(\text{conf. A}) = (4.7 \pm 0.7) \cdot 10^7 \text{ s}^{-1}$  and  $k_{\text{transfer}}(\text{conf. B}) = (10 \pm 2) \cdot 10^7 \text{ s}^{-1}$ . Thus, the experiment provides the ratio of the energy transfer rates in the two conformers:  $k_B/k_A = 2.1 \pm 0.7$ . With this value, we test the performance of two theoretical models for energy transfer.

## 5.7. Models for electronic energy transfer

Dr. Antonio Prlj from the Laboratory for Computational Molecular Design carried out all the computations of electronic couplings. A short overview of theoretical methods for electronic couplings follows in this section.

The energy transfer rate in the weak-coupling regime can be described by the Fermi golden rule:

$$k_{transfer} = \frac{2\pi}{\hbar} |V|^2 J \quad (5.1)$$

where  $V$  is the electronic coupling between the excited states of the donor and acceptor, and  $J$  is the spectral overlap of the donor emission and acceptor absorption.

According to Förster theory, the electronic coupling  $V$  can be approximated with a dipole-dipole interaction between transition dipole moments (TDMs) of the donor and acceptor chromophores [38]. The expression for the rate of electronic energy transfer becomes:

$$k_{transfer} = \left( \frac{9000 \ln 10}{128 \pi^5 N n^4} \right) \frac{Q_D \kappa^2 J}{\tau_D r^6} \quad (5.2)$$

where  $Q_D$  and  $\tau_D$  are the quantum yield and lifetime of the donor in the absence of acceptor, respectively,  $n$  is the refraction index of the medium,  $J$  is the aforementioned spectral overlap,  $r$  is the interchromophore distance and  $\kappa^2$  is the orientation factor. The orientation factor is given by the expression [39]:



$$\kappa^2 = (\cos\theta_T - 3\cos\theta_d\cos\theta_a)^2 \quad (5.3)$$

where  $\theta_T$  is the angle between the TDM of the donor and TDM of the acceptor, and  $\theta_d$  and  $\theta_a$  are angles between a vector that connects the chromophores and TDMs of the donor and acceptor, respectively.

Instead of a simplified model of dipole-dipole interaction, the total coupling can be expressed as the Coulomb interaction between 3D transition densities. Apart from including higher order terms in the multipole expansion, this quantum-mechanical approach accounts for electronic exchange and correlation effects and orbital overlap contributions [40]:

$$\begin{aligned} V = & \int \rho_D^{tr*}(r) \frac{1}{|r-r'|} \rho_A^{tr}(r') dr dr' + \int \rho_D^{tr*}(r) g_{xc}(r, r') \rho_A^{tr}(r') dr dr' - \\ & - \omega_0 \int \rho_D^{tr}(r) \rho_A^{tr}(r) dr \end{aligned} \quad (5.4)$$

where  $g_{xc}$  is the exchange and correlation kernel,  $\rho^{tr}$  is the transition density, and  $\omega_0$  is the average resonance transition energy of the dyad. The transition density is computed for two subsystems containing the donor and acceptor chromophores. The influence of the linker can also be taken into account [41].

Assuming that the spectral overlap is identical in the two conformers, the ratio of energy transfer rates can be expressed by:

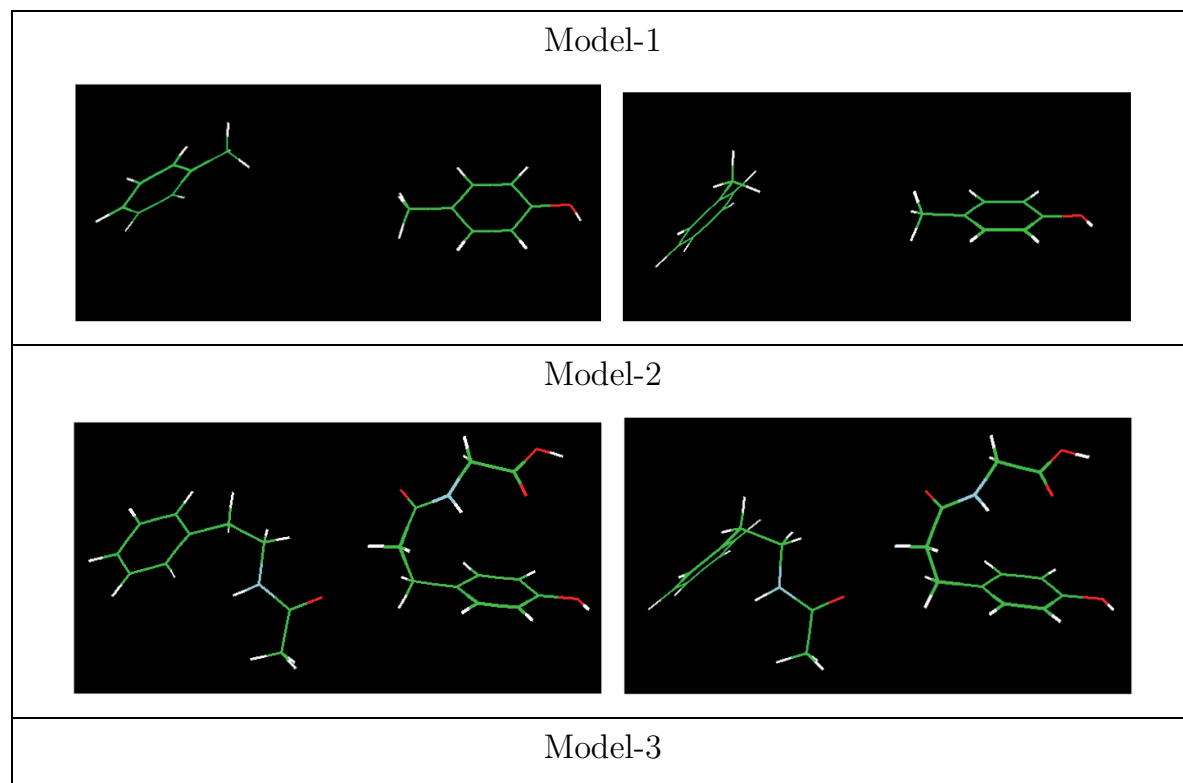
$$\frac{k_{conformer B}}{k_{conformer A}} = \frac{|V_B|^2}{|V_A|^2} \quad (5.5)$$

Considering also the fluorescence yield of the donor chromophore  $Q_D$  identical for both conformers, Equation 5.2 transforms into:

$$\frac{k_{conformer B}}{k_{conformer A}} = \frac{\kappa_B^2 r_A^6}{\kappa_A^2 r_B^6} \quad (5.6)$$

## 5.8. Computational results

The couplings are computed for three different truncated chromophores (fragmentation models): model-1 corresponds to the minimal chromophore structure, model-2 includes the local environment (i.e. part of the backbone) and model-3 includes the largest portion of the backbone (Figure 5.12). The truncation is done on the ground state structures because the geometry optimization in the excited state of the phenylalanine (donor) chromophore leads to unsubstantial changes of the ground state conformation. Both transition dipole moments and electronic couplings are computed with TDDFT [42] and wavefunction-based EOM-CCSD [28].



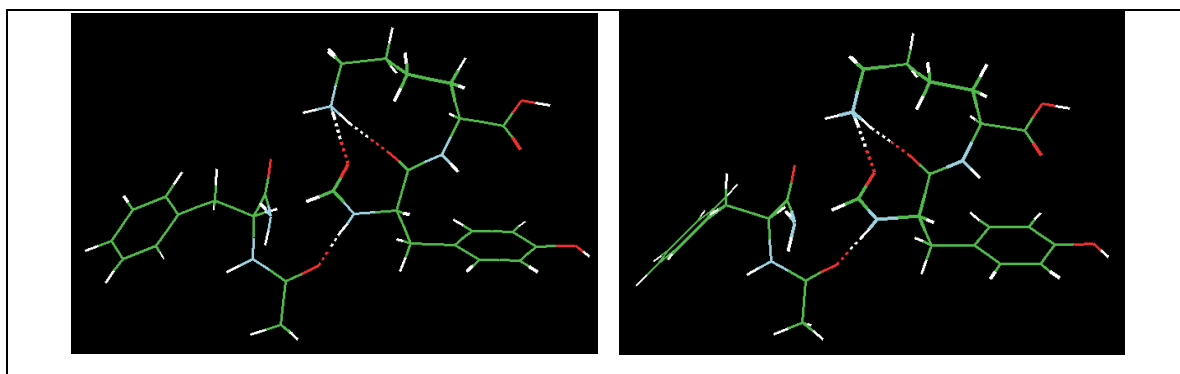
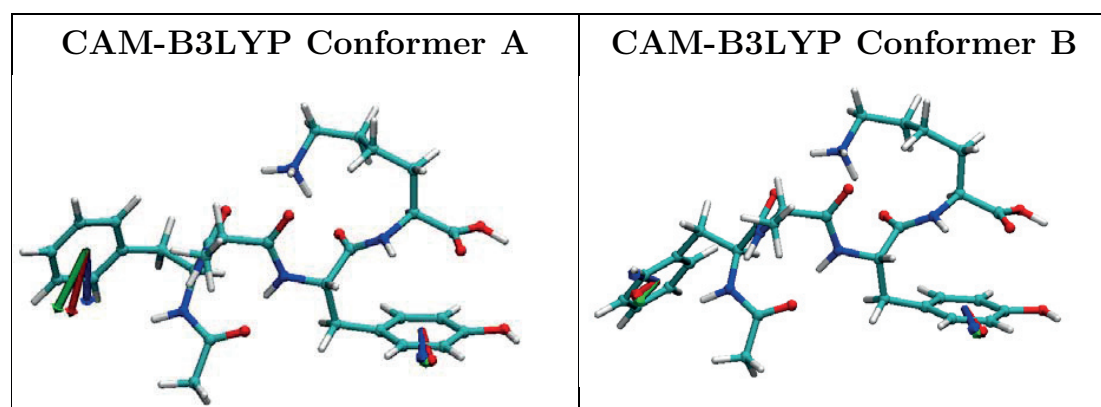


Figure 5.12. The two chromophores are isolated in two different systems, between which the coupling is computed. Left: conformer A. Right: conformer B.

The results from the dipole-dipole approximation vary widely depending upon the fragmentation model and the electronic structure method employed. A tentative explanation for this effect is the high polarizability of phenylalanine chromophore that leads to a high sensitivity of its TDM to the local environment variation (Figure 5.13). Also, higher order multipoles become significant due to the short distance between chromophores ( $\sim 12$  Å). These results are in line with previous work, outlining the deficiencies of the dipole approximation [43, 44].



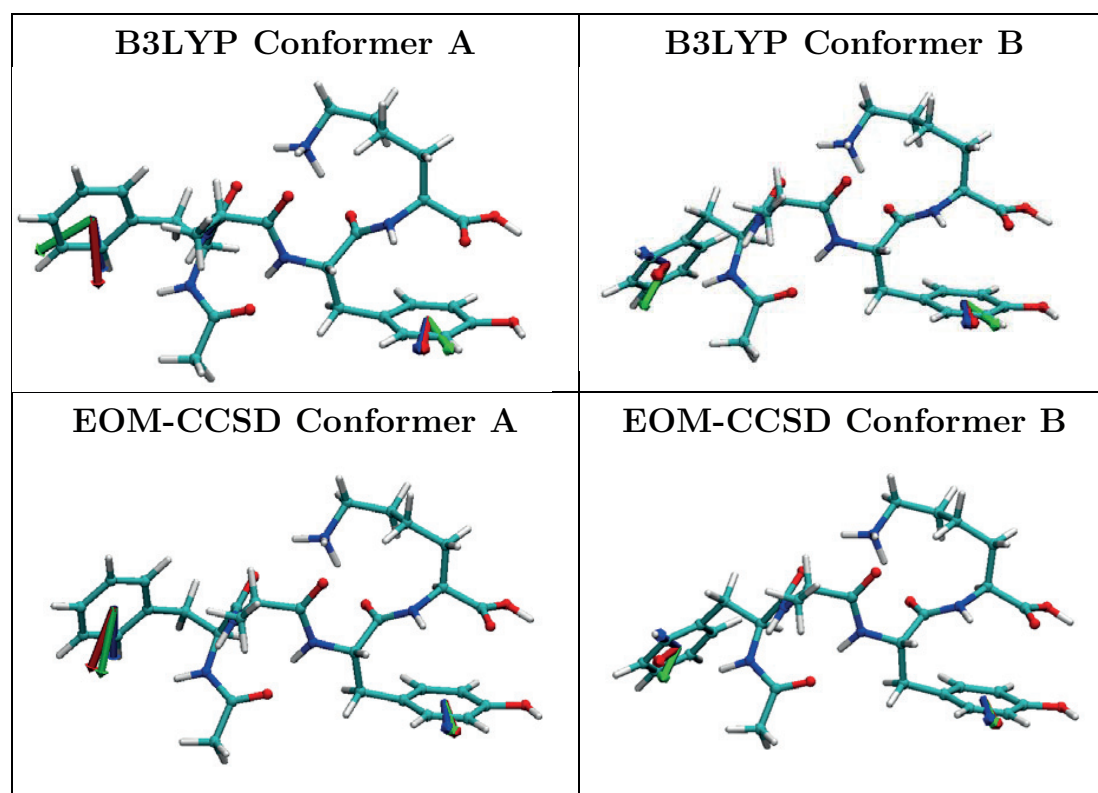


Figure 5.13. TDMs for the three models: blue = small cut (model1), red = middle cut (model2), green = large cut (model3). All vectors are normalized and multiplied by 2.5 for comparison reasons.

Computing the coupling based on transition densities reveals that the total electronic coupling values are strongly dominated by Coulomb contributions, with the exchange and orbital overlap effects being negligible (Tables 5.1-5.3). For the intermediate and large fragmentation models (model-2 and model-3), the TDDFT results (computed with two common density functional approximations: B3LYP [16, 17] and CAM-B3LYP [27]) deviate strongly from the experimental results, whereas EOM-CCSD is consistent with the experiment (Figure 5.14). The large size of the

chromophore subsystems in model-3 limited the affordable basis set to 6-31G(d,p) for EOM-CCSD computations.

Table 5.1. Couplings computed on the B3LYP-D3(BJ)/6-31+G(d,p) geometry. (\*) 6-31G(d,p) basis set.

	Method	Coupling in conformer A ( $V_A$ )	A: excitation energies, eV (oscillator strengths)	Coupling in conformer B ( $V_B$ )	B: excitation energies, eV (oscillator strengths)	$ V_B ^2/ V_A ^2$	Ratio with dipole approx
Model 1	B3LYP	-0.00007943	A:4.87(0.0360) D:5.26(0.0019)	0.000126425	A:4.87(0.036) D:5.26(0.0022)	2.533	3.67
	CAM-B3LYP	0.000078786	A:5.02(0.0394) D:5.37(0.0012)	0.000159561	A:5.02(0.0395) D:5.38(0.0026)	4.102	5.6
	EOM-CCSD	-0.000040725	A:4.87(0.0245) D:5.11(0.0008)	0.000069638	A:4.87(0.0246) D:5.11(0.0009)	2.924	3.72
Model 2	B3LYP	-0.000088977	A:4.78(0.0104) D:5.23(0.0026)	0.000009672	A:4.78(0.0105) D:5.25(0.002)	0.012	8.77
	CAM-B3LYP	-0.000001803	A:5.05(0.0237) D:5.38(0.0017)	0.000051555	A:5.05(0.0246) D:5.38(0.0014)	817.6	425.4
	EOM-CCSD	0.000008717	A:4.89(0.0142) D:5.11(0.0005)	0.000012888	A:4.89(0.0146) D:5.12(0.0004)	2.186	55.4
Model 3	B3LYP	0.000199714	A:4.89(0.01) D:5.22(0.003)	0.000074815	A:4.88(0.0099) D:5.24(0.0009)	0.140	0.61
	CAM-B3LYP	0.000014324	A:5.05(0.0179) D:5.38(0.0012)	-0.000011056	A:5.04(0.0183) D:5.38(0.0012)	0.596	16.1
	EOM-CCSD*	0.000009664	A:5.01(0.0125) D:5.19(0.0006)	0.000017572	A:5.01(0.0129) D:5.20(0.0004)	3.306	75.1

Table 5.2. Coupling energy components for conformer A.

	Method	Total coupling for conformer A	Coulomb	Exch.	Exch.-Corr.	w-avg*overlap
Model 1	B3LYP	-0.00007943	-0.000079351	-0.000000022	-0.000000057	0
	CAM-B3LYP	0.000078786	0.000078669	0.000000056	0.000000062	0
	EOM-CCSD	-0.000040725	-0.000040674	-0.000000052	-	0
Model 2	B3LYP	-0.000088977	-0.000091863	0.000001199	0.000001717	-0.000000029
	CAM-B3LYP	-0.000001803	-0.0000002	-0.000001103	-0.000000517	0.000000018
	EOM-CCSD	0.000008717	0.000010547	-0.000001845	-	0.000000014
Model 3	B3LYP	0.000199714	0.000209335	-0.000004545	-0.000005259	0.000000182
	CAM-B3LYP	0.000014324	0.000015805	-0.000001382	-0.000000092	-0.000000007
	EOM-CCSD*	0.000009664	0.000009131	0.000000539	-	-0.000000006

Table 5.3. Coupling energy components for conformer B.

		Total coupling for conformer B	Coulomb	Exch.	Exch.-Corr.	w- avg*overlap
Model 1	B3LYP	0.000126425	0.000126125	-0.000000021	0.00000032	0
	CAM-B3LYP	0.000159561	0.000159532	-0.000000039	0.000000068	0
	EOM-CCSD	0.000069638	0.000069659	-0.000000022	-	0
Model 2	B3LYP	0.000009672	0.000006408	0.000001034	0.000002276	-0.000000047
	CAM-B3LYP	0.000051555	0.000055955	-0.000002757	-0.000001692	0.000000049
	EOM-CCSD	0.000012888	0.000015561	-0.000002695	-	0.000000022
Model 3	B3LYP	0.000074815	0.000087433	-0.000006257	-0.000006785	0.000000423
	CAM-B3LYP	-0.000011056	-0.000014362	0.000002184	0.000001162	-0.00000004
	EOM-CCSD*	0.000017572	0.000018562	-0.000001003	-	0.000000013

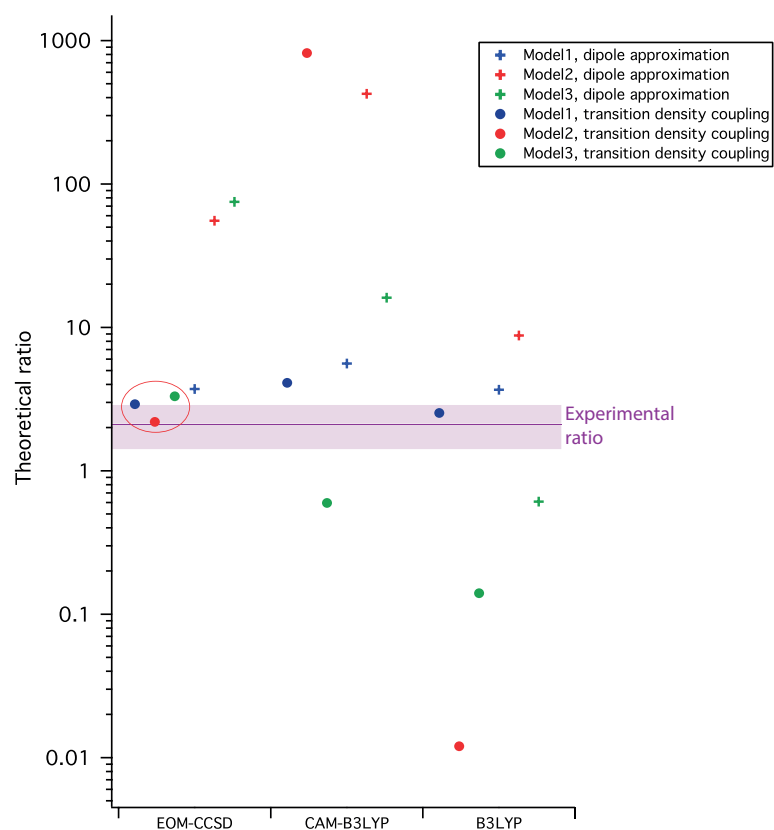
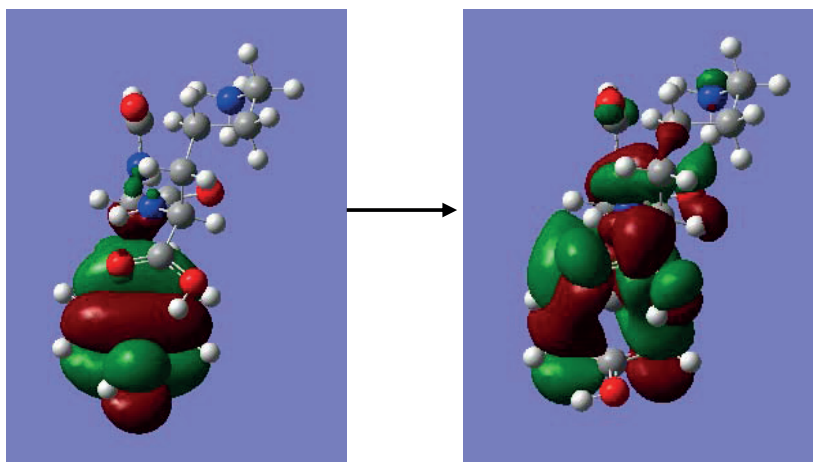


Figure 5.14. Ratio of electronic energy transfer rates ( $k_B/k_A$ ) predicted based on the dipole-dipole approximation and coupling of transition densities. The red oval highlights the transition density coupling computed

with EOM-CCSD, which is in agreement with experiment for all cutting models. Notice the logarithmic vertical scale.

Excited-state character analysis (Figure 5.15) reveals that instead of the fairly localized nature of the  $L_b$  excitations predicted by wavefunction-based methods, the TDDFT excitations tend to spuriously delocalize from the chromophore towards the peptide backbone. This is the reason for the unbalanced description of the electronic couplings in the two chromophores. Furthermore, while the correlated wavefunction-based methods predict the two  $L_b$  excited states as the lowest in energy, in TDDFT they do not necessarily coincide with the  $S_1$  and  $S_2$  states. Instead, they are embedded in the manifold of low-energy states, which increases the possibility of character mixing with the nearly degenerate excited states. The poor performance of TDDFT may be traced back to the lack of differential correlation effects, which are highly important for the description of  $L_b$  states [45].



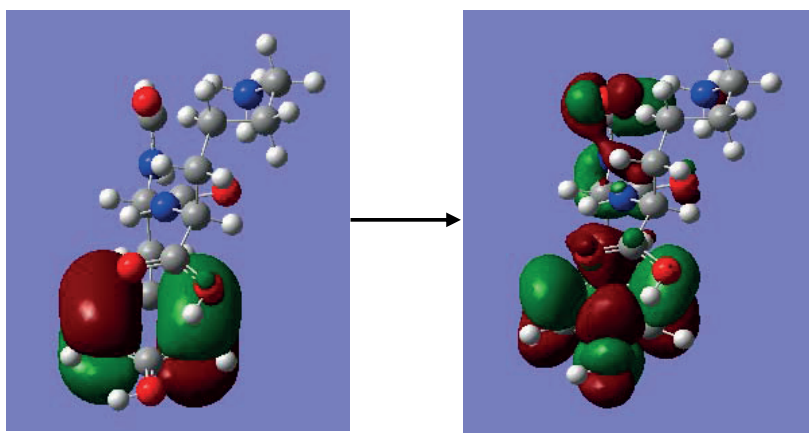


Figure 5.15. NTOs of  $L_b$  state of tyrosine computed for model-3 of conformer A with B3LYP/6-31+G(d,p) show a false delocalization of electron density from the chromophore towards the peptide backbone. Isosurface connects the points with the wavefunction value = 0.02.

### 5.9. Fragmentation from the UV laser

We measured the power dependence of side chain loss channels specific and the  $b_2$  fragmentation channels (Figure 5.16).

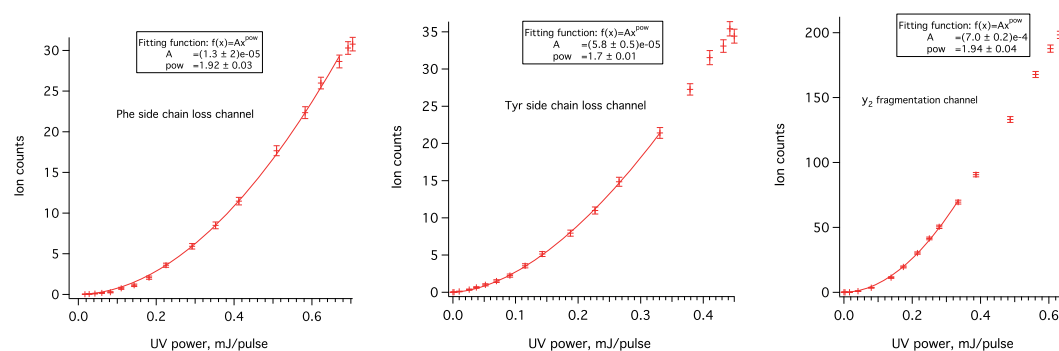


Figure 5.16. Power dependence of the UV-induced fragmentation.



The splines strongly suggest that phenylalanine and tyrosine side chain loss channels, as well as the  $b_2$  channel, are due to absorption of two photons. Jockusch *et al.* have recently shown how fragmentation of large ions can occur from multiple-photon absorption, using rhodamine as an example [46]. We conclude that in the case of AcFAYK- $H^+$ , multiphoton fragmentation from UV laser is inherently biased and does not reflect the energy transfer measured in the pump-probe experiments. However, this observation does not undermine the pump-probe scheme, since the ions that previously absorbed one photon of UV do not fragment, unless they absorb also an IR photon.

#### 5.10. Summary

Our experiment provides a new way of monitoring the electronic energy transfer and the subsequent photochemical processes. The low temperature in our ion trap allows the measurement of conformer-specific infrared spectra of AcFAYK- $H^+$ . The relative orientation of the chromophores varies in the two conformers, while the distance between the chromophores does not change significantly. Comparing the IR spectrum of AcFAYK- $H^+$  with those of the two monochromophoric peptides (AcFA<sub>2</sub>K- $H^+$  and AcA<sub>2</sub>YK- $H^+$ ) reveals that only the NH and OH groups that are in the vicinity of the chromophores shift upon electronic excitation, confirming the peak assignments of the vibrational spectrum of the bichromophoric species. The UV-pump/IR-probe scheme reveals the energy transfer processes that take place in real time after UV excitation of the

phenylalanine or tyrosine chromophores in AcFAYK-H<sup>+</sup>. The measured singlet-singlet energy transfer rates vary by a factor of 2 for two different conformers. Carrying out the experiment in a cold ion trap narrows down the uncertainty caused by solvation and thermal vibrations, and serves as a benchmark for determining the performance of the dipole-dipole approximation of the FRET model as well as that based on the coupling of transition densities [40]. The dipole-dipole Förster approximation is insufficient for the system of interest, because of the short distance between the chromophores. As for the quantum mechanical approach, couplings computed with EOM-CCSD are consistent with the experimental results, while those calculated with TDDFT using the B3LYP and CAM-B3LYP functionals are not. Dexter exchange of energy transfer is insignificant, given that the exchange and the orbital overlap contribution to the total coupling are negligible.

Implementing picosecond lasers in the proposed cryogenic UV-pump/IR-probe technique could reveal complex dynamics in a range of important biomolecular systems, relevant for the action of photoactivated enzymes.

References:

1. Rizzo, T.R., J.A. Stearns and O.V. Boyarkin, *Spectroscopic Studies of Cold, Gas-Phase Biomolecular Ions*. Int. Rev. Phys. Chem., 2009. **28**(3): p. 481-515.
2. Mališ, M., Y. Loquais, E. Gloaguen, H.S. Biswal, F. Piuzzi, B. Tardivel, V. Brenner, M. Broquier, C. Jouvét, M. Mons, N. Došlić and I. Ljubić, *Unraveling the Mechanisms of Nonradiative Deactivation in Model Peptides Following Photoexcitation of a Phenylalanine Residue*. J. Am. Chem. Soc., 2012. **134**(50): p. 20340-20351.
3. Hashimoto, T., Y. Takasu, Y. Yamada and T. Ebata, *Anomalous Conformer Dependent S<sub>1</sub> Lifetime of l-Phenylalanine*. Chem. Phys. Lett., 2006. **421**(1-3): p. 227-231.
4. Zabuga, A.V., M.Z. Kamrath, O.V. Boyarkin and T.R. Rizzo, *Fragmentation Mechanism of UV-excited Peptides in the Gas Phase*. J. Chem. Phys., 2014. **141**(15): p. 154309.
5. Loquais, Y., E. Gloaguen, M. Alauddin, V. Brenner, B. Tardivel and M. Mons, *On the Near UV Photophysics of a Phenylalanine Residue: Conformation-Dependent  $\pi\pi^*$  State Deactivation Revealed by Laser Spectroscopy of Isolated Neutral Dipeptides*. PCCP, 2014. **16**(40): p. 22192-22200.
6. Féraud, G., M. Broquier, C. Dedonder, C. Jouvét, G. Grégoire and S. Soorkia, *Excited State Dynamics of Protonated Phenylalanine and*

- Tyrosine: Photo-Induced Reactions Following Electronic Excitation.* J. Phys. Chem. A, 2015. **119**(23): p. 5914-5924.
7. Soorkia, S., M. Broquier and G. Grégoire, *Conformer- and Mode-Specific Excited State Lifetimes of Cold Protonated Tyrosine Ions.* J. Phys. Chem. Lett., 2014. **5**(24): p. 4349-4355.
  8. Malis, M., Y. Loquais, E. Gloaguen, C. Jouvét, V. Brenner, M. Mons, I. Ljubic and N. Doslic, *Non-Radiative Relaxation of UV Photoexcited Phenylalanine Residues: Probing the Role of Conical Intersections by Chemical Substitution.* Phys. Chem. Chem. Phys., 2014. **16**(6): p. 2285-2288.
  9. Hudgins, R.R., M.A. Ratner and M.F. Jarrold, *Design of Helices That Are Stable in Vacuo.* J. Am. Chem. Soc., 1998. **120**(49): p. 12974-12975.
  10. Zabuga, A.V. and T.R. Rizzo, *Capping Motif for Peptide Helix Formation.* J. Phys. Chem. Lett., 2015. **6**(9): p. 1504-1508.
  11. Stearns, J.A., O.V. Boyarkin and T.R. Rizzo, *Spectroscopic Signatures of Gas-Phase Helices: Ac-Phe-(Ala)<sub>5</sub>-Lys-H<sup>+</sup> and Ac-Phe-(Ala)<sub>10</sub>-Lys-H<sup>+</sup>.* J. Am. Chem. Soc., 2007. **129**(45): p. 13820-13821.
  12. Hendricks, N.G., N.M. Lareau, S.M. Stow, J.A. McLean and R.R. Julian, *Bond-Specific Dissociation Following Excitation Energy Transfer for Distance Constraint Determination in the Gas Phase.* J. Am. Chem. Soc., 2014. **136**(38): p. 13363-13370.

13. Nagornova, N.S., T.R. Rizzo and O.V. Boyarkin, *Cover Picture: Exploring the Mechanism of IR–UV Double-Resonance for Quantitative Spectroscopy of Protonated Polypeptides and Proteins (Angew. Chem. Int. Ed. 23/2013)*. *Angew. Chem. Int. Ed.*, 2013. **52**(23): p. 5887-5887.
14. Frisch, M.J., G.W. Trucks, H.B. Schlegel, G.E. Scuseria, M.A. Robb, J.R. Cheeseman, G. Scalmani, V. Barone, B. Mennucci, G.A. Petersson, H. Nakatsuji, M. Caricato, X. Li, H.P. Hratchian, A.F. Izmaylov, J. Bloino, G. Zheng, J.L. Sonnenberg, M. Hada, M. Ehara, K. Toyota, R. Fukuda, J. Hasegawa, M. Ishida, T. Nakajima, Y. Honda, O. Kitao, H. Nakai, T. Vreven, J.A. Montgomery, J.E. Peralta, F. Ogliaro, M. Bearpark, J.J. Heyd, E. Brothers, K.N. Kudin, V.N. Staroverov, R. Kobayashi, J. Normand, K. Raghavachari, A. Rendell, J.C. Burant, S.S. Iyengar, J. Tomasi, M. Cossi, N. Rega, J.M. Millam, M. Klene, J.E. Knox, J.B. Cross, V. Bakken, C. Adamo, J. Jaramillo, R. Gomperts, R.E. Stratmann, O. Yazyev, A.J. Austin, R. Cammi, C. Pomelli, J.W. Ochterski, R.L. Martin, K. Morokuma, V.G. Zakrzewski, G.A. Voth, P. Salvador, J.J. Dannenberg, S. Dapprich, A.D. Daniels, Farkas, J.B. Foresman, J.V. Ortiz, J. Cioslowski and D.J. Fox, *Gaussian 16*, 2016: Wallingford CT.
15. Clark, T., J. Chandrasekhar, G.W. Spitznagel and P.V.R. Schleyer, *Efficient Diffuse Function-Augmented Basis Sets for Anion*

- Calculations. III. The 3-21+G Basis Set for First-Row Elements, Li-F.* J. Comput. Chem., 1983. **4**: p. 294-301.
16. Becke, A.D., *Density-Functional Thermochemistry. III. The Role of Exact Exchange.* J. Chem. Phys., 1993. **98**(7): p. 5648-5652.
17. Lee, C., W. Yang and R.G. Parr, *Development of the Colle-Salvetti Correlation-Energy Formula into a Functional of the Electron Density.* Phys. Rev. B, 1988. **37**(2): p. 785-789.
18. Grimme, S., S. Ehrlich and L. Goerigk, *Effect of the damping function in dispersion corrected density functional theory.* J. Comput. Chem., 2011. **32**(7): p. 1456-1465.
19. Dian, B.C., A. Longarte and T.S. Zwier, *Hydride Stretch Infrared Spectra in the Excited Electronic States of Indole and its Derivatives: Direct Evidence for the  $1\pi\sigma^*$  State.* J. Chem. Phys., 2003. **118**(6): p. 2696-2706.
20. Kidwell, N.M., D.N. Mehta-Hurt, J.A. Korn, E.L. Sibert and T.S. Zwier, *Ground and Excited State Infrared Spectroscopy of Jet-Cooled Radicals: Exploring the Photophysics of Trihydronaphthyl and Inden-2-ylmethyl.* J. Chem. Phys., 2014. **140**(21): p. 214302.
21. Ahlrichs, R., M. Bär, M. Häser, H. Horn and C. Kölmel, *Electronic structure calculations on workstation computers: The program system turbomole.* Chem. Phys. Lett., 1989. **162**(3): p. 165-169.

22. Schirmer, J., *Beyond the Random-phase Approximation: A New Approximation Scheme for the Polarization Propagator*. Physical Review A, 1982. **26**(5): p. 2395-2416.
23. Trofimov, A.B. and J. Schirmer, *An efficient polarization propagator approach to valence electron excitation spectra*. Journal of Physics B: Atomic, Molecular and Optical Physics, 1995. **28**(12): p. 2299.
24. Hättig, C. and F. Weigend, *CC2 excitation energy calculations on large molecules using the resolution of the identity approximation*. J. Chem. Phys., 2000. **113**(13): p. 5154-5161.
25. Dunning, T.H., *Gaussian Basis Sets for Use in Correlated Molecular Calculations. I. The Atoms Boron Through Neon and Hydrogen*. J. Chem. Phys., 1989. **90**(2): p. 1007-1023.
26. Casida, M.E., *Time-Dependent Density-Functional Theory for Molecules and Molecular Solids*. Journal of Molecular Structure: THEOCHEM, 2009. **914**(1): p. 3-18.
27. Yanai, T., D.P. Tew and N.C. Handy, *A New Hybrid Exchange-Correlation Functional Using the Coulomb-Attenuating Method (CAM-B3LYP)*. Chem. Phys. Lett., 2004. **393**(1): p. 51-57.
28. Stanton, J.F. and R.J. Bartlett, *The Equation of Motion Coupled-Cluster Method. A Systematic Biorthogonal Approach to Molecular Excitation Energies, Transition Probabilities, and Excited State Properties*. J. Chem. Phys., 1993. **98**(9): p. 7029-7039.

29. Curutchet, C. and B. Mennucci, *Toward a Molecular Scale Interpretation of Excitation Energy Transfer in Solvated Bichromophoric Systems*. J. Am. Chem. Soc., 2005. **127**(47): p. 16733-16744.
30. Russo, V., C. Curutchet and B. Mennucci, *Towards a Molecular Scale Interpretation of Excitation Energy Transfer in Solvated Bichromophoric Systems. II. The Through-Bond Contribution*. J. Phys. Chem. B, 2007. **111**(4): p. 853-863.
31. Martin, R.L., *Natural transition orbitals*. J. Chem. Phys., 2003. **118**(11): p. 4775-4777.
32. Stearns, J.A., S. Mercier, C. Seaiby, M. Guidi, O.V. Boyarkin and T.R. Rizzo, *Conformation-Specific Spectroscopy and Photodissociation of Cold, Protonated Tyrosine and Phenylalanine*. J. Am. Chem. Soc., 2007. **129**(38): p. 11814-11820.
33. Kopysov, V. and O.V. Boyarkin, *Resonance Energy Transfer Relates the Gas-Phase Structure and Pharmacological Activity of Opioid Peptides*. Angew. Chem. Int. Ed., 2016. **55**(2): p. 689-692.
34. Stearns, J.A., C. Seaiby, O.V. Boyarkin and T.R. Rizzo, *Spectroscopy and Conformational Preferences of Gas-Phase Helices*. Phys. Chem. Chem. Phys., 2009. **11**(1): p. 125-132.
35. Voronina, L., A. Masson, M. Kamrath, F. Schubert, D. Clemmer, C. Baldauf and T. Rizzo, *Conformations of Prolyl–Peptide Bonds in the*



- Bradykinin 1–5 Fragment in Solution and in the Gas Phase.* J. Am. Chem. Soc., 2016. **138**(29): p. 9224-9233.
36. Ebata, T., N. Mizuochi, T. Watanabe and N. Mikami, *OH Stretching Vibrations of Phenol–(H<sub>2</sub>O)<sub>1</sub> and Phenol–(H<sub>2</sub>O)<sub>3</sub> in the S<sub>1</sub> State.* J. Phys. Chem., 1996. **100**(2): p. 546-550.
37. Platt, J.R., *Classification of Spectra of Cata-Condensed Hydrocarbons.* J. Chem. Phys., 1949. **17**(5): p. 484-495.
38. Scholes, G.D., *Long-Range Resonance Energy Transfer in Molecular Systems.* Annu. Rev. Phys. Chem., 2003. **54**(1): p. 57-87.
39. Lakowicz, L., *Principles of Fluorescence Spectroscopy.* Springer, New York, 2006: p. 954.
40. Curutchet, C. and B. Mennucci, *Quantum Chemical Studies of Light Harvesting.* Chem. Rev., 2017. **117**(2): p. 294-343.
41. Azarias, C., R. Russo, L. Cupellini, B. Mennucci and D. Jacquemin, *Modeling Excitation Energy Transfer in multi-BODIPY Architectures.* Phys. Chem. Chem. Phys., 2017. **19**(9): p. 6443-6453.
42. Furche, F. and R. Ahlrichs, *Adiabatic Time-Dependent Density Functional Methods for Excited State Properties.* J. Chem. Phys., 2002. **117**(16): p. 7433-7447.
43. Kenny, E.P. and I. Kassal, *Benchmarking Calculations of Excitonic Couplings between Bacteriochlorophylls.* J. Phys. Chem. B, 2016. **120**(1): p. 25-32.

44. Muñoz-Losa, A., C. Curutchet, B.P. Krueger, L.R. Hartsell and B. Mennucci, *Fretting about FRET: Failure of the Ideal Dipole Approximation*. Biophys. J., 2009. **96**(12): p. 4779-4788.
45. Prlj, A., M.E. Sandoval-Salinas, D. Casanova, D. Jacquemin and C. Corminboeuf, *Low-Lying  $\pi\pi^*$  States of Heteroaromatic Molecules: A Challenge for Excited State Methods*. J. Chem. Theory Comput., 2016. **12**(6): p. 2652-2660.
46. Wellman, S.M.J. and R.A. Jockusch, *Moving in on the Action: An Experimental Comparison of Fluorescence Excitation and Photodissociation Action Spectroscopy*. J. Phys. Chem. A, 2015. **119**(24): p. 6333-6338.

## Chapter 6. Conclusions

This thesis aimed to determine the structure of the following biomolecular objects: (1) amino acid clusters, (2) glycans, and (3) peptides. For this purpose, we used cryogenic vibrational spectroscopy that can provide critical insights into the connectivity in the molecule and how it changes with a different conformation. The thesis was organized into three case studies, in which the link between the hydrogen bonding network and the structure is established.

Firstly, we reported the structure of the  $\text{Ser}_8\text{H}^+$  cluster as determined by the combination of cryogenic ion spectroscopy of He-tagged  $\text{Ser}_8\text{H}^+$  and simulated annealing *ab initio* molecular dynamics. The found structure is  $\sim 25$  kcal mol<sup>-1</sup> more stable than the previously reported most stable structure [1]. All eight serines are zwitterionic and form a tight and nearly complete hydrogen bonding network, which is disrupted upon the removal of a single serine. Furthermore, this octameric assembly does not have docking points for the addition of another amino acid as only the two hydroxyl groups and a few N-H groups are exposed to the outside. Therefore, the formation of a  $\text{Ser}_9\text{H}^+$  cluster by adding one more serine to the octamer is disfavored. The presence of two free side-chain OH groups explains the facile substitution of up to two serines. We observe that if any serine other than  $\alpha$  and  $\beta$  is substituted, either by another amino acid or by D-serine, the entire hydrogen bonding network will be disrupted.

Secondly, we proposed a method for spectroscopic identification of the anomeric hydroxyl oscillators in carbohydrates.  $^{18}\text{O}$  isotopic labeling of the reducing end in protonated glucosamine leads to a  $12\text{ cm}^{-1}$  redshift of two lines in the spectrum. With IR-IR double-resonance spectroscopy we collected conformer-selective spectra of three conformers of protonated glucosamine. Quantum mechanical computations agree well with the highly resolved experimental spectra. Moreover, they are consistent with the assignment of the anomeric OH bands, which shift upon exchange with  $\text{H}_2^{18}\text{O}$ . Next, we explored the spectroscopy of a deprotonated glycan and of glycan fragments formed in collision-induced dissociation (CID).

Finally, we described the case study of a short model peptide containing phenylalanine and tyrosine chromophores. We have combined electronic and vibrational spectroscopy in a cryogenic ion trap to produce highly resolved, conformer-selective spectra for the ground and excited states of the model peptide. These spectra permitted us to determine the precise three-dimensional structure of the peptide and gave insight into the migration of the electronic excitation from phenylalanine to tyrosine. This was possible because infrared spectra of the excited states are sensitive to localization of the electronic energy in each chromophore. The electronic energy transfer efficiency was found to depend on the spatial orientation of the chromophores. The well-controlled experimental conditions make this result a stringent test for theoretical methods dealing with electronic energy transfer.

The developed conformer-selective He predissociation spectroscopy opens many promising avenues of research. Most importantly, this technique is well-suited for structural investigation of an important class of biomolecules – glycans. As we showed in this thesis, cryogenic infrared spectroscopy senses the slightest change in the structure of a glycan, and the proposed facile isotopic labeling allows us to identify the vibrational bands of the reducing end OH in the cryogenic IR spectrum. These two methods can provide a wealth of structural information especially in the case of glycan fragments. Such an issue as the influence of the charge location in the glycan on its fragmentation pattern can be studied to a high level of detail with the presented techniques. Mechanistic studies of glycan fragmentation are very important to develop a universal approach for glycan *de novo* sequencing. Such a sequencing approach would allow identifying unknown glycans, which is a top priority in modern glycoscience (as emphasized in the US National Research Council Committee report “Transforming Glycoscience: A roadmap for the future” [2]).

References:

1. Schalley, C.A. and P. Weis, *Unusually stable magic number clusters of serine with a surprising preference for homochirality*. Int. J. Mass spectrom., 2002. **221**(1): p. 9-19.
2. Council, N.R., *Transforming Glycoscience: A Roadmap for the Future*. 2012, Washington, DC: The National Academies Press. 208.

# Appendix: Cryogenic infrared spectroscopy of mobility-selected ions

Proline cis-trans isomerization in peptides acts as a conformational switch that leads to major changes in the peptide structure [1-3]. Proline is also found frequently in the regions of proteins with high conformational heterogeneity [4]. Clemmer *et al.* have recently investigated a nonapeptide NPY<sub>1-9</sub> with IMS-MS and resolved a few different conformational families [3]. NPY<sub>1-9</sub> is a fragment of human neuropeptide Y and is highly abundant in the central and peripheral nervous systems and regulates a variety of biological processes. The structure of NPY<sub>1-9</sub> is: Tyr-**Pro**-Ser-Lys-**Pro**-Asp-Asn-**Pro**-Gly-NH<sub>2</sub>. Studies suggested that the Pro<sub>2</sub> residue may be important for binding the Y<sub>1</sub> receptor [5].

For a deeper insight into the nonapeptide structure, we perform cryogenic infrared spectroscopy (CIS) of mobility selected ions in a tandem IMS/CIS spectrometer shown in Figure A.1. Electrosprayed ions pass through a drift tube filled with helium gas at 3 mbar, then we select ions by their CCS and inject them into a cryogenic flat trap and tag them with H<sub>2</sub>. The tagged ions are accelerated into a time-of-flight mass spectrometer and are irradiated on the flight with IR light. Monitoring the depletion of the tagged species in dependence of the IR frequency, we acquire an IR action spectrum.

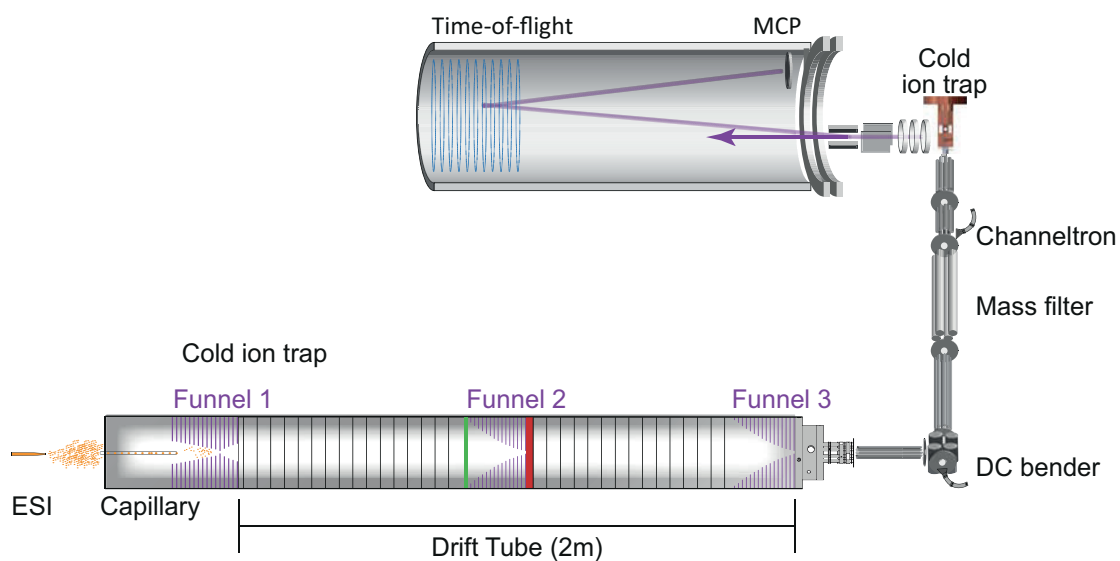


Figure A.1. Layout of the IMS/CIS tandem mass spectrometer. Courtesy of Michael Kamrath.

Due to a rich proline content, the NPY<sub>1-9</sub> fragment produces three peaks in the arrival-time distribution (Figure A.2), which has been attributed to different proline *cis-trans* isomers, consistent with the literature distribution [3].

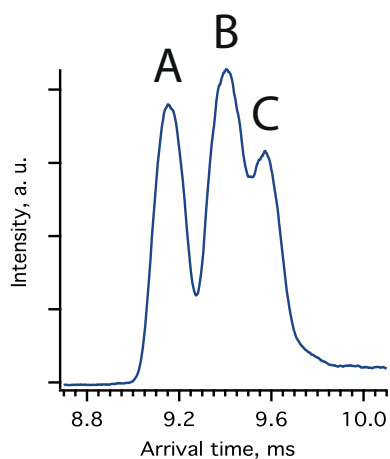
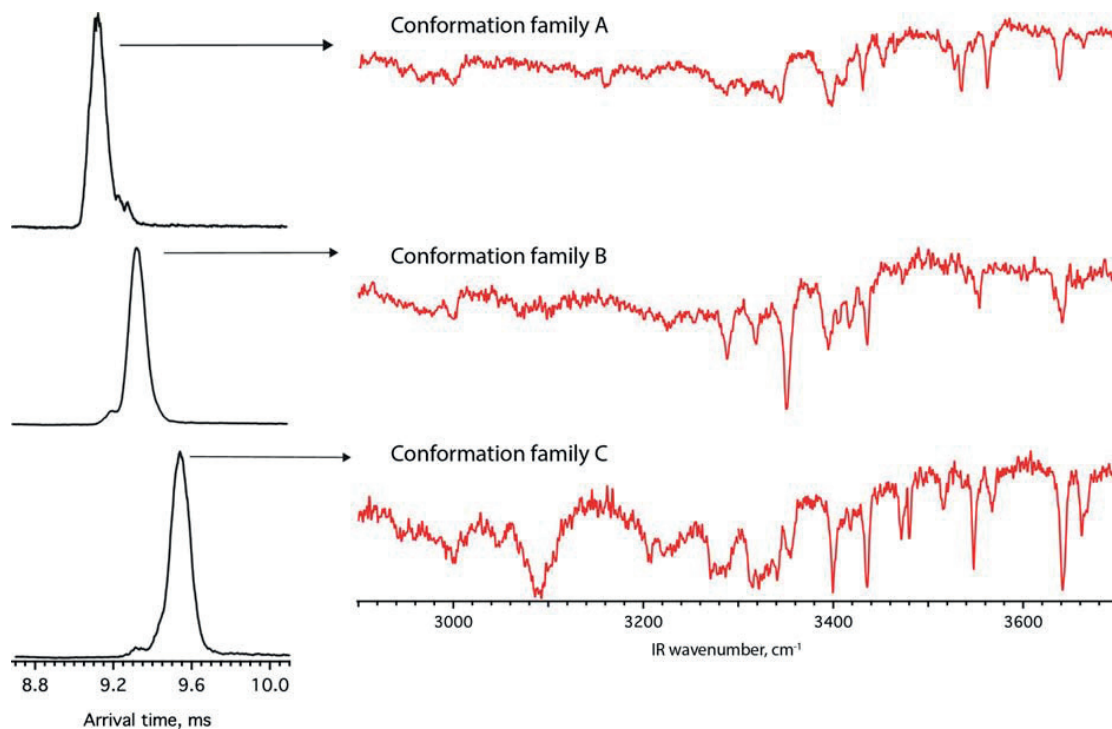


Figure A.2. Arrival-time distribution of NPY<sub>1-9</sub>.



We send each mobility separated conformation family into the cold trap and perform IR spectroscopy on it (Figure A.3).



*Figure A.3. IR spectra corresponding to each mobility separated species.*

The IR spectra appear to be different, which indicates that we are able to transfer the conformers to the cold trap without isomerizing them. Highly resolved IR spectra along with collision cross section information can provide stringent constraints for theoretical modeling of the conformation.

References:

1. Voronina, L., A. Masson, M. Kamrath, F. Schubert, D. Clemmer, C. Baldauf and T. Rizzo, *Conformations of Prolyl–Peptide Bonds in the Bradykinin 1–5 Fragment in Solution and in the Gas Phase*. J. Am. Chem. Soc., 2016. **138**(29): p. 9224-9233.
2. Shi, L., A.E. Holliday, N. Khanal, D.H. Russell and D.E. Clemmer, *Configurational-Coupled Protonation of Polyproline-7*. J. Am. Chem. Soc., 2015. **137**(27): p. 8680-8683.
3. Glover, M.S., E.P. Bellinger, P. Radivojac and D.E. Clemmer, *Penultimate Proline in Neuropeptides*. Anal. Chem., 2015. **87**(16): p. 8466-8472.
4. Andreotti, A.H., *Native State Proline Isomerization: An Intrinsic Molecular Switch*. Biochemistry, 2003. **42**(32): p. 9515-9524.
5. G., B.-S.A., W.H. A., W. Helmut, W. Klaus-Dieter, R. Klaus and J. Günther, *Complete L-Alanine Scan of Neuropeptide Y Reveals Ligands Binding to Y1 and Y2 Receptors with Distinguished Conformations*. Eur. J. Biochem., 1994. **225**(3): p. 947-958.

# Acknowledgements

During the four years I spent at EPFL, every day was full of excitement for me. I need to thank many brilliant people for this memorable experience in Switzerland.

I would like to thank Prof. Thomas Rizzo for all the resources, support and independence he gave me in pursuing my doctoral degree. Thanks to his valuable advice I learned to be self-critical and to cultivate high standards of research, because “when you prepare the manuscript you need to be more critical about your work than any reviewer”.

I am very thankful to Dr. Anne-Sophie Chauvin, Prof. Etienne Garand, Prof. Jos Oomens and Prof. Ulrich Lorenz, for evaluating this thesis and for their insightful questions at my PhD exam.

Dr. Aleksandra Zabuga and Dr. Mike Kamrath introduced me to the instruments that were present in the lab at the time when I joined LCPM. I am very grateful to them for sharing their knowledge. Particular thanks go to Dr. Chiara Masellis, who with her energetic and passionate character made the time we spent inside and outside the lab unforgettable. I appreciate Dr. Oleg Aseev’s friendship and great support when I arrived in Switzerland. It was great to have enthusiastic discussions about science and life in general with Dr. Liudmila Voronina. The atmosphere in our bio-group continues to be particularly warm and productive thanks to its current team: Ahmed Ben Faleh, Robert Pellegrinelli, Natalia Yalovenko, Irina

## Acknowledgements

---

Diukova, Priyanka Bansal, and Dr. Stephan Warnke. Thank you, Stephan, for helping me develop my ingenuity and problem-solving skills!

It has been a pleasure to have passionate and profound scientific discussions with Dr. Marcel Drabbels, Prof. Rainer Beck, Dr. Andreas Osterwalder, and Dr. Oleg Boyarkin. As it usually happened after our discussions, they were willing to help me out with their equipment.

I would like to thank all my LCPM colleagues for spending time during and after work, I enjoyed a lot practicing mountain sports with them. Thank you, Dr. Maarten van Reijzen, for teaching me to snowboard! My gratitude expands also to the LND group and, in particular, to Pavel Olshin. His courageous character and special sense of humor brought a lot of fun into our numerous conversations. Many thanks are addressed to our group secretary Angeles Alarcon. I appreciate a lot her help and kind smile.

I am especially grateful to Dr. Marta Perez and Dr. Antonio Prlj for accepting to collaborate with us and for their splendid theoretical work. Here I would like to mention also the great support from the ISIC mechanical workshop, especially Yves Morier and André Fattet.

From the bottom of my heart I thank my family for giving me courage to come to the finish line of my “PhD marathon”.

Last but not least, thank you, dear reader, for reading though this thesis.

# Curriculum Vitae

## Education

---

Since September 2014: PhD student at **EPFL**, LCPM, PhD advisor: Prof. Thomas Rizzo  
September 2009 – June 2014: **Lomonosov Moscow State University**, Chemistry Specialist Degree with Honours (chemistry department, Laboratory of High Energy Chemistry), **GPA: 5.00/5.00**  
September 1997 – June 2009: “**Mihai Eminescu**” High School in Bălți, Republic of Moldova.

## Teaching activities

---

1. Spring semester 2015 – experimental physical chemistry for Bachelor students.
2. Spring semester 2016 – experimental physical chemistry for Bachelor students.
3. Fall semester 2016 – chemistry laboratory work I for Bachelor students.
4. Spring semester 2017 – exercises session in the chemical thermodynamics course for Bachelor students.
5. Fall semester 2017 – exercises session in the spectroscopy course for Bachelor students.
6. Spring semester 2018 – exercises session in the quantum chemistry course for Bachelor students.

## Publications in peer-reviewed journals:

---

1. Sadig Aghazada, Iwan Zimmermann, **Valeriu Scutelnic**, and Mohammad Khaja Nazeeruddin: “Synthesis and Photophysical Characterization of Cyclometalated Ruthenium Complexes with N-Heterocyclic Carbene Ligands”. *Organometallics*, **2017**, 36 (13), p. 2397–2403. <https://pubs.acs.org/doi/10.1021/acs.organomet.7b00354>
2. Liudmila Voronina, **Valeriu Scutelnic**, Chiara Masellis, Thomas Rizzo: “Can mutational analysis be used to assist structure determination of peptides”. *JACS*, **2018**, 140 (7), p. 2401–2404. <https://pubs.acs.org/doi/10.1021/jacs.7b11302>
3. **Valeriu Scutelnic**, Marta Perez, Mateusz Marianski, Stephan Warnke, Aurelien Gregor, Ursula Rothlisberger, Michael T. Bowers, Carsten Baldauf, Gert von Helden, Thomas R. Rizzo, and Jongcheol Seo: “The structure of the protonated serine octamer”, *JACS*, **2018**. <https://pubs.acs.org/doi/10.1021/jacs.8b02118>  
*ACS Editors’ Choice for publishing as open access article; JACS cover; featured in C&EN (<https://cen.acs.org/analytical-chemistry/spectroscopy/Serine-octamer-reveals-structure/96/i19>), JACS Spotlights (<https://pubs.acs.org/doi/10.1021/jacs.8b05773>).*
4. **Valeriu Scutelnic**, Antonio Prlj, Aleksandra Zabuga, Clemence Corminboeuf, Thomas Rizzo: “Infrared spectroscopy as a probe of electronic energy transfer”, *J. Phys. Chem. Lett.*, **2018**, 9, p. 3217-3223. <https://pubs.acs.org/doi/10.1021/acs.jpcclett.8b01216>